HIGH-RESOLUTION STUDIES OF BETA-DELAYED PROTON EMISSION IN LIGHT NUCLEI

Table of Contents

LIST OF ILLUSTRATIONS

LIST OF TABLES

HIGH-RESOLUTION STUDIES OF BETA-DELAYED PROTON EMISSION IN LIGHT NUCLEI

Richard George Sextro

Lawrence Berkeley Laboratory and Department of Chemistry
University of California, Berkeley, California 94720

ABSTRACT

Identified protons have been observed following beta decay of the precursor nuclei ^{21}Mg, ^{25}Si, ^{37}Ca, ^{40}Sc, ^{41}Ti, and ^{23}Al. These measurements spanned a proton energy range from 600 keV to 8.5 MeV, and included all significant particle decays of these nuclei. A helium-jet transport system was developed and used with various ΔE-E counter telescopes to obtain high-resolution, low-background spectra. These data permitted accurate location of proton unbound levels in the beta-decay daughters, and absolute branching ratios and $\underline{ft}$ values for these allowed decays have been determined.

The half-lives of these nuclei have been measured, and all except that for ^{41}Ti are consistent with the previous values. For ^{41}Ti, the half-life is 80 ± 2 msec, which differs from the old value of 88 ± 1 msec. This latter value is thought to have been affected by the presence of ^{37}Ca activity produced in a competing reaction.

The $\underline{ft}$ values for ^{21}Mg and ^{25}Si are compared to the negatron decay rates in their respective mirrors. For mass 21, $(\underline{ft})^+/(\underline{ft})^- = 1.10 \pm 0.08$, while for mass 25 this ratio is 1.17 ± 0.04. A comparison of predicted and observed beta-decay rates for the superallowed

decay to the $T = 3/2$ state in ^{41}Sc indicates that this level has an isospin impurity of ~ 8%.

The observed beta-decay rates in ^{21}Mg and ^{37}Ca are also contrasted with theoretical predictions for decay rates to their respective daughters. The calculated values agree well for ^{21}Mg, while for ^{37}Ca the calculations appear to be limited by the basis space used.

Delayed protons from ^{23}Al, the first member of the $A = 4n+3$ series of $T_z = 3/2$ nuclei, have been observed, and the half-life of ^{23}Al has been measured to be 470 ± 30 msec. In addition, delayed protons from ^{40}Sc were studied in order to ascertain their contribution to the proton spectra obtained from ^{3}He bombardment of ^{40}Ca.

I. INTRODUCTION

There are currently 24 known beta-delayed charged-particle precursors with $A \leq 50$ (for a general review, see Ha 72, Ha 74), including the most-recently discovered, ^{45}Cr (Ha 73). Although some of these are characterized by only one significant particle decay peak or have very small beta-branching ratios to particle-unbound levels, several members of the $T_z = -3/2$, $A = 4n+1$ series of nuclei exhibit complex proton decay spectra arising from beta decay to many unbound levels. Accurate determination of the particle energies and intensities from these nuclei can yield information on beta-decay strengths and spectroscopic details of excited states in the beta daughter. If these relative transition rates can be related to absolute beta-decay rates to the daughter, measurement of the particle decay intensities will yield absolute ft values for beta decay to the unbound levels.

Spectroscopic details can then be compared with theoretical predictions. Recent shell-model calculations (La 73) have provided both excitation energies and log ft values for some nuclei in the sd shell. Experimental measurements of ft values for these transitions through observation of delayed protons permit a new and sensitive test of these model wavefunctions, which in general, have been reasonably successful in describing energy spectra, spectroscopic factors for single-nucleon transfer reactions, and electromagnetic observables (La 73).

Moreover, beta decay studies in these light nuclei can furnish additional information on the question of mirror symmetry for beta decay. In a comparison of mirror beta-decay transitions in light nuclei for both even and odd A, Wilkinson (Wi 70a) pointed out an apparent proportionality between the ratio of mirror decay rates, and the $\beta^{\pm}$ -decay energy, given by

$$(ft)^{+}/(ft)^{-} \propto W_0^{+} + W_0^{-} . \qquad (1-1)$$

The superscripts + and - refer to positron and negatron decay, respectively, and W_0 is the <u>total</u> decay energy. More recent work by Wilkinson and others (Wi 72) on mirror decay rates for $T_z = \pm 1$, even A isobars indicates that the earlier systematic evidence for a "fundamental" asymmetry in these systems has in fact largely disappeared in the light of new experimental evidence. The odd-mass systems, however, continue to show positive values for this ratio (though not necessarily of non-trivial origin).

The nuclides ^{21}Mg (Ha 65a, Ve 68), ^{25}Si (Ha 65a, Re 66), ^{37}Ca (Ha 64, Re 64, Po 66) and ^{41}Ti (Re 64, Po 66) are among those in the $T_z = -3/2$, $A = 4n+1$ series that have not previously been studied with high energy-resolution, low-background techniques. For the present experiments a helium-jet transport system (Ma 69) was developed in order to detect charged particles from a thin source in a relatively background-free environment. The background was further reduced by use of a detector telescope and standard particle identification techniques (Go 64). These experimental techniques are detailed in Section III.

Results are reported in Section IV for delayed proton decay from ^{21}Mg, ^{25}Si, ^{37}Ca, ^{40}Sc, ^{41}Ti, and the first member of the A = 4n+3 series of T = -3/2 nuclei, ^{23}Al, and include detection of all significant particle decay branches from these nuclei. Beta decay branching ratios ranging over two to three orders of magnitude have been determined.

II. THEORY AND CALCULATIONS

The intensity of a particle decay peak is controlled by two factors, the partial width for this decay exhibited by the parent state in the $T_z = -1/2$ emitter nucleus, and by the strength of the preceding beta-decay transition connecting this state and the precursor ground state. These decays are shown schematically in Fig. 2-1. The beta-decay transition strength is defined in terms of an ft value, where f is the (unitless) statistical rate function and t the partial half-life for the decay. This product is usually between $\sim 1\times10^4$ and $\sim 3\times10^6$ sec for allowed beta decay in light nuclei (Go 66). Typically, partial half-lives are inferred from measurement of the total half-life and the beta decay branching ratios.

A. Statistical rate function

The statistical rate function is dependent upon the decay energy and the nuclear charge, and for allowed beta decay is given by (Ko 65, Bl 69, Go 71a):

$$f \equiv f(\pm Z, W_0^{\mp}) = \int_{0.511}^{W_0} Wp(W_0^{\mp}-W)^2 F(\pm Z,W)dW \qquad (2\text{-}1)$$

where W and p are the electron energy and momentum, respectively. W_0 is the total decay energy in terms of the nuclear mass difference, and is related to the end-point beta-decay energy E_0, or the atomic mass difference, Q_β, and excitation energy, E_x, by

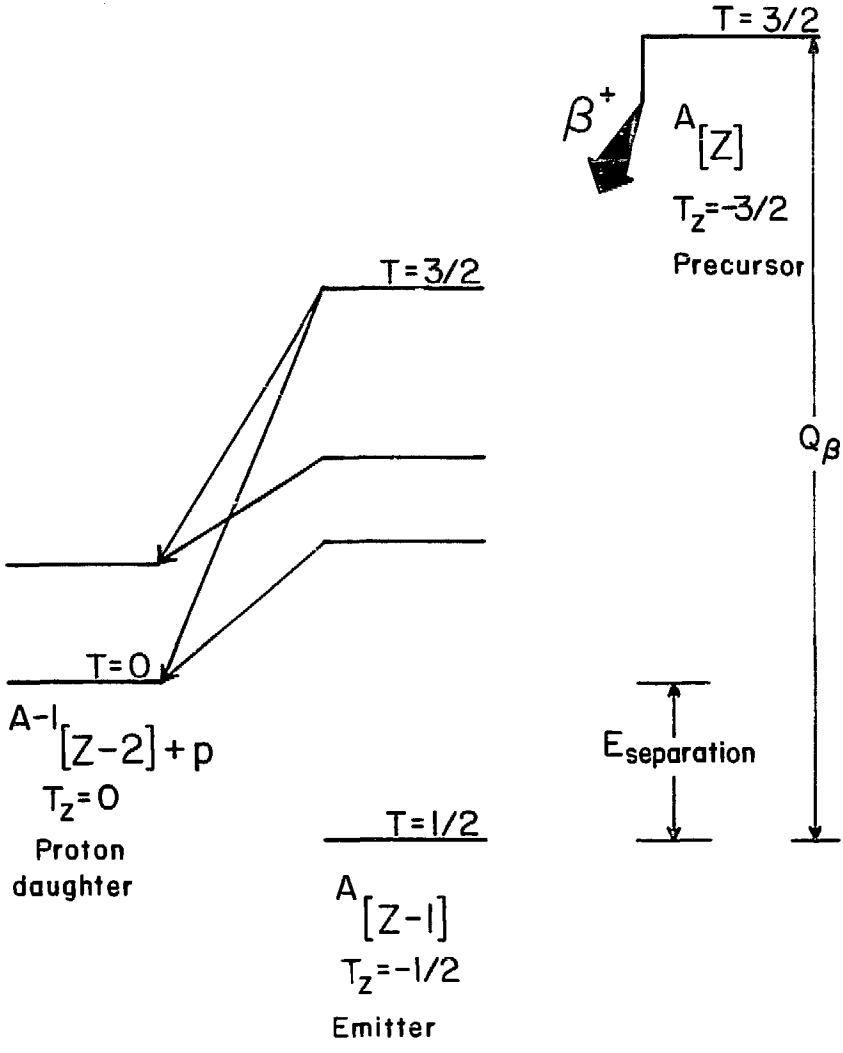

Fig. 2-1. An illustration of a typical beta-delayed proton decay scheme, showing the atomic mass difference, Q_β, and the proton separation energy.

$$W_0 = E_0 + 0.511 = Q_\beta - E_x \pm 0.511 \qquad \text{(all in MeV)}; \qquad (2\text{-}2)$$

$\pm Z$ is the charge of the daughter nucleus, and the positive and negative signs correspond to negatron and positron emission respectively. The solution for Eq. (2-1) depends on $F(\pm Z, W)$, the Fermi function, which cannot be evaluated in closed form. The accurate solution depends on knowing the lepton radial wavefunctions; usually it is written as:

$$F(\pm Z, W) = F_0(\pm Z, W)\, L_0 \qquad (2\text{-}3)$$

where
$$F_0 = \left(\frac{2pR}{\hbar}\right)^{2\gamma_0 - 2} e^{\pi\nu} \frac{|\Gamma(\gamma_0 + i\nu)|^2}{[(2\gamma_0 + 1)]^2} \qquad (2\text{-}4)$$

$$L_0 = \frac{[g_{-1}^2 + f_1^2]}{2p^2 F_0}\Bigg|_{r = R} \qquad (2\text{-}5)$$

and the nomenclature used is:

$\alpha \equiv e^2/\hbar c = 1/137.036$

$\nu = (\pm Z)\, \alpha W/c p$

$\gamma_0 = [1-(\alpha Z)^2]^{1/2}$

$R = r_0 A^{1/3}$

Γ is the usual gamma function, and g_{-1}^2, f_1^2 are the radial components of the lepton wavefunction evaluated at the nuclear radius R, for even and odd parity (assuming $j = 1/2$ for the lepton angular momentum).

Typically Eq. (2-5) is expanded to second order in αZ, so

$$L_0 = \frac{1 + \gamma_0}{2} \qquad (2\text{-}6)$$

which is the source of the usual approximation for finite size effects. The correction for screening by atomic electrons is made by substituting $W \mp V$ (for $e^{\mp}$) for W in Eq. 2-1, where (Ba 66a)

$$V \sim 1.45\, \alpha^2 \,|\, Z \,|^{4/3} \,. \qquad (2\text{-}7)$$

However, with the interest in comparing measured $0+ \rightarrow 0+$ pure Fermi transition strengths ($\Delta T = 0$) with theoretical predictions and the precise evaluation of beta-decay coupling constants, the above approximations do not give the required accuracy. To a lesser extent the intercomparison of mirror Gamow-Teller decay rates in light nuclei is likewise affected. Two major corrections are required: 1) the inclusion of higher order terms in the equation for L_0 and 2) corrections for electromagnetic radiative effects.

The former has been estimated by Wilkinson (Wi 70b), among others, and for light nuclei ($Z < 30$) and high beta decay energy, this can amount to ~3%. Hence, following his analysis, higher order terms have been included in the equation for L_0:

$$L_0 = 1 - \frac{1}{4}(\alpha Z)^2 - \frac{5}{3}\,\alpha Z\, W R - \frac{1}{3}\left(\frac{\alpha Z R}{W} + (pR)^2\right). \qquad (2\text{-}8)$$

This equation is used in the evaluation of $F(\pm Z, W)$ for calculating the statistical rate function, f, as done in the computer program FERMI (Ba 66a).

The radiative corrections are considered in two parts, the 'inner' correction which does not depend on Z or W_0 (i.e. it is nuclide independent), and the 'outer' corrections which are Z and W_0

dependent. The former do depend on details of the decay process, but can effectively be considered as a renormalization of the beta-decay coupling constants (Bl 70). The outer corrections, on the other hand, are evaluated for each case, and can be written as

$$\underline{f} = \underline{f}' (1 + \Sigma \delta_i) \qquad (2\text{-}9)$$

where $\underline{f}'$ is evaluated from Eq. (2-1) and δ_i is the correction for $i^{\underline{th}}$ order in α.

Wilkinson and Macefield (Wi 70) have estimated δ to order $Z\alpha$, and their parameterization for the $Z=0$ case has been used here for both negatron and positron decay. (This estimate compared to their tabulated values for $Z \leq 30$ is accurate to $< 0.2\%$ in its effect on $\underline{f}$). The second order correction (δ_2) is given by Jaus and Rasche (Ja 70) as

$$O[Z\alpha^2] \sim 4\times10^{-4} Z \qquad (2\text{-}10)$$

and, although small, has been included in the present $\underline{f}$ calculations. The estimate to third order (Ja 72) is $\delta_3 \sim 3.6\times10^{-6}Z^2$, and is clearly small enough ($\lesssim 3\times10^{-3}$ for $Z \leq 30$) to be neglected.

Statistical rate functions calculated using the approximation for L_0 shown in Eq. (2-6), and ignoring outer radiative corrections were compared with those including a more correct evaluation of finite size effects (Eq. 2-8) and the outer radiative corrections just discussed; differences of up to as much as $\sim 5\%$ were found. As a further check on the accuracy of the prescription of $\underline{f}$ calculations described above, $\underline{f}$ values were calculated for several $0+ \rightarrow 0+$ superallowed decays and

were compared to those calculated by Towner and Hardy (To 73). The largest deviation was 0.22% for the positron decay of ^{50}Mn.

The method for calculating the statistical rate function described in this section appears to be accurate enough to give essentially no systematic contribution to errors for either $\underline{f}$ values or for ratios of positron to negatron decay rates due to approximations made in the calculation. The present calculations include an estimate for the error in each $\underline{f}$ value caused by uncertainties in W_0.

B. Allowed beta decay and nuclear matrix elements

The comparative half-life ($\underline{ft}$) for allowed beta decay is related to the nuclear matrix elements, viz.:

$$\underline{ft} = \frac{1.231 \times 10^{-94} \text{ c.g.s. units}}{g_V'^2 \langle 1 \rangle^2 + g_A'^2 \langle \sigma \rangle^2} \qquad (2\text{-}11)$$

where g_V' is the renormalized vector coupling constant, $\langle 1 \rangle$ the Fermi matrix element, g_A' the renormalized axial-vector coupling constant, and $\langle \sigma \rangle$ the Gamow-Teller matrix element. As noted above the renormalization is due to the inclusion of inner radiative corrections (Bl 70). From the evaluation of several well-known $0+ \rightarrow 0+$ pure Fermi transitions in the light nuclei, Towner and Hardy (To 73) have deduced the value for g_V' as

$$g_V' = 1.413 \times 10^{-49} \text{ erg} \times \text{cm}^3 . \qquad (2\text{-}12)$$

Decay of the neutron yields a measurement of g_A'/g_V'; Wilkinson (Wi 73) has recently re-evaluated this ratio to be

$$g_A'/g_V' = 1.251 \,. \tag{2-13}$$

So equation (2-11) becomes

$$\underline{ft} = \frac{6166}{\langle 1 \rangle^2 + 1.565 \langle \sigma \rangle^2} \text{ sec} \,. \tag{2-14}$$

Wavefunctions for the precursor and for states in the daughter can be written (assuming isospin purity for the parent state) as

$$\psi_i = | \psi (J_i, T_i, T_z(i)) \rangle \tag{2-15}$$

and, allowing for isospin mixing in the daughter,

$$\psi_f = a | \psi(J_f, T_f, T_z(f)) \rangle + b | \psi(J_f, T_f', T_z(f)) \rangle \tag{2-16}$$

properly normalized so $a^2 + b^2 = 1$.

The Fermi matrix element is

$$\langle 1 \rangle = \langle \psi_f | \sum_n \tau_\pm(n) | \psi_i \rangle \tag{2-17}$$

where

$$\sum_n \tau_\pm(n) = T_\pm \tag{2-18}$$

and $\tau_\pm(n)$ is the isospin raising (+) or lowering operator (-) and can operate on all $\underline{n}$ nucleons. τ_+ converts a proton to a neutron, and τ_- a neutron to a proton. Accordingly, $T_\pm$ operating on ψ_i gives

$$T_\pm | \psi(J, T, T_z) \rangle = [(T \mp T_z)(T \pm T_z + 1)]^{1/2} | \psi(J, T, T_z \pm 1) \rangle \,. \tag{2-19}$$

Hence it connects initial and final states differing <u>only</u> in isospin projection T_z, <u>i.e.</u> $|T_z(f) - T_z(i)| = 1$, so that from Eqs. (2-16) and

(2-17)

$$\langle 1 \rangle^2 = [\, T(T+1) - T_z(i)\, T_z(f)]\, a^2. \qquad (2\text{-}20)$$

Clearly, for the $T = 3/2$ superallowed positron decays considered here, $\langle 1 \rangle^2 = 3a^2$, and the evaluation of this matrix element does not depend on choice of model wavefunctions, only on the degree of isospin purity of ψ_f.

The Gamow-Teller matrix element, on the other hand, does not reduce so simply. Its form is given by

$$\langle \sigma \rangle = \langle \psi_f \,|\, \sum_n \sigma(n) \cdot \tau_\pm(n) \,|\, \psi_i \rangle \qquad (2\text{-}21)$$

where $\sigma(n)$ is the Pauli spin operator and $\tau_\pm(n)$ is as defined above. The selection rules can be deduced from the properties of $\sum_n \sigma(n) \cdot \tau_\pm(n)$, which is a rank 1 tensor, and hence can give $\Delta J = 0, \pm 1$ and $\Delta T = 0, \pm 1$.

The actual evaluation of $\langle \sigma \rangle$ depends upon the nuclear wavefunctions. For the case of superallowed beta decay to the analogue $T = 3/2$ state, $\langle \sigma \rangle$ has been estimated from the Nilsson formalism for beta decay in the $A = 4n+1$, $17 \leq A \leq 37$ mass region (Ha 65). More recently, Lanford and Wildenthal (La 73) have predicted $\langle \sigma \rangle$ for beta decay for some nuclei in the sd shell, including mass 21 and mass 37. The earlier estimates agree with shell-model calculations for these two masses. For these superallowed decays $1.565\, \langle \sigma \rangle^2 / \langle 1 \rangle^2 \leq 15\%$ for the $A = 4n+1$ ($A \leq 37$) nuclides; hence the transition rate for these decays can be calculated from equation (2-14) in a nearly model-independent way.

C. Isospin mixing

Because the nuclear Hamiltonian is not charge independent, isospin mixing of $T_<$ states into $T_>$ states and vice-versa can occur. Primarily this charge-dependence is due to the Coulomb potential, although other charge dependent forces, such as the short range nuclear force, can contribute. In general the longer range Coulomb force dominates (Bl 69). The charge-dependent potential can be a sum of isovector and isotensor parts; generally, as is done here, the isovector part is assumed to dominate. (Recently, Adelberger, et al. (Ad 73) have indicated evidence for mixing due to the isotensor potential in the particle decays of T = 3/2 levels in masses 13 and 17.)

If the mixing is assumed small, perturbation theory can be used to show that

$$(E_{T_>} - E_{T_<})\, a = \langle \psi(T_>) \,|\, H_c \,|\, \psi(T_<) \rangle \qquad (2\text{-}22)$$

where E_T is the excitation energy of the state with isospin T, and H_c is the charge-dependent part of the nuclear Hamiltonian. From this equation, the amount of mixing of the $T_>$ state with nearby $T_<$ states can be estimated from knowledge of the size of the matrix elements, which have been tabulated by Bloom (Bl 66), Blin-Stoyle (Bl 69), and Bertsch and Mekjian (Be 72).

It is important to note that particle decays of the T = 3/2 levels in the daughter can occur only through isospin admixing in these levels, since proton decay to states in the $T_z = 0$ daughter nucleus are isospin forbidden. Calculations by Arima and Yoshida (Ar 71) for mass 13 have shown that $a^2 \leq 1\%$ admixture in the T = 3/2 state is necessary to

reproduce the partial widths. Other calculations by Auerbach and Lev (Au 71) give $a^2 - 1\%$ for mass 41.

These results from (Au 71) show that the predominant mixing in the T = 3/2 state occurs with the antianalogue state (configuration state). Although this point will be discussed in greater detail in Sec. IV, the antianalogue configuration is simply that of the analogue state (T = 3/2) recoupled to T = 1/2. These wavefunctions can each be expanded in terms of the single-particle wavefunctions. Since these constituent configurations are identical (just coupled to different T) the resulting beta decay matrix elements are related simply by the ratio of the Clebsch-Gordon coefficients, C(T), involved in the expansion, viz:

$$\langle \psi(T_<, T_z') \,|\, \Sigma \sigma \cdot \tau \,|\, \psi(T_>, T_z) \rangle = \frac{C(T_>)}{C(T_<)} \langle \psi(T_>, T_z') \,|\, \Sigma \sigma \cdot \tau \,|\, \psi(T_>, T_z) \rangle . \tag{2-23}$$

The relationship between the Gamow-Teller matrix element for beta decay to the T = 3/2 state, $\langle \sigma \rangle_{S.A.}$ to that for decay to the antianalogue state (T = 1/2), $\langle \sigma \rangle_{A.A.}$, is:

$$\langle \sigma \rangle_{S.A.} = \frac{C(T_<)}{C(T_>)} \langle \sigma \rangle_{A.A.} = \frac{1}{\sqrt{2}} \langle \sigma \rangle_{A.A.} . \tag{2-24}$$

The usefulness of this relationship will become evident in the discussion of results for mass 41 in Sec. IV D.

D. Partial widths and penetrabilities

The decay modes exhibited by an unbound level depend mainly on the degree of overlap between the initial wavefunction and that describing a particular final state or exit channel, and external kinematic effects of penetration through Coulomb and angular momentum barriers. These factors can be written quantitatively (following Ma 68 and Mc 68) as a relationship between the partial width $\Gamma_{a\ell}$ for a given exit channel a, and the penetrability P and the reduced width γ^2:

$$\Gamma_{a\ell} = 2P_{a\ell}\gamma^2_{a\ell} \quad \text{(in MeV)} \tag{2-25}$$

where ℓ is the relative angular momentum involved in the decay (usually chosen to be the lowest possible value consistent with $\Delta\pi = (-1)^{\ell}$). All of the internal nuclear structure effects are contained in γ^2. The penetrability is given by

$$P_{a\ell} = \frac{\rho}{A^2_{a\ell}} \tag{2-26}$$

where

$$\rho = kR = kr_0(A_1^{1/3} + A_2^{1/3}) \tag{2-27}$$

k is the wave number, and is calculated from

$$k = \left(\frac{2\mu E}{\hbar^2}\right)^{1/2} \text{fm}^{-1} = 0.2187\ (\mu E)^{1/2}. \tag{2-28}$$

The energy E is in MeV in the center-of-mass (c.m.) system and μ is the reduced mass in amu.

The denominator in Eq. (2-26) is the penetration function, and is given by

$$A_{\alpha\ell}^2 = F_{\alpha\ell}^2 + G_{\alpha\ell}^2 , \qquad (2\text{-}29)$$

which are the regular and irregular solutions to the Coulomb function, respectively, for angular momentum ℓ. These solutions, and the resulting penetrabilities are obtained through the program COCAG.

Penetrabilities for two different nuclei are plotted in Figs. 2-2 and 2-3 to illustrate the effects of energy and angular momentum. Figure 2-2 shows the penetrabilities for excited states in ^{41}Sc decaying to the ground state and first three excited states in ^{40}Ca. It is evident from this figure that, for states below 6 MeV in excitation in ^{41}Sc, the ratio of penetrabilities for decay to the excited states in ^{40}Ca to that for decay to the ground state is extremely small. It is therefore likely that for excited states up to 6 MeV, proton decays to the ^{40}Ca g.s. will predominate.

On the other hand the proton decay penetrabilities for excited states in ^{25}Al, shown in Fig. 2-3, present a different picture. The Coulomb barrier in mass 25 is smaller than in mass 41, while the first few excited states in ^{24}Mg are lower in energy than their counterparts in ^{40}Ca. In addition the angular momentum barrier is lower in the mass 25 case for decays to the first-excited state in the proton daughter since the first-excited state in ^{24}Mg is $J^{\pi} = 2+$, while its counterpart in ^{40}Ca has $J^{\pi} = 0+$. In fact, for states in ^{25}Al above 5 MeV in excitation, decay to the ^{24}Mg ground state is less favored than

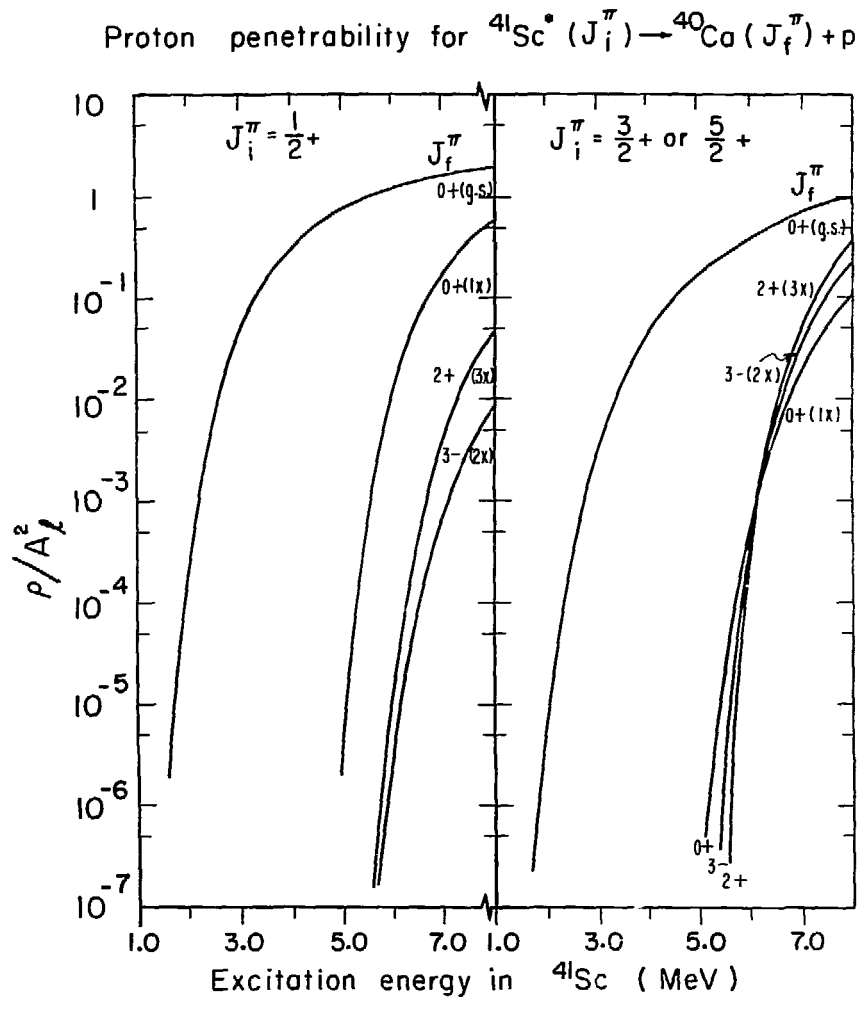

XBL738-4006

Fig. 2-2. Penetrability calculations for proton decay of $^{41}Sc(*)$. The ordinate is the penetrability $P = \rho/A_\ell^2$ calculated with $r_0 = 1.3$ fm (see text for details). The curves are labelled with the spin, parity and level order (ground state, 1st excited, 2nd excited, etc.) for each final state.

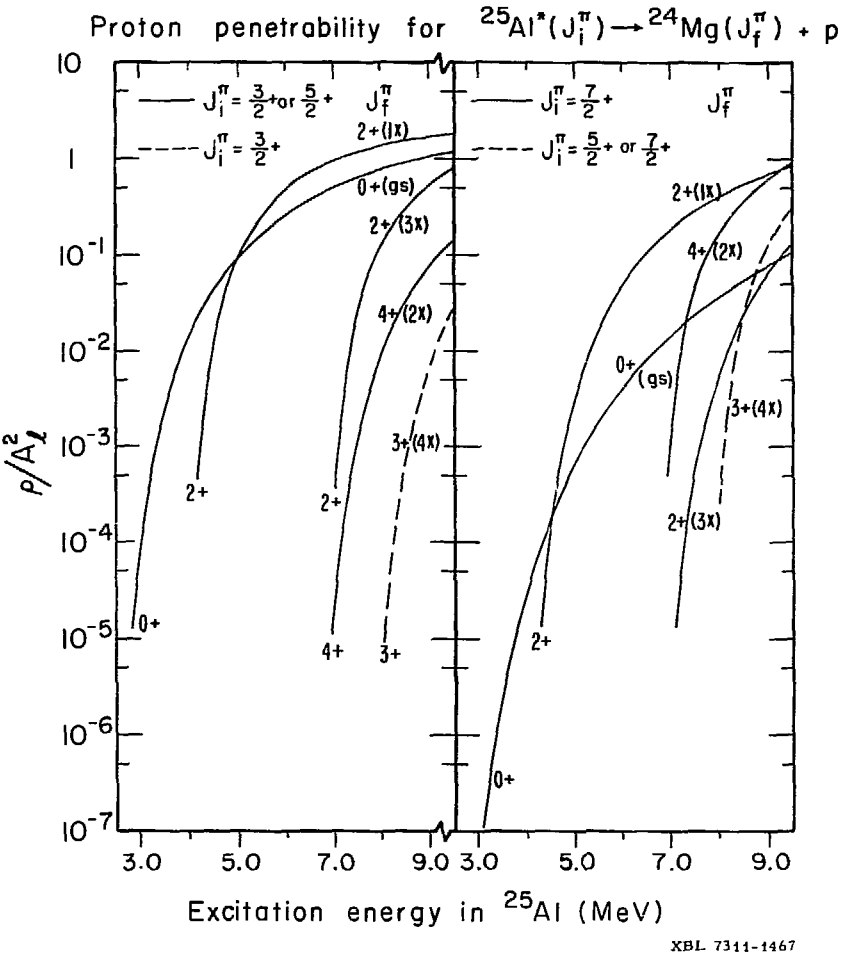

Fig. 2-3. Calculated penetrabilities for proton decay of $^{25}Al(*)$, with $r_0 = 1.3$ fm. See caption for Fig. 2-2 for other details.

proton decay to the 2+, first-excited state, as shown in Fig. 2-3. Therefore proton decays to excited states become kinematically more likely from levels at lower excitation energies in ^{25}Al than in the corresponding case in ^{41}Sc, and the resulting proton spectrum could be more complicated due to these competing decay modes.

No attempt has been made to calculate the reduced widths from model wave functions. In order to estimate partial decay widths and lifetimes, the Wigner sum-rule limit has been used (Ma 68), where

$$\gamma_\ell^2 \leq \frac{3}{2} \frac{\hbar^2}{\mu R^2} = \frac{62.7}{\mu R^2} \text{ MeV}. \qquad (2\text{-}30)$$

Then upper limits for partial widths, and lower limits on the partial half-lives follow:

$$\Gamma_{a\ell} \sim \frac{125.4 P_{a\ell}}{\mu R^2} \text{ MeV} \qquad (2\text{-}31)$$

and

$$t = \tau \ln 2 = \frac{\hbar \ln 2 \, \mu R^2}{125.4 P_{a\ell}} \text{ sec}. \qquad (2\text{-}32)$$

As discussed in Sec. IV, these limits are useful in estimating decay strengths of energetically-allowed, but unobserved decays.

III. EXPERIMENTAL TECHNIQUE

Accurate measurement of particle decay branches over a broad energy range, and hence determination of the preceding beta-decay strengths, depends on high-resolution, low-background spectra extending to low particle energies. Previous transport techniques developed to study the delayed-proton decay of gaseous activities employed a helium-sweeping system to carry activity away from the target area to a shielded counting chamber (Es 71). Although such a system was a clear improvement over the former method of directly observing decay particles from recoils stopped in the target, it did not appear to have a transport efficiency suitable for non-gaseous activities produced in low cross-section reactions. A helium-jet system (Ma 69), similar to those used in studies of α-emitting isotopes (among others), was designed and built for transport of light mass, non-gaseous activities.

A. Cyclotron, beam transport and pumping system

The cyclotron, beam transport system, and experimental area are shown in Fig. 3-1. The location of the pumping system with respect to the counting chamber is also shown; the total pumping distance was ~9 m through 10 cm inside-diameter (ID) pipe. This entire system was constructed to be compatible with other experiments using Cave 2, with all components of the experimental equipment readily removable for an unobstructed beam path to the facilities further downstream.

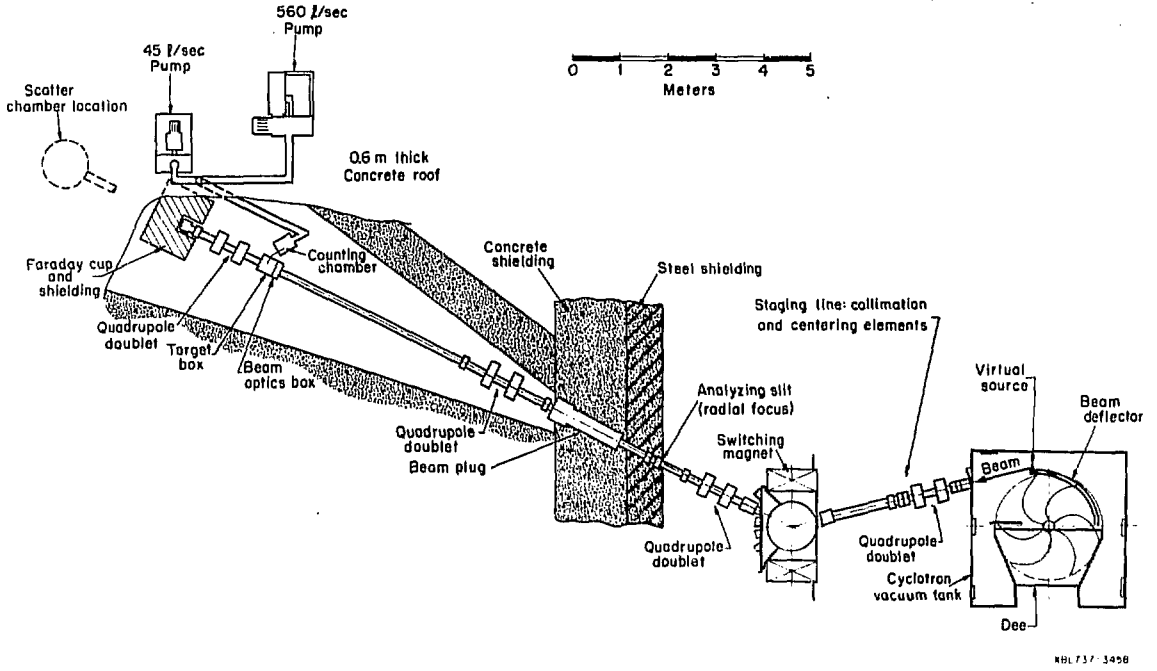

Fig. 3-1. System layout for Cave 2, showing the helium jet target box, counting chamber, and pumps. The scatter chamber was required for experiments using the shielded-detector (wheel) system.

A more detailed diagram of the helium-jet system is exhibited in Fig. 3-2. The cyclotron beam was focused on a retractable Al_2O_3 screen (monitored via closed-circuit television) located 10.8 cm upstream from the target box entrance foil. The beam spot size generally was 0.5 to 0.7 cm square in order to pass through the 1.0-cm diameter tantalum entrance collimator, which was located 4 cm upstream from the entrance foil. Foil lifetime was greatly reduced when the beam was focused to a smaller spot.

The beam entered the target box through the 1.0-cm diam entrance foil, exited through a similar 1.9-cm diam foil window and was refocused into a Faraday cup located ~1.8 m downstream. Either 5.6-μm Havar foils[1] (4.6 mg/cm^2) or 5-μm Ni foils[2] (4.5 mg/cm^2) were used for these isolation foil windows (no significant difference in foil durability was observed).

Typical $^3He^{+2}$ or p beam currents were 2 to 4 μA (at all bombarding energies), with usually < 50 nA dropped on the entrance collimator. Foil lifetimes ranged from 8 to 50 hours at these currents. A few exploratory experiments were conducted with ^{12}C and ^{16}O beams (the results of which are briefly discussed in Appendix A); the entrance foil was typically 2.5-μm Ni. Even then, isolation foil lifetime decreased appreciably unless the heavy ion beam intensities were limited to ~0.8 to 1.0 μA (measured fully stripped).

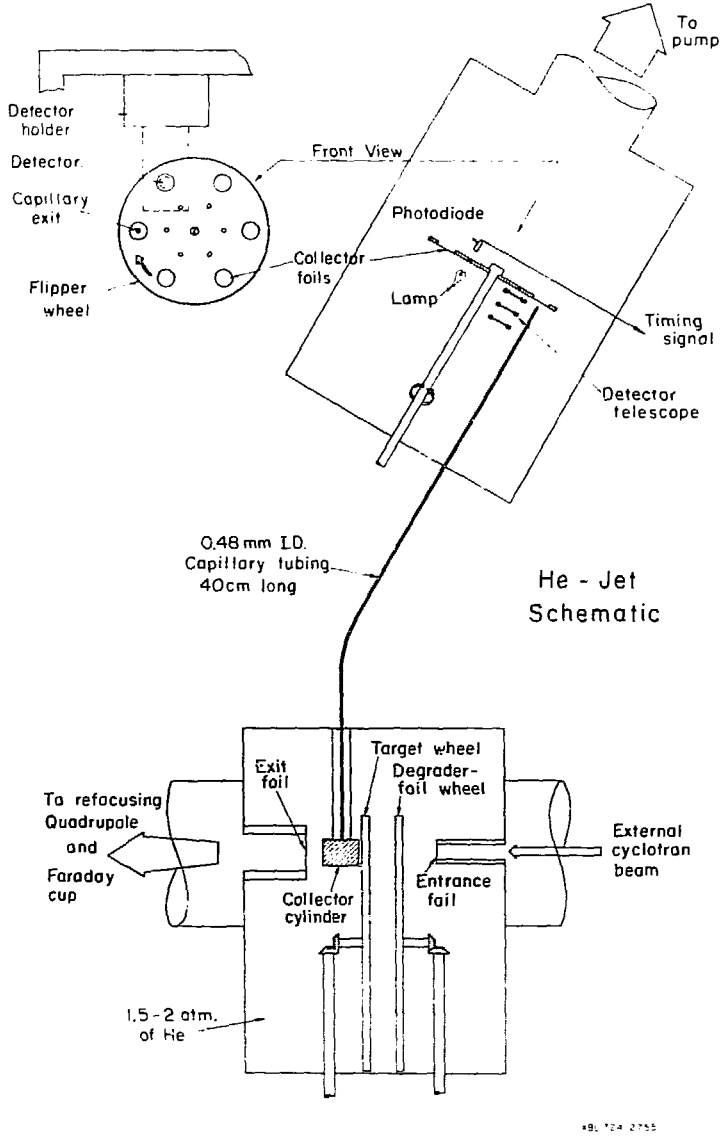

Fig. 3-2. A simplified drawing of the helium-jet transport system, showing in greater detail the target box and counting chamber. Specifics regarding its use are given in the text.

B. Helium-jet transport system

1. General operation

A photograph of the system is shown in Fig. 3-3, showing the target box, the target wheel assembly, and the counting chamber. Targets and beam degrader foils were mounted on parallel, 6-position wheels which could be manually positioned via geared shafts as shown in Figs. 3-2 and 3-3. The target wheel position was 5.2 cm from the entrance foil; the degrader foils were 2.2 cm upstream from the target. The target box was pressurized through the gas handling system shown in the upper-right corner of Fig. 3-3. Commercial-grade helium gas was used for solid targets, at a typical pressure of 1100-1500 torr (absolute). For the ^{21}Mg experiments, commercial spark chamber gas, consisting of 90% Ne and 10% He, was used as both target and transport gas.

A fraction of the beam-induced product nuclei recoiling from the target were thermalized by the gas within the 2.5-cm-long, 1.9-cm ID collector cylinder, entrained in the gas flow and swept into the 0.48-mm ID stainless steel capillary tube[3]. The recoils and gas were transported ~40 cm through the capillary tube into the counting chamber, and directed against a collector foil positioned 3 mm from the end of the capillary. Although no attempt was made to gain a detailed understanding of the complicated chemistry involved in the helium-jet technique, several empirical tests were made to study yield as a function of several parameters. The description and results of these tests are given in Appendix A.

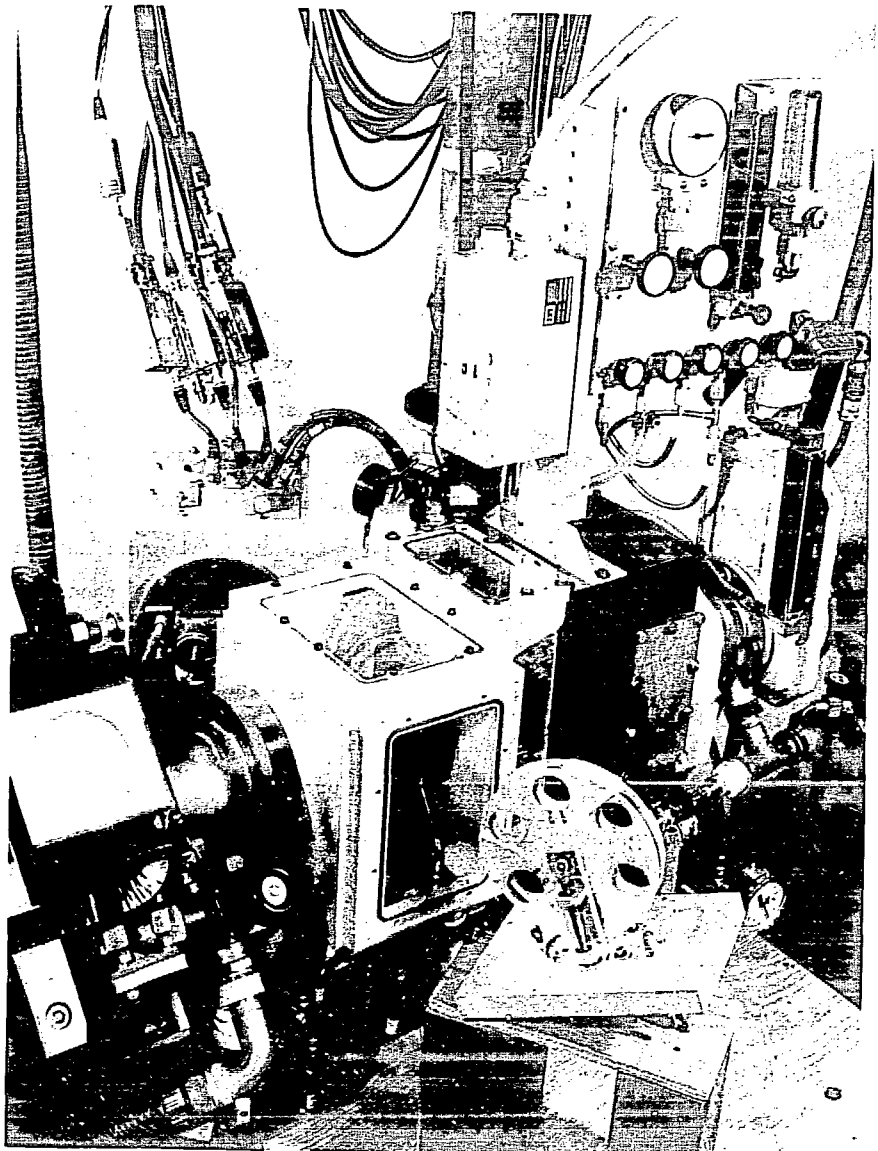

XBB 737-4585

Fig. 3-3. Picture of helium-jet apparatus, showing target box (light-colored box in center-foreground), with target/degrader-foil wheels removed and placed in front for exhibit. The beam enters from the right. The gas manifold is shown in the upper right corner, while the collection/counting chamber is shown in the background, with the detector turret and pre-amplifiers in place.

One major change in the operation of the system during the course of this work has been the introduction of chemical "additives." The results of tests conducted with this system and elsewhere have shown that for many reaction products of interest, the total system efficiency is greater as a result of these chemicals introduced into the helium gas. More information, including results of these tests, is also given in Appendix A.

The collection/counting chamber was continuously evacuated by a combination Roots-blower/mechanical pump. For the earlier experiments, the pumping speed was ~ 45 *l*/sec for He gas, which gave an operating pressure in the counting chamber of 0.3 to 0.4 torr. With the installation of a larger pump, the pumping speed increased to ~ 560 *l*/sec for He gas, and resulted in a counting chamber pressure of ~ 0.1 torr. The flow of He gas through the system was monitored continuously by a stainless-steel-ball-type flowmeter. Typically, the flow ranged from 16 to 25 torr-*l*/sec, depending on the target box pressure and gas used.

The collector wheel, shown in Figs. 3-2 and 3-4 was a 10-cm-diameter Al disk, with six collection foils mounted 60 degrees apart. Collection of activity and counting were done on the same side of the foil surface. The collection efficiency ("sticking" probability) was not measured directly, rather this is included in the overall system efficiency discussed in Appendix A. It is known, however, that there is some dependence on chemical species, since the rare gas nuclides do not adhere to the collector (Ma 70a). The present data corroborate

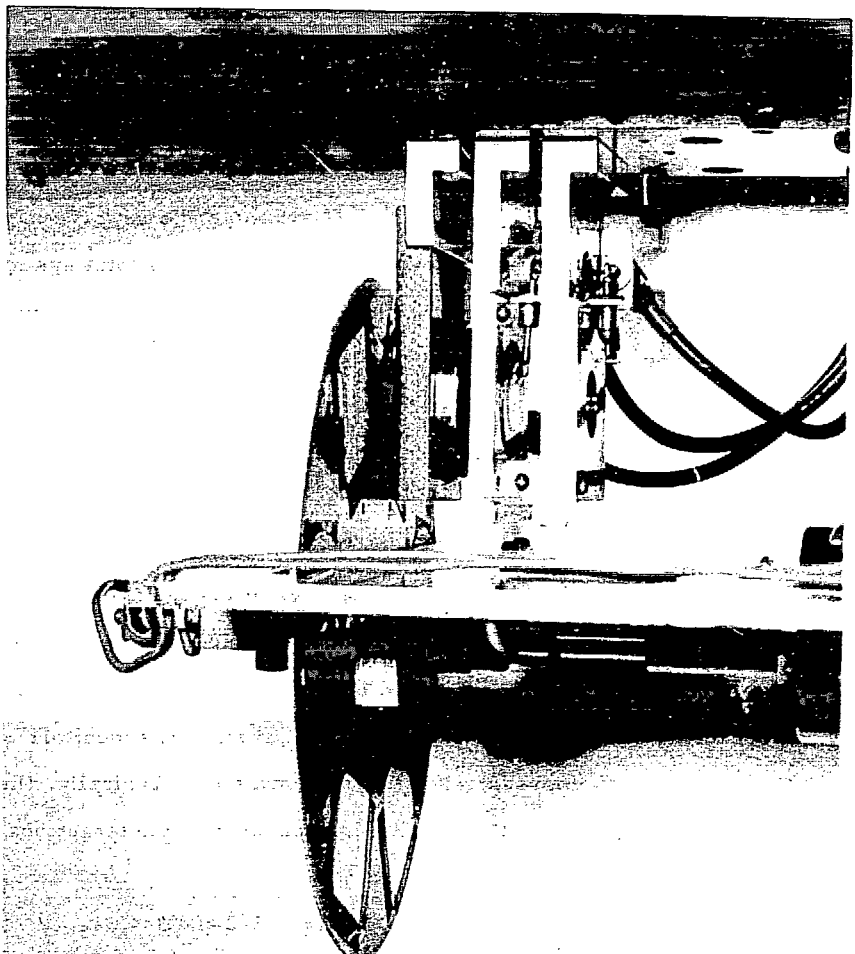

XBB 737-4588

Fig. 3-4. Close-up photograph of collector wheel, showing the relative position of the detector telescope. The wheel is 10 cm in diameter. The capillary tube enters from the right, and is obscured by the flipper wheel shaft.

this, since no evidence for proton peaks from the known (Ha 71) beta-delayed proton emitters ^{33}Ar or ^{17}Ne was found in those experiments in which their production was possible. (See Sec. IV for further discussion.)

Collector foils were typically 50-μm-thick Al disks; for experiments using a second telescope or anti-coincidence detector mounted on the opposite side of the foils, 0.6-μm thick Ni foils (~ 550 $\mu g/cm^2$) were used. The collector foils were moved from the collection position to the counting location by means of a 30 deg solenoidal stepping motor[4], and a 1:2 gear ratio. This position change required ~ 25 msec. Although the stepping motor could be fired as many as 10 times per second, typical cycle times were from 300-500 msec. No pulsing of the beam was necessary with this arrangement; while one foil was positioned in front of the capillary tube, the adjacent foil was being counted. The geometry of the system precluded the observation of events from foils on either side of the counting position.

2. Gas target

For the ^{36}Ar (^{3}He, 2n) ^{37}Ca experiments, a gas target and gas-handling system were constructed for use with the helium-jet. A sketch of the gas target system is shown in Fig. 3-5. For this reaction the recoil energy is quite small (~2.9 MeV using a 40 MeV ^{3}He beam); this places a severe limitation on the gas target exit window thickness. Furthermore, such a thin window cannot withstand a differential pressure of much more than 15 torr. It was necessary, under these limitations, to construct a gas target system with a minimum 'exposed'

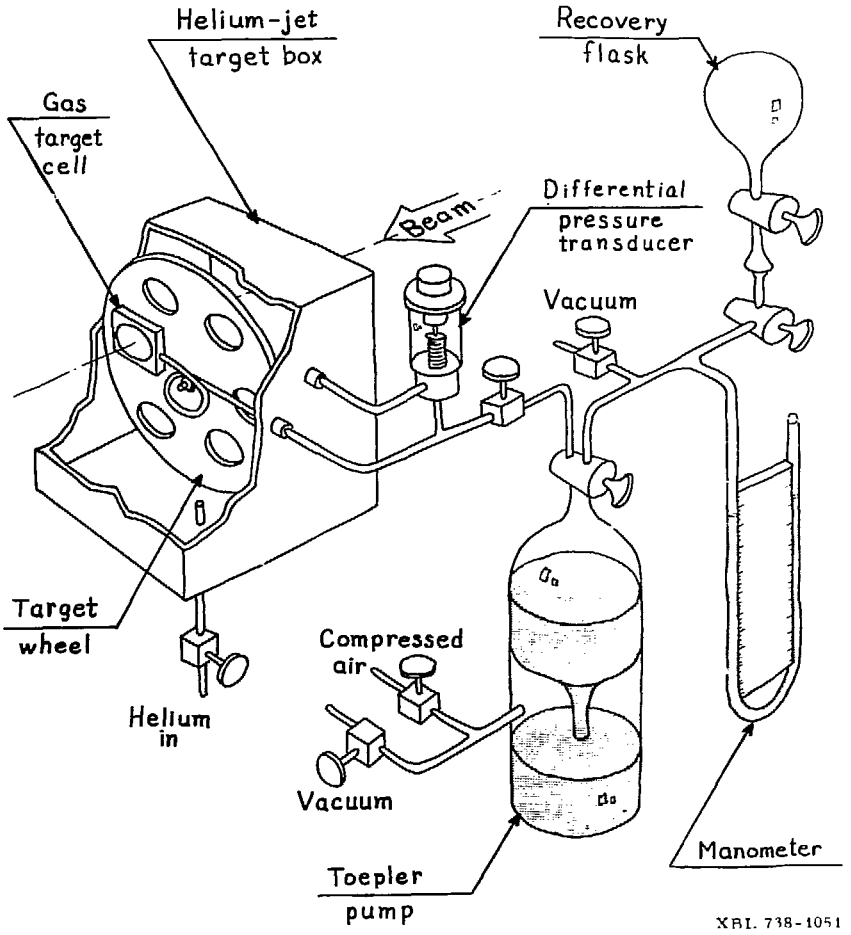

Fig. 3-5. Sketch of the gas target set-up for use with the helium-jet transport. For simplicity, only the target and gas handling apparatus are shown, with the transport system and counting chamber omitted. Details of its use are given in the text.

volume, and with the capability of simultaneously pressurizing both the target box and the gas target cell while maintaining a differential pressure of less than 10 to 15 torr.

The gas target entrance and exit foils were 1.91-μm and 0.23-μm thick Ni foils respectively (~ 200 $\mu g/cm^2$ for the exit foil). The inside dimensions of the stainless steel gas cell were 0.1 cm in length and 1.9 cm in diameter, with a total volume of ~2.9 cm^3. At a pressure of 1200 torr, this is equivalent to a target 2.83 mg/cm^2 thick; however, the severe recoil energy restrictions limit the useful target thickness to ~ 20% of this value which, depending on beam energy, is an effective target thickness of ~ 500 $\mu g/cm^2$. The gas pressures were equalized through use of a mercury-filled Toepler pump driven by compressed air. The argon target gas, enriched to 99% ^{36}Ar, was transferred from the top half of the Toepler pump which had been charged from the source/recovery flask. Simultaneously the target box was slowly filled with helium to its operating pressure. The differential pressure during the filling operation and during the course of the experiment was monitored with a specially designed differential pressure transducer, with a proportional dc output feeding a remote digital voltmeter. The transducer is shown in Fig. 3-6; it consists of a low-volume bellows[5] sealed at one end and a linear displacement transducer[6] which measures the bellows displacement due to pressure changes. The target box pressure served as a reference pressure; this system could measure differential pressures of the order of 0.05 torr. The helium input pressure was well-regulated to avoid pressure instabilities or drift.

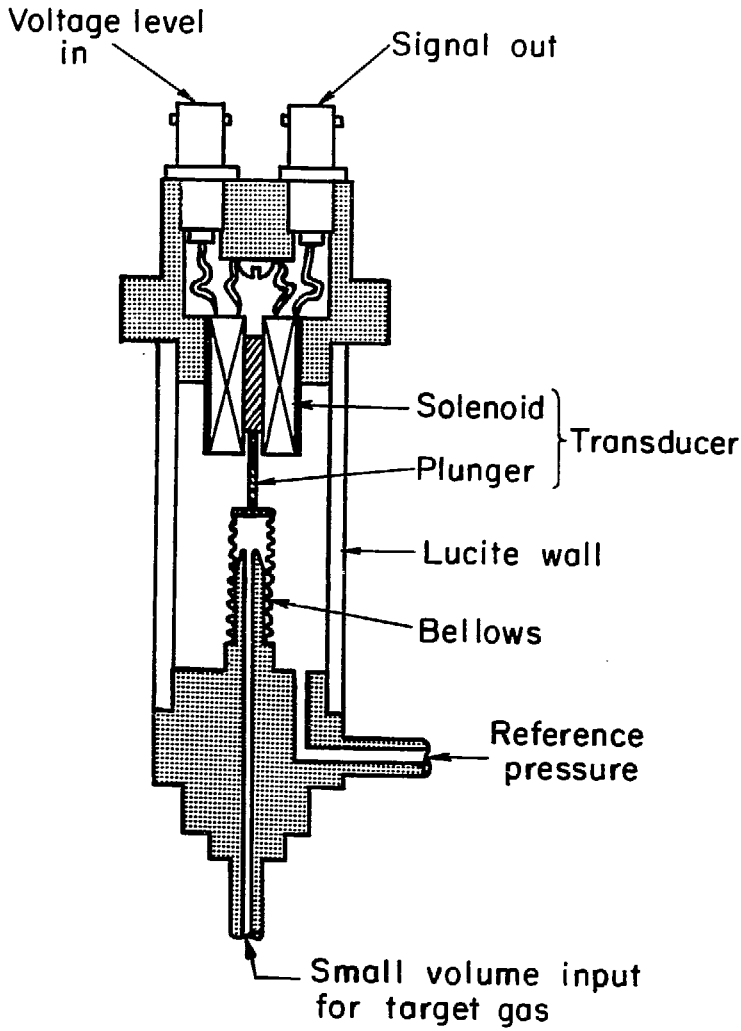

XBL 738-3664

Fig. 3-6. Cut-away drawing of the differential pressure transducer, showing the low-volume, highly-sensitive bellows and linear displacement transducer.

The cell was filled through a 1.5 mm ID flexible polyethylene capillary which allowed the target wheel to be rotated, permitting bombardment of other targets while not disturbing the gas target pressure. The total volume "exposed" to the helium-jet, including the volume of the ~1 mm ID connecting lines to the pressure transducer and the gas cell, is ~10 cm^3, thereby minimizing the amount of target gas lost in the event of a foil rupture.

C. Detectors and electronics

1. Particle detection and identification

Data obtained in the course of these experiments were acquired with silicon semiconductor telescopes. The thin dE/dx detectors (ΔE) ranged in thickness from 4 μm to 50 μm; the thinner detectors (notably 4, 6, 8, and 11 μm) were commercially prepared surface barrier detectors,[7] while the others were fully-depleted P-diffused Si prepared at LBL. The stopping detectors (E) were either ~50-μm, 164-μm, or ~ 260-μm thick P-diffused Si or 500-μm thick Si (Li). The telescopes assembled from these detectors spanned a large particle energy range--from ~ 600 keV to ~ 8.5 MeV for protons--and a lower limit on α-particle energies of ~ 1.4 MeV.

Each ΔE-E telescope was followed by a 100-μm thick partially-depleted Si detector 1.5 cm in diameter to reject long range particles traversing the telescope. The detectors were mounted as shown in Fig. 3-7. This detector turret was designed for nuclear reaction experiments with the 20-in. scattering chamber as well as for compatibility with these particle-decay experiments. The copper base plate

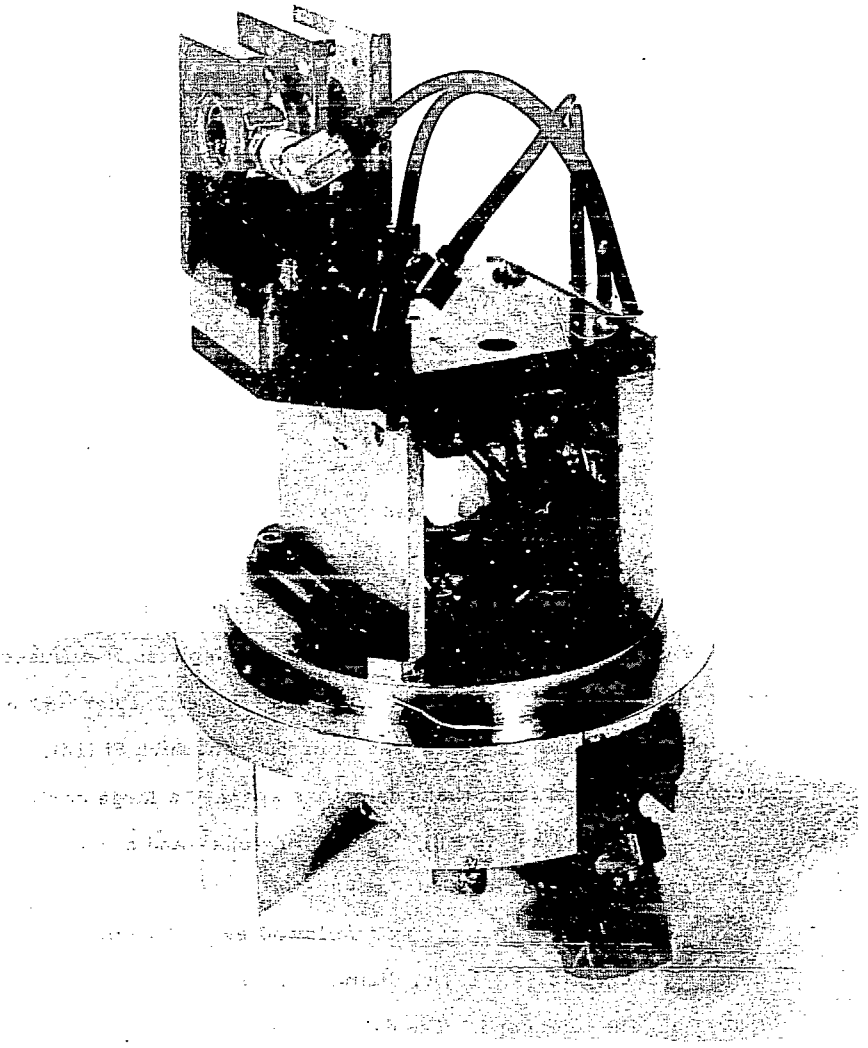

XBB 737-4584

Fig. 3-7. Photograph of detector turret and a counter telescope. The copper base is cooled with a thermoelectric cooler mounted underneath; the water cooling lines and external connections are shown.

and detectors (except the very thin detectors, which were insulated by fiberglass mounts) were cooled to ~ -25°C by a thermo-electric cooler[8] and heat sink assembly attached to the underside. Bias voltage and particle detection signals were carried through coaxial cables connected to each detector by Subminax or Microdot connectors.

In position, the detector turret accurately located the ΔE detector ~ 6 to 7 mm from the activity, depending on the exact detector configuration (see Fig. 3-4). The geometry of the telescopes was limited in every case by the diameter of the E counter; typically the solid angle was 0.24 sr.

Since the capacitance of a detector is proportional to the ratio of area to thickness, the thin detectors presented the problem of high capacitive noise, and low output signal voltage (see Go 65). Special pre-amplifiers were used which utilized two matched, field-effect transistors on the input stage, giving the pre-amp output a high signal-to-noise ratio. This output signal was amplified by another factor of 5 in a low-noise amplifier before being sent to the standard "198" linear amplifiers. A block diagram of the electronics set-up is shown in Fig. 3-8. Instead of the usual delay-line shaping at the linear amplifier stage, RC shaping was used for the 4, 6, and 8-μm thick detectors, with the integration time ~ 0.5 to 2.0 μsec.

After having met a coincidence requirement of $2\tau \sim 40$ nsec, the ΔE and E signals were fed into a Goulding-Landis particle identifier (P.I.) whose output is proportional to particle type (Go 64). Events corresponding to protons could be selected by setting SCA gates around the proton peak in the identifier spectrum. For some exper-

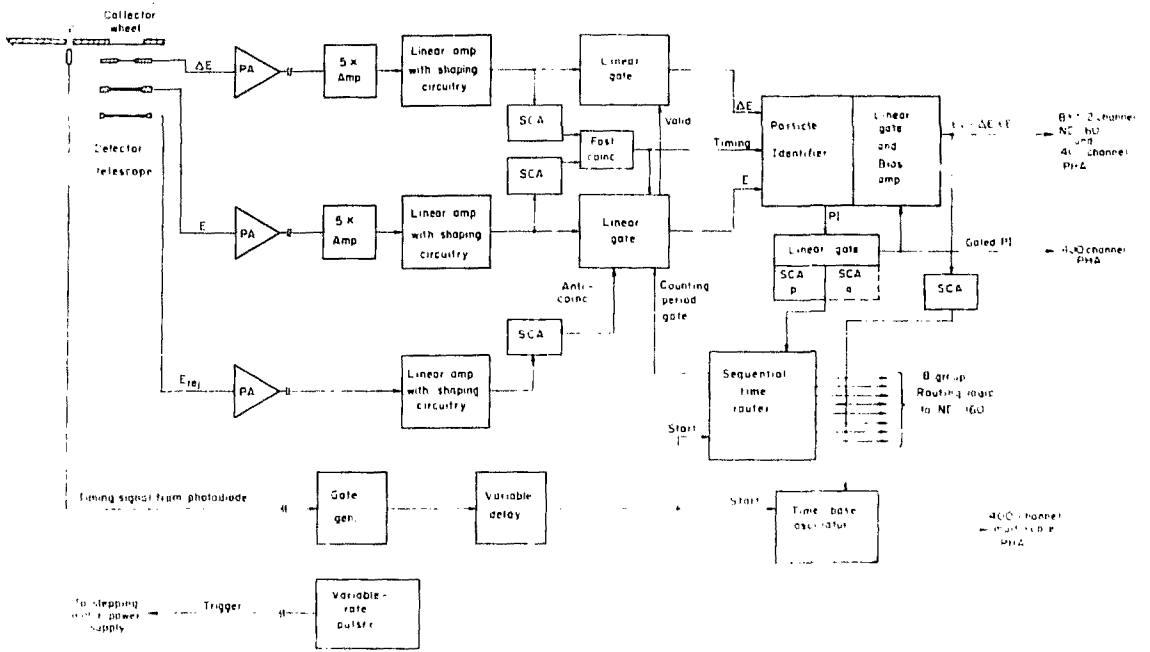

Fig. 3-6. Electronics diagram for use with the helium-jet system. Both counting electronics and timing and gating logic are shown.

iments, both protons and alphas were recorded. These P.I. gates helped to further eliminate events due to multiply-scattered beta particles. The total particle energy, E_T, signal was obtained from the sum of the ΔE and E signals.

The total particle resolution was dependent upon the exact combination of detectors used, but ranged from 25 to 45 keV FWHM for protons. This resolution was influenced, in part, by the large capacitance of the ΔE detectors. The observed proton widths were also influenced by the momentum-broadening due to the preceding β^+ decay, and in some cases, by the intrinsic widths of broad states themselves. The maximum beta-broadening contribution for each precursor is given in Table 3-1.

2. Timing and half-life measurements

The collector wheel provided a timing signal used to initiate each counting cycle. The associated electronics are shown schematically as part of Fig. 3-8. Six holes, each 1.6 mm in diameter, were located along the same radial axes as the collector foils, a small, collimated light beam passed through the hole onto a photodiode. This beam was interrupted when the wheel was stepped by the solenoidal motor, causing the photodiode to "gate-off" the voltage signal. The "on" signal was re-established by the light beam and photodiode when the wheel completed its 60 deg motion; this signal provided the start signal for the timing. Since the wheel mechanically or capacitively induced a noise signal in the detectors, the timing signal was delayed 30-50 msec to allow this detector noise to die away. Counting then began for a preset time, divided into four or eight sequential time

Table 3-1. Maximum Effect of Beta-Broadening on Observed Proton Peak Widths

Nuclide	Energy at Maximum (MeV) $E_{\beta+}$	E_p(lab)	FWHM (keV) [a]
^{21}Mg	~6.0	~3.5	14
^{25}Si	~6.0	~2.9	11
^{37}Ca	5.8	~2.9	7
^{41}Ti	7.0	~3.7	9
^{40}Sc	4.88	1.085	4 [b]
^{23}Al	3.80	0.818	4 [c]

a) This estimate assumes that the proton and positron momenta are parallel or anti-parallel, and that the resulting contribution to the line width can be calculated as a triangular distribution (see Ref. Es 71a).

b) This is calculated for the most intense proton peak.

c) This calculation is for the single observed proton decay peak.

groups of equal length (typically 30-50 msec each). Energy signals from the amplifiers were blocked while the collector wheel was stepped. During the counting period, E_T signals were stored both in a 400 channel analyzer and in a Nuclear Data ND-160 4096-channel analyzer, the latter being routed by the timing signals into 8 groups of 512 channels each. Data thus stored could be transferred off-line via a PDP-5 computer onto magnetic tape.

Logic signals corresponding to one peak or group of peaks of interest in the E_T spectrum were recorded in a 400-channel analyzer operating in the multiscale mode. The channel address was advanced at a preset rate by a quartz-crystal oscillator, and the system was initialized each time by the flipper wheel timing signal. This provided another semi-independent source of half-life information; in no case did data acquired with these two methods result in half-lives whose difference was greater than the sum of the statistical errors.

3. Anticoincidence experiments

In searching for possible protons from ^{23}Al whose energies were too low to penetrate the thin ΔE detector, it was necessary to look at ΔE-counter spectra in anticoincidence with the E detector following it, and in anticoincidence with a large area detector mounted on the opposite side of the collection foil. For these experiments, the collection foils were 550 $\mu g/cm^2$ Ni foils. The 1.8 cm diameter, 60-μm thick, partially-depleted detector was mounted 4.8 mm from the collector foil, giving a solid angle of 3.3 sr. The electronic set-up was nearly identical to that shown in Fig. 3-8, except that both this

detector, and the E detector were used in anticoincidence to the ΔE. The ΔE signals were then fed directly into the Nuclear Data operating in a 8×512-channel, time-routed mode. The experiment is discussed in Sec. IV E.

D. Pulsed beam experiments

Part of the ^{23}Al data was acquired using a pulsed-beam, shielded-detector system mounted in the scattering chamber (see Fig. 3-1). Although it has been described previously (Ce 72, Es 71a), it is shown here in Fig. 3-9 for the sake of completeness. A brief description follows.

A motor-driven 3.2-mm-thick Ta wheel rotated at a constant velocity in front of the detector telescopes, shielding them during beam-on periods. During the beam-off time, large slots rotated in front of the detectors, allowing the viewing of the target, and the proton decays of those recoil nuclei stopped in the target. The thick targets required for efficient recoil stopping affected the proton energy resolution achieved with this system. Some background, due to target activation, was also present in the proton spectra.

Control of the beam pulsing (via modulation of the cyclotron dee voltage) was achieved through use of light-source/photo-diode logic signals keyed to narrow slits in the wheel (see Fig. 3-9). For the ^{23}Al experiments the total cycle time, as determined by the preset wheel rotation period, was ~3.6 sec: ~1.4 sec bombardment, ~ 1.4 sec counting. The two detector telescopes were used as described for the helium-jet system electronics (Sec. III C). Half-life data were also

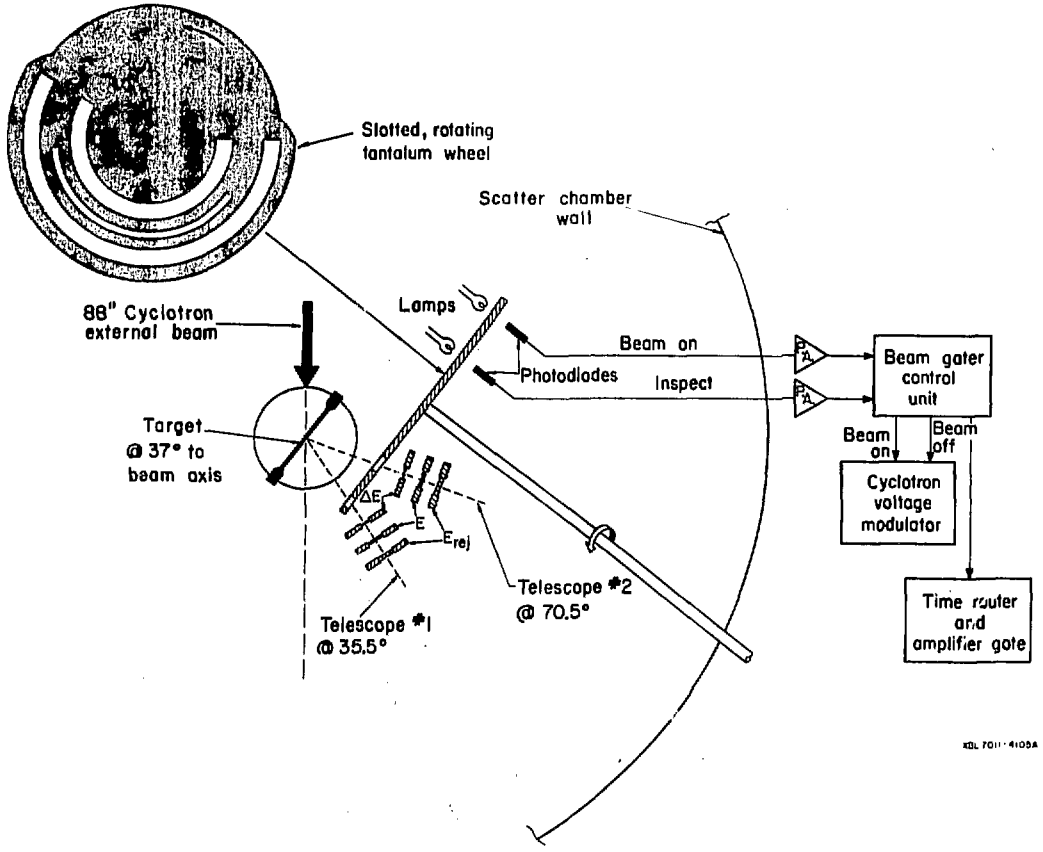

Fig. 3-9. Diagram of pulsed-beam, shielded-detector apparatus used for some of the ^{23}Al measurements.

acquired in a method similar to that already described.

This system also allowed the scattering of low energy protons--accelerated as low energy H_2^+ beams--into the detector telescopes as an energy calibration. The cross-sections or helium-jet efficiency calculated in Appendix A are based, in part, on low-quality ^{25}Si and ^{41}Ti data taken with the wheel system (Es 71a).

E. Data reduction and analysis

The E_T data, either summed or in separate time groups were analyzed peak-by-peak using an interactive, Gaussian peak-fitting program, DERTAG, (Ma 71a) on the SCC-660 computer. Centroids, peak widths, and integrals were obtained for each peak. In general, the 400 channel data from the PHA and the 512-channel data from the ND-160 were analyzed separately, and the resulting peak energies and intensities were then averaged together for the final results. Data from several different experiments on the same nuclide were usually combined by means of weighted averages for both peak energies and intensities.

Eight point half-life data for each statistically-significant peak were obtained from the peak-by-peak analysis described above. The 400-channel multiscale data were usually summed into a smaller number of time groups of equal length (e.g., usually 9 or 10 groups). Half-lives for individual peaks or groups of peaks were then deduced from both these sets of data using a least squares fit to an exponential curve via program CLSQ (Cu 63). This program had the capability of including a long-lived background; however, since the particle-identification reduced the background to negligible levels in most cases, there was no necessity for using this option.

Although these two sources of half-life information were not completely independent, they provided an excellent consistency check. The values thus obtained were averaged together (not treated as independent sources of data), while final half-lives were the result of a weighted average of these average values from several different experiments.

The energy for each proton decay peak was interpolated (or in rare cases extrapolated) from a calibration line fit to several calibrant peaks (discussed in Sec. IV A). Typically a straight-line least-squares fit was used; in only two cases was it necessary, because of slight nonlinearities at the extreme low-energy end of the decay spectrum, to use a quadratic fit to the calibration data.

IV. EXPERIMENTAL RESULTS AND DISCUSSION

The nuclides discussed in this section were all produced using ^{3}He or proton beams of various energies from the Berkeley 88-in. cyclotron. Since the $T_z = -3/2$, $A = 4n+1$ series of nuclides, and some of those in the neighboring $T_z = -1$, $A = 4n$ series, exhibit beta-delayed particle decay, the resulting particle spectra can potentially be complicated by competing reaction channels. These reactions, their products and thresholds are tabulated in Table 4-1, including both those nuclides of interest, and those produced in competing reactions. Half-lives shown include the present measurements; the mass-excesses used throughout this dissertation are from the 1971 Atomic Mass Table (Wa 71) unless otherwise noted.

A synopsis of the relevant Q_β values (differences in ground-state atomic masses) and proton or alpha separation energies are shown in Table 4-2. These numbers are used throughout this section in computing beta-decay transition strengths and excitation energies in the emitter nuclei.

A. Energy calibration

In addition to the requirements of high-resolution particle measurements, accurate calibration energy standards are necessary for precise level energy determinations in the beta daughter. Such precision is a necessary aid in assignment of decay protons to specific energy levels, and in identifying new levels in the emitter nucleus. Rather than base the calibrations on α-source standards such as ^{212}Bi-

Table 4-1. Reactions, Thresholds, and Half-Lives for Beta-Delayed Proton Precursors Produced from ^{20}Ne, ^{24}Mg, ^{36}Ar, and ^{40}Ca Targets

Product Nuclide [a]	(Reaction), Threshold (Lab) in MeV — Target ^{20}Ne	Target ^{24}Mg	Target ^{36}Ar	Target ^{40}Ca	Half-Life [b] (msec)
^{17}Ne	(^3He, 2nα), 31.2	(^3He, 2n 2α), 41.0	--	--	108.5 ± 0.9
^{20}Na [c, d]	(^3He, 2np), 25.8	(^3He, 2nαp), 35.7	--	--	446 ± 3
^{21}Mg	(^3He, 2n), 22.0	(^3He, 2nα), 32.0	--	--	122.5 ± 2.1 [e]
^{24}Al [f]	--	(^3He, 2np), 25.9	--	--	2066 ± 7
$^{24}Al^n$ [c]	--	(^3He, 2np), 26.4	--	--	130 ± 4
^{25}Si	--	(^3He, 2n), 21.3	--	--	220.7 ± 2.9 [e]
^{29}S	--	--	(^3He, 2n2α), 35.9	--	189 ± 6
^{32}Cl [d]	--	--	(^3He, 2nαp), 30.2	(^3He, 2n2αp), 37.5	298 ± 6
^{33}Ar	--	--	(^3He, 2nα), 26.5	(^3He, 2n2α), 33.9	173.8 ± 1.8
^{36}K [c, d]	--	--	(^3He, 2np), 23.1	(^3He, 2nαp), 31.3	340.0 ± 3.3 [g]
^{37}Ca [h]	--	--	(^3He, 2n), 19.8	(^3He, 2nα), 27.2	175 ± 3
^{40}Sc	--	--	--	(^3He, 2np), 24.5	182.4 ± 0.7
^{41}Ti [i]	--	--	--	(^3He, 2n), 21.8	80 ± 2 [j]
^{20}Na	--	(p, αn), 25.0	--	--	446 ± 3
^{23}Al	--	(p, 2n), 30.8	--	--	470 ± 30 [k]

continued.....

Table 4-1 (continued)

Product Nuclide[a]	(Reaction), Threshold (Lab) in MeV — Target: ^{20}Ne	^{24}Mg	^{36}Ar	^{40}Ca	Half-Life[b] (msec)
^{24}Al	--	(p, n), 15.4	--	--	2066 ± 7
^{24}Al^{m}	--	(p, n), 15.8	--	--	130 ± 4

a) Unless otherwise noted, mass-excesses are from (Wa 71).

b) Half-lives are from (Ha 72), except as noted.

c) This nuclide is energetically capable of beta-delayed proton emission, but decays to proton-unbound levels have not been observed.

d) The mass-excess is from (Go 71).

e) This half-life is a weighted average of present and previous (Ha 72) results.

f) Although this does beta-decay to excited states in ^{24}Mg that are both proton- and alpha-unbound, no strong proton decay branches have been observed (To 71).

g) This half-life is from (Go 71).

h) The ^{37}Ca mass-excess is -13.161 ± 0.034 MeV, which is a weighted average of values in Refs. (Bu 68) and (Be 73).

i) The ^{41}Ti mass-excess, -15.78 ± 0.030 MeV, is calculated from the present results.

j) The ^{41}Ti half-life is from this work only (see discussion in Sec. IV D).

k) The ^{23}Al half-life is from the present work.

Table 4-2. Relevant Particle Separation Energies and Q_β(g.s.) Values (Energies in MeV ± keV).

Precursor	Q_β [a]	Refs.	Final System	Separation Energy	Refs.
^{21}Mg	13.095 ± 19	Wa 71	$^{20}Ne + p$	2.432 ± 2*	Wa 71, Bl 69a, Ha 72a
			$^{17}F + \alpha$	6.560 ± 9	Wa 71
^{23}Al	12.238 ± 80	Ce 69	$^{22}Na + p$	7.579 ± 3	Wa 71
^{25}Si	12.736 ± 10	Be 72a	$^{24}Mg + p$	2.271 ± 0.6	Ev 71, Pi 72, Ro 70
^{37}Ca	11.640 ± 34	Bu 68, Be 73	$^{36}Ar + p$	1.857 ± 1	Wa 71
^{40}Sc	14.324 ± 7	Wa 71	$^{39}K + p$	8.330 ± 1	Wa 71
^{41}Ti	12.862 ± 30	b), Al 73	$^{40}Ca + p$	1.086 ± 1	Al 73, Wa 71

a) With the exception of ^{41}Sc, the mass-excesses for the $T_z = -1/2$ nuclei are from (Wa 71).

b) The mass-excess for ^{41}Ti is computed from the present results (see Sec. IV D).

* A recent $^{20}Ne(p,\gamma)$ measurement reported by J. Dubois, et al., Physica Scripta 5, 183 (1972), gives $E_x = 3543.7 \pm 0.4$ keV, for the 3.54-MeV state. Combining this with the resonance energy reported in (Bl 69a), a more accurate $E_{sep.} = 2.4109 \pm 0.0004$ MeV results. Clearly this has no effect on the beta decay results reported here using the tabulated value of 2.432 ± 0.002 MeV. This newer value was reported too late to have been included here.

^{212}Po and attempt to correct for detector dead-layer effects, source thicknesses and charge collection, clearly the most accurate standards are protons from precisely-known states in the beta daughters.

1. Decay energies of the lowest T = 3/2 states

The excitation energies of T = 3/2 states in the A = 4n+1, T_z = -1/2 nuclei have been accurately measured by a variety of techniques (see references in Table 4-3 below): radiative capture, resonance scattering, and particle transfer reactions. These same states can be produced and detected through beta-delayed proton decay, and as a simple cross-check of their reported energies, protons from the decay of these states have been measured using the helium-jet system. These results have been reported in Ref. (Go 73).

The T = 3/2 states in ^{21}Na, ^{25}Al, ^{37}K, ^{41}Sc and ^{29}P were studied in this way. Their respective precursors, ^{21}Mg, ^{25}Si, ^{37}Ca, ^{41}Ti and ^{29}S, were produced in the (^{3}He, 2n) reaction on ^{20}Ne, ^{24}Mg, ^{36}Ar, ^{40}Ca and ^{28}Si targets, respectively. The first four of these nuclides are discussed in greater detail in the ensuing parts of Sec. IV. The mass-29 system was not investigated beyond this cross-calibration experiment. A ^{28}Si target ~1.0 mg/cm^2 thick was used for the production of ^{29}S.

Bombardment of each target alternated with short bombardments of a ^{24}Mg target in order to use the relatively high yield ^{25}Si product as a source of protons to monitor any electronic gain shifts. A precision pulser was also employed to follow any electronic instabilities. The ^{36}Ar (^{3}He, 2n) ^{37}Ca experiment was done at a 40 MeV bombarding

energy, while the four remaining reactions were done at the lower beam energy of 29.5 MeV.

Delayed protons were detected in a 48-μm ΔE 500-μm Σ telescope. For these cross-calibration measurements a total experimental resolution of 30 keV FWHM was achieved. Proton energies were corrected for any small shifts in gain, and for detector dead layers. Since the log ft values are typically ~3.3 (Ha 65) for superallowed beta decay populating the T = 3/2 states in this mass region, the concomitant beta-decay branching ratios to these states are significant (for A > 17). The narrow peaks arising from the isospin-forbidden proton decay of these T = 3/2 states are therefore prominent in each spectrum and can be readily identified.

Delayed-proton spectra from ^{25}Si and ^{41}Ti are shown in Fig. 4-1. As discussed in detail later, the T = 3/2 state in ^{25}Al shows proton decay branches to excited states in ^{24}Mg. Part (a) shows the spectrum from ^{25}Si; peaks 1 and 2 are proton decay peaks from the T = 3/2 level in ^{25}Al to the ground state and first-excited state in ^{24}Mg. Part (b) shows protons from excited states in ^{41}Sc, fed by positron decay from ^{41}Ti; peak 3 is the proton decay of the lowest T = 3/2 state in ^{41}Sc to the ^{40}Ca ground state.

The results of these measurements are shown in Table 4-3, where the center-of-mass (c.m.) proton energies are compared to those deduced from the previous experimental determinations. Decay protons from the lowest T = 3/2 states in ^{25}Si and ^{37}Ca have been used as calibration points, in part since these energies are the most precisely known (see Table 4-3 for references). In addition, the first-

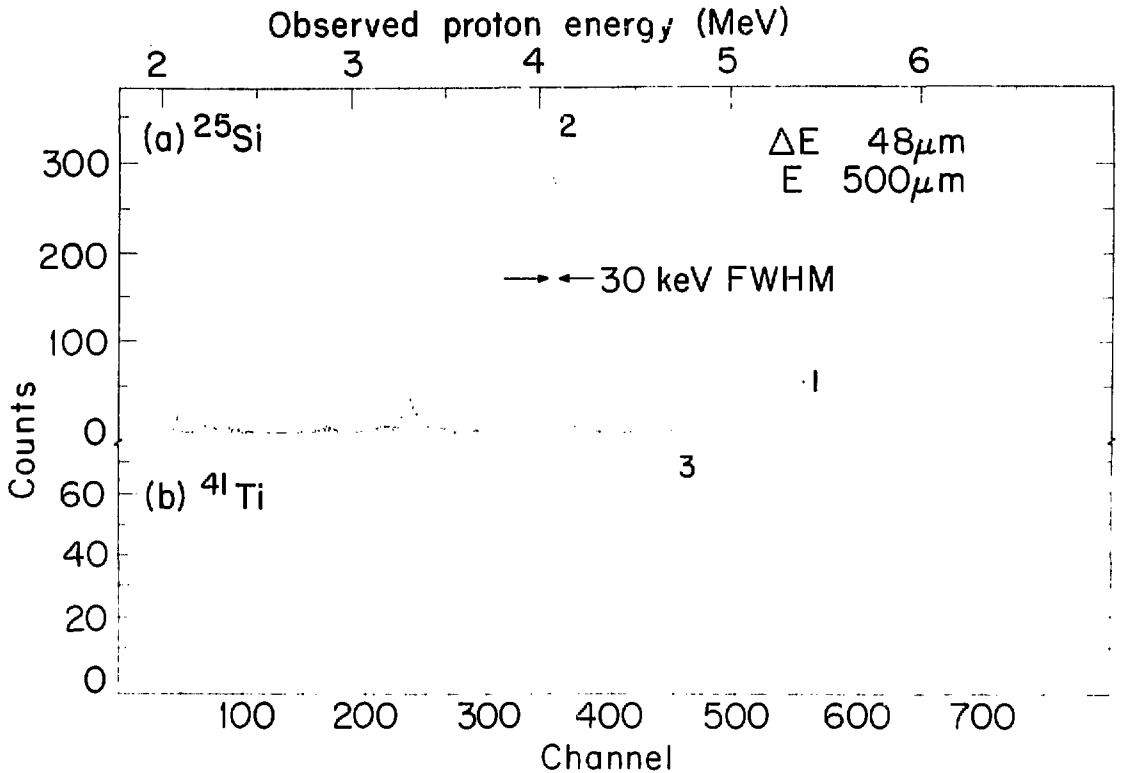

XBL 729-4063

Fig. 4-1. Identified protons following beta-decay of (a) ^{25}Si and (b) ^{41}Ti. The numbered peaks arise from proton decay of the respective T = 3/2 levels in masses 25 and 41, as described in the text.

Table 4-3. Proton Decay Energies (center-of-mass) of the Lowest T=3/2 States

Precursor	Final State in Proton Daughter	Proton decay (c.m.) energies (MeV ± keV) — Deduced from Previous Work	Refs.	Present Results	Weighted Average
^{37}Ca	^{36}Ar (g.s.)	3.1898 ± 2.4	Go 67, Be 73	calibrant	
^{25}Si	^{24}Mg (1x)[a]	4.2623 ± 2.8	Mo 68, Te 69a Be 73a	calibrant	
^{41}Ti	^{40}Ca (g.s.)	4.779 ± 4	En 67, Te 69 Gr 68	4.851 ± 6	4.851 ± 6 [b]
^{21}Mg	^{20}Ne (1x)[c]	4.908 ± 5	Mc 69	4.898 ± 6	4.904 ± 4
^{25}Si	^{24}Mg (g.s.)	5.6309 ± 2.8		calibrant	
^{29}S	^{28}Si (g.s)	5.633 ± 4	Yo 66, Mo 68, Te 69a, Ba 72	5.633 ± 6	5.633 ± 3 [d]
^{21}Mg	^{20}Ne (g.s.)	6.542 ± 5		6.533 ± 6	6.538 ± 4

a) Excitation energy of the first-excited state in ^{24}Mg is from (En 67).

b) This is not a weighted average, but from this work only.

c) Excitation energy of the first-excited state in ^{20}Ne is from (Aj 72).

d) By combining this average with the resonance energy measurements of (Yo 66), (Te 69a), and (Ba 72) with the direct excitation energy measurements of (Mo 68) and (Ba 72), an improved value of the ^{29}P ground-state mass-excess of -16.949 ± 0.004 MeV results.

excited state in ^{24}Mg is well-known (En 67), so the two proton peaks from ^{25}Si shown in Fig. 4-1 differ in energy by a precisely known amount.

With the exception of the 72 keV discrepancy for the ^{41}Sc result, the other nuclides, ^{21}Na and ^{29}P, give values in excellent agreement with the previous measurements and are a unique check on the self-consistency of the T = 3/2 state excitation energies. For ^{41}Sc, the previous T = 3/2 state assignment (En 67, Te 69, Gr 68) is in substantial disagreement with the present result. This reassignment has been confirmed by recently reported results (Tr 73) from ^{40}Ca($\vec{p}$, p) studies from which J^{π} can be uniquely determined. The result of this resonance experiment has been combined with the present measurement to give the proton decay energy listed in Table 4-4 below.

2. Additional energy calibrants

In addition to the proton decay energies from T = 3/2 states just described, other well-known states in ^{21}Na and ^{25}Al exhibit strong proton decay peaks that can serve as energy calibrants. These states are lower in excitation, and their resulting low-energy protons (E_p (lab) < 2 MeV) are important in establishing a low-energy calibration. These states, their respective proton decay energies and the energy regions of interest are tabulated in Table 4-4. Also listed is similar information on the T = 3/2 states discussed above.

Table 4-4. Delayed-Proton Peaks Used as Energy Calibrants
(Energies in MeV ± keV)

Precursor	Excitation in Emitter	Ref.	Final State in Daughter	Proton Energy (Lab)	Reaction and Proton Energy Range a)
^{21}Mg	3.545 ± 2	Va 64, Bl 69a Ha 72a	^{20}Ne g.s.	1.060 ± 0.4	A(2, 3)
	4.294 ± 3	Va 64, Bl 69a Ha 72a	g.s.	1.773 ± 2	A(2, 3)
	4.468 ± 5	Va 64	g.s.	1.939 ± 5	A(2, 3)
	8.970 ± 4	Table 4-3	g.s.	6.225 ± 4	A(1), D(1)
	8.970 ± 4	Table 4-3	1.634	4.669 ± 4	A(1, 2), D(1)
^{25}Si	4.197 ± 1	Ro 70, Br 73	^{24}Mg g.s.	1.849 ± 1	B(2), D(2, 3), E(3)
	4.582 ± 1	Ro 70, Br 73	g.s.	2.218 ± 1	B(2), D(2, 3), E(3)
	4.582 ± 1	Ro 70, Br 73	1.369	3.905 ± 2	B(2), D(3), E(3)
	7.902 ± 3	Table 4-3	g.s.	4.091 ± 3	A(1), B(1, 2), C(1), D(1, 2)
	7.902 ± 3	Table 4-3	1.369	5.404 ± 3	A(1), B(1, 2), C(1), D(1, 2)
^{37}Ca	5.047 ± 3	Table 4-3	^{36}Ar g.s.	3.103 ± 3	C(1)
^{41}Ti	5.939 ± 4 b)	Table 4-3, Tr 73	^{40}Ca g.s.	4.734 ± 4 b)	D(1, 2)

continued. . .

Table 4-4 (continued)

a)

Reaction	Proton Energy Range (Lab)
A. $^{20}Ne + {}^{3}He$	1. $E_p > 2.3$ MeV only
B. $^{24}Mg + {}^{3}He$	2. 0.7 MeV < E_p < 5.5 MeV
C. $^{36}Ar + {}^{3}He$	3. $E_p < 3$ MeV only
D. $^{40}Ca + {}^{3}He$	
E. $^{40}Ca + p$	

b) Weighted average of present result and that from (Tr 73).

The ^{23}Al experiments used two methods of energy calibration. For those results obtained using the pulsed-beam method, low-energy protons, accelerated as H_2^+ beams, were elastically scattered directly into the detector telescopes by a thin Au foil. The beam energies, as measured in an analyzing magnet (Hi 69), were 0.63 and 1.15 MeV/nucleon. Secondly, for those ^{23}Al experiments using the helium-jet system, delayed-protons from ^{40}Sc were used as energy calibrants. (These results are discussed in more detail in the ^{23}Al and ^{40}Sc sections, respectively.)

B. Results for ^{21}Mg

The earlier prediction (Wi 70a) of a mirror beta-decay-rate asymmetry proportional to decay energy, as shown by Eq. 1-1, yields $(\underline{ft})^+/(\underline{ft})^- \sim 1.07$ for mass 21. However, the previous ^{21}Mg data (Ha 65a, Ve 68), when compared to ^{21}F negatron decay rates, show strong disagreement with this prediction. These earlier delayed-proton experiments were hampered by a large, low-energy background, relatively poor energy resolution, and a limited observable energy range.

The results discussed here have been reported in Ref. (Se 73).

1. Discussion of data

The ^{21}Mg experiments were done at 29.5 MeV, on a Ne-He gas mixture. As can be seen from Table 4-1, this bombarding energy is sufficient to produce ^{20}Na, but avoids the possibility of producing ^{17}Ne.

a. Proton spectra. An identified proton spectrum obtained with an 11-μm ΔE 265-μm E detector telescope is shown in Fig. 4-2. The energy region between 2.3 and 7.5 MeV, acquired with 50-μm ΔE and

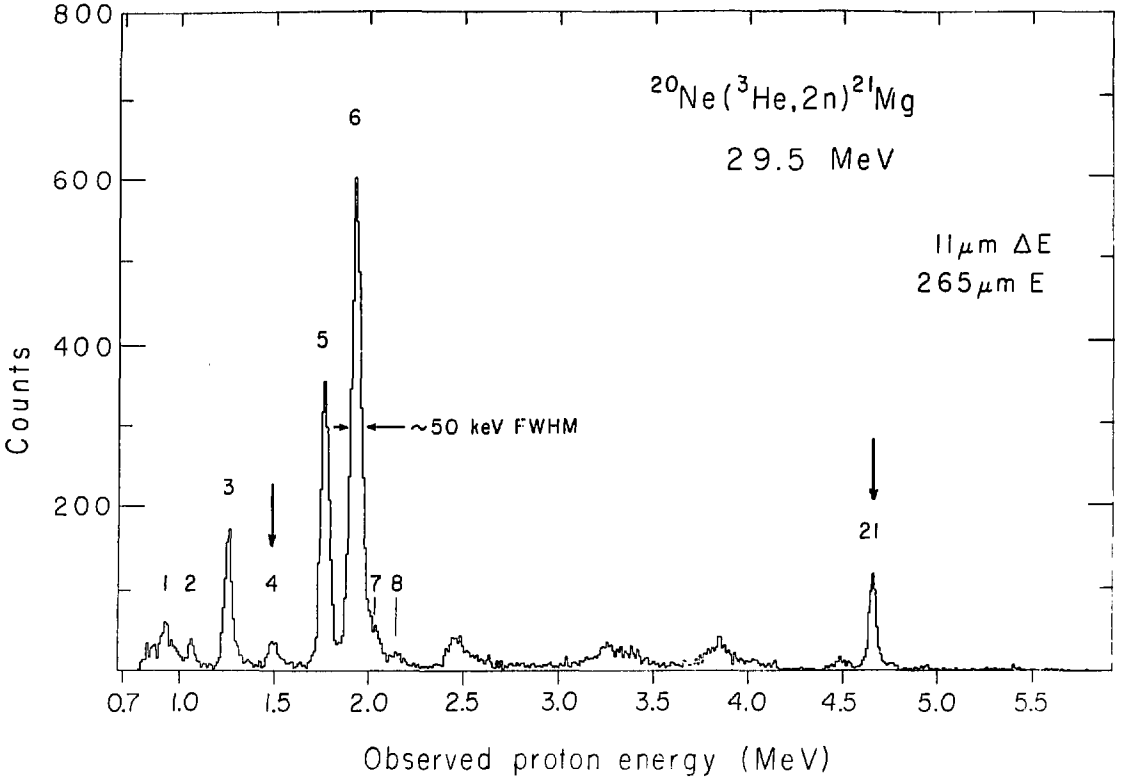

XBL 7210-5776

Fig. 4-2. An identified proton spectrum acquired with the counter telescope noted in the figure. All peaks are associated with the decay of ^{21}Mg and are numbered to correspond with the data listed in Tables 4-5 and 4-6. The vertical arrows denote decays from the T = 3/2 state in ^{21}Na.

500-μm E counters, is shown in Fig. 4-3, with better statistics than in Fig. 4-2. The numbers above the peaks correspond to the peak numbers and decay assignments in Tables 4-5 and 4-6 below. Additional data taken with a 6-μm ΔE 50-μm E telescope are shown in Fig. 4-4, spanning the low-energy proton range from 0.6 to 2.2 MeV.

No known β^+-delayed proton precursors could be produced from likely contaminants in the target gas. Although ^{20}Na can, in principle, decay via electron capture to proton unbound levels in ^{20}Ne, the resulting maximum proton energy (lab) would be $\leq$ 1.0 MeV (Go 71, Wa 71). The half-lives exhibited by all statistically significant peaks in the sequential time-routed data were found to be consistent with the ^{21}Mg half-life. Hence the proton spectra obtained consist solely of decay peaks from break-up of proton unbound levels in ^{21}Na.

Between proton lab energies of 2.4 to 4.3 MeV, the spectra are composed primarily of three sets of multiple peaks, making the extraction of accurate intensities difficult. Figure 4-5 shows a typical decomposition of one set of multiple peaks using the Gaussian peak-fitting program described in Sec. III E. The energies, intensities and widths of peaks 9 through 19 remained consistent for data from three separate experiments when analyzed in this manner.

The energy calibrants used to obtain the proton peak energies are listed in Table 4-4. The resulting lab energies for the 25 proton peaks are shown in Table 4-5, along with the relative intensities for each peak; these numbers are averages over several different experiments. The energy resolution achieved in these experiments is shown in each spectrum; typically momentum broadening from the preceding β^+ decay

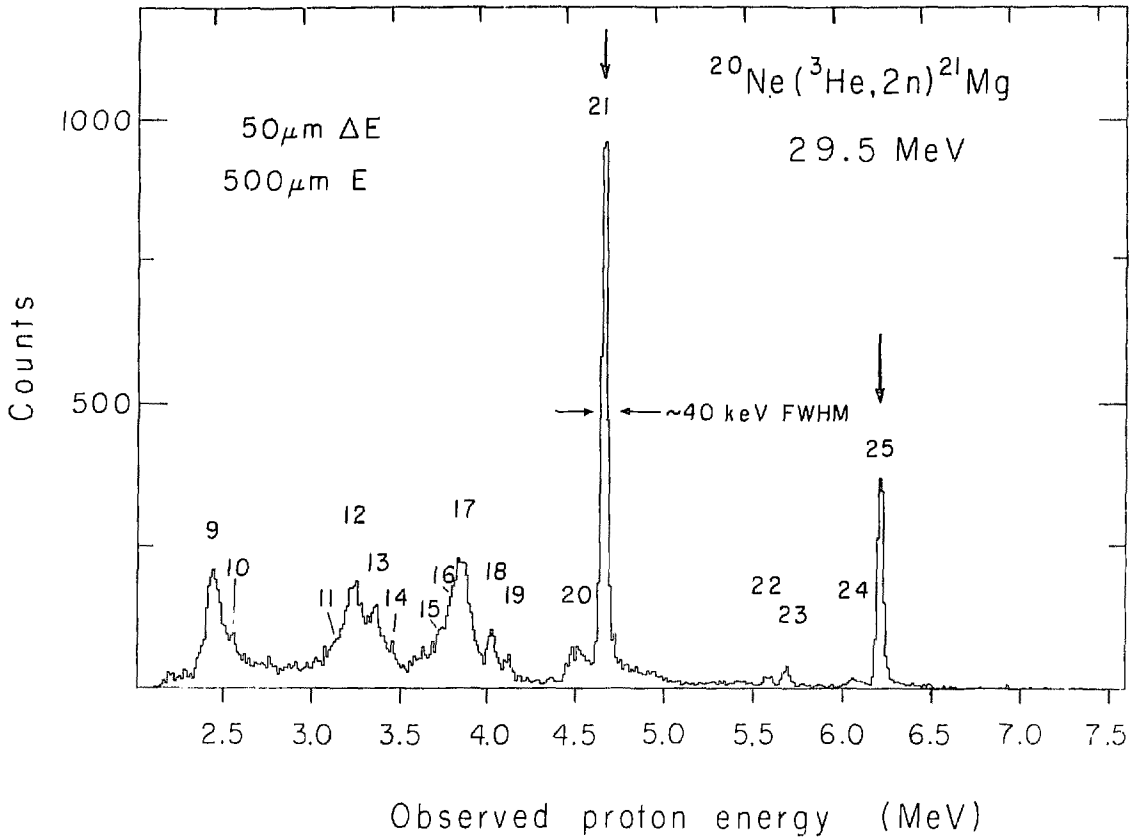

XBL 7710-7777

Fig. 4-3. Delayed protons from ^{21}Mg with energies greater than 2.3 MeV. Again the numbers correspond to proton decay data shown in Tables 4-5 and 4-6; the vertical arrows point to peaks arising from the T = 3/2 state decay.

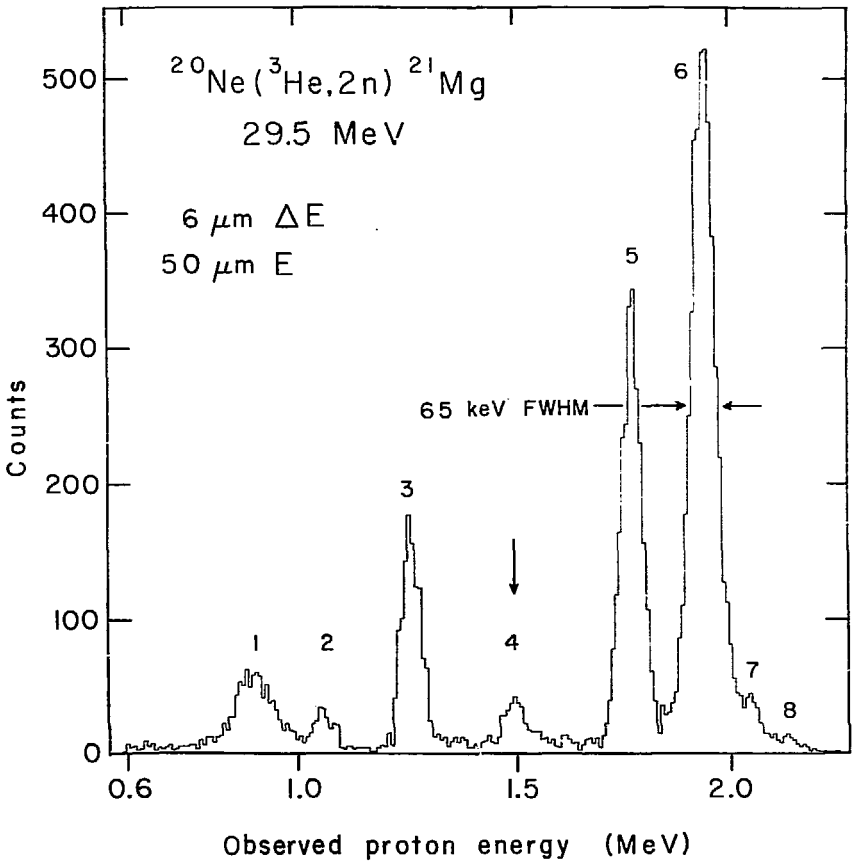

XBL 7311-6805

Fig. 4-4. Low-energy proton spectrum following the decay of ^{21}Mg. The peak numbers and arrows have the same connotation as in Figs. 4-2 and 4-3.

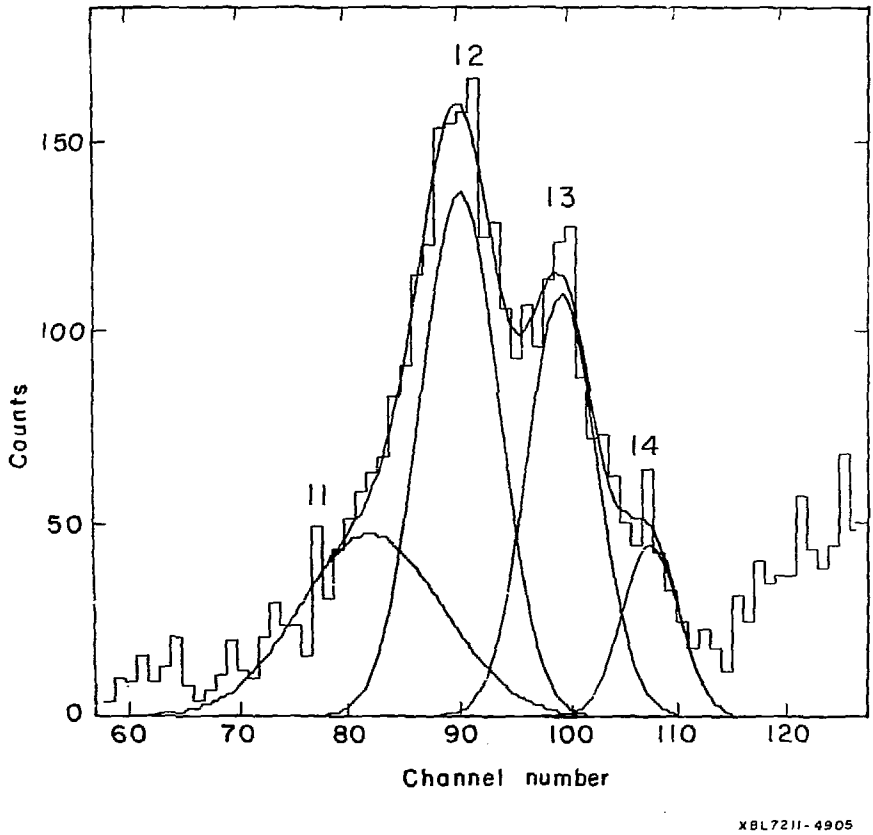

Fig. 4-5. A sample multiple-peak group with proton energies between 3.0 and 3.5 MeV analyzed using a Gaussian peak-fitting program (see discussion in text). The numbering system and data are identical to that in Fig. 4-3.

Table 4-5. Observed proton energies and relative intensities for the delayed-proton decay of ^{21}Mg. The peak numbers correspond to the identification numbers shown in Figs. 4-2, 4-3, and 4-4.

Peak Number	E_p (Lab) MeV ± keV	Relative Intensity[a] (%)
1	0.902 ± 20	16.6 ± 0.5
2	1.060 ± 0.4[b]	4.3 ± 0.6
3	1.257 ±10	23.3 ± 1.7
4	1.498 ±10	6.3 ± 0.6
5	1.773 ± 2[b]	51.4 ± 2.0
6	1.939 ± 5[b]	100.
7	2.042 ±15	8.3 ± 1.0
8	2.157 ±25	4.6 ± 0.4
9	2.474 ±20	7.6 ± 2.0
10	2.588 ±30	2.9 ± 1.0
11	3.167 ±35	3.3 ± 0.2
12	3.271 ±25	5.9 ± 0.3
13	3.377 ±15	4.5 ± 0.5
14	3.487 ±35	1.35± 0.10
15	3.600 ±50	1.3 ± 0.2
16	3.742 ±35	3.6 ± 0.5
17	3.873 ±20	10.3 ± 0.4
18	4.043 ±25	2.46± 0.20
19	4.142 ±20	1.0 ± 0.2
20	4.514 ±15	2.5 ± 0.5
21	4.669 ± 4[b]	14.4 ± 0.7
22	5.584 ±15	0.48± 0.05
23	5.699 ±15	0.73± 0.06
24	6.081 ±25	0.57± 0.10
25	6.225 ± 4[b]	5.5 ± 0.1

a) These are relative to the most intense proton group - peak 6.
b) Energy calibrant, see discussion in Sec. IV A.

contributed 5 to 14 keV to this width (see Table 3-1). These measurements, covering a broad energy range, include all the significant proton decays of those unbound levels in ^{21}Na fed by the positron decay of ^{21}Mg.

b. α-particle spectrum and results. States in ^{21}Na above 6.56 MeV are unbound to α decay to ^{17}F, as noted in Table 4-2. In particular, the lowest T = 3/2 state is α-unbound by 2.4 MeV (Wa 71). This nuclide is the heaviest member of the T_z = -1/2, A = 4n+1 series whose lowest T = 3/2 state is α-unbound (both alpha- and proton- decay branches are exhibited by the T = 3/2 level in ^{13}N (Ad 73) while an upper limit for α decay has been obtained for decay of the T = 3/2 state in ^{17}F (Ha 71, Ad 73)). Simple barrier-penetrability predictions (following the prescription in Sec. II D) for ℓ = 0 α emission from the ^{21}Na T = 3/2 level to the ^{17}F ground state suggest that, as an upper limit, this (isospin-forbidden) decay is relatively unhindered by the Coulomb barrier. In fact, the penetrability for this decay is comparable to that calculated for the proton decay of this state to the third-excited state in ^{20}Ne, as shown in Table 4-7 below.

An experimental search for this possible decay mode employed a 4-μm ΔE 48-μm E detector telescope; α-particles with energies as low as 1.4 MeV could be reliably identified. The resulting spectrum is shown in Fig. 4-6; as can be seen, the β^+-delayed α decay of ^{20}Na dominates the spectrum. Since proton data from delayed-proton decay of ^{21}Mg were collected simultaneously, direct comparison of the intensities establishes a limit for this possible decay branch of $< 1.6\%$ relative to the total proton decay.

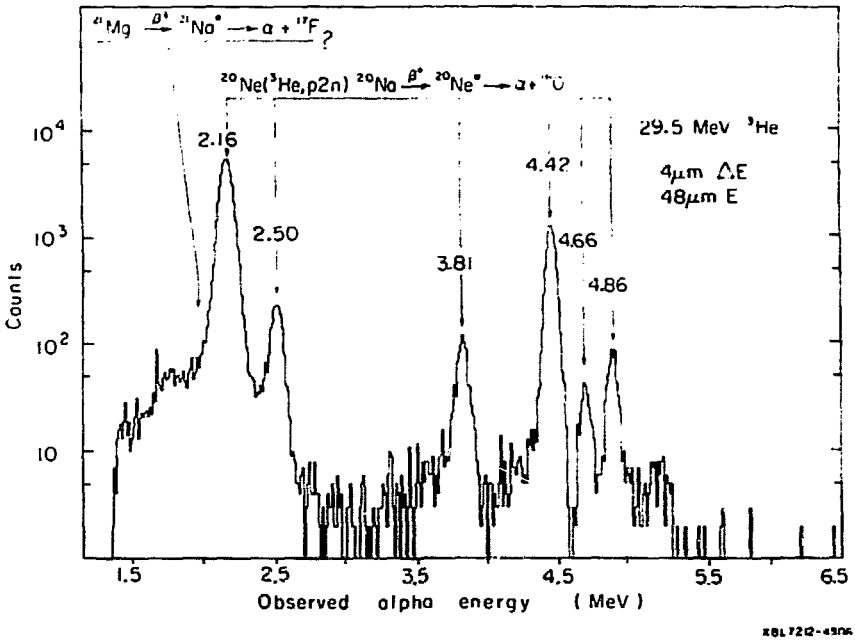

Fig. 4-6. Identified α-particle spectrum following ^{3}He bombardment of ^{20}Ne. The predicted location for α particles from decay of the ^{21}Na T = 3/2 state is shown by the arrow at lowest energy. The remaining arrows indicate α-particle groups and their respective laboratory energies (in MeV) following the β^+ decay of ^{20}Na.

The energy calibration scale for the α-particle spectrum was taken from the known decays of the 7.42-and 10.26-MeV levels (Aj 72) in ^{20}Ne, which result in α energies (lab) of 2.16 and 4.42 MeV respectively. Using these as calibrants, the deduced energies of the other major peaks arising from ^{20}Na decay are shown in Fig. 4-6, along with the location of the potential 1.95-MeV α particle from ^{21}Na (T = 3/2). The intensities of these peaks relative to the 2.16 MeV peak (100%) are: 2.50 (4.5%); 3.81 (1.8%); 4.42 (17.8%); 4.66 (0.6%); 4.86 (1.3%). These energies and intensities agree with the recently published results for β^+-delayed alpha decay of ^{20}Na (To 73a).

c. Half-life measurements. Since ^{21}Mg is the only known delayed-proton precursor present in the spectra, no systematic errors from contaminant activities should be present to distort the measured lifetime. Combining data acquired using the two methods described in Sec. III C, the present determination of the ^{21}Mg half-life (resulting from four independent experiments) is 123.1 ± 3.3 msec. This compares well with the previously reported ^{21}Mg half-life of 121 ± 5 msec (Ha 65a), and gives a weighted average of 122.5 ± 2.8 msec. This average value has been used for all subsequent calculations and results.

2. Analysis

a. Assignment of energy levels. The center-of-mass proton energy and the parent state in ^{21}Na for each of the peaks in Table 4-5 are given in Table 4-6. Unfortunately some ambiguities remain regarding a few of these assignments for the observed proton peaks. Such uncertainties arise due to the two or more decay modes available to states above ~5 MeV in excitation. The energy levels of ^{21}Na up to ~5 MeV have been extensively

Table 4-6. Proton energies from the decay of unbound levels in ^{21}Na fed by β^+-decay of ^{21}Mg, and a comparison of ^{21}Na energy levels inferred from this work with previous results. Underlined numbers preceding each entry correspond to peak-identification numbers shown in Figs. 4-2, 4-3, and 4-4. (All entries given as MeV ± keV).

Proton Energies (c.m.) Corresponding to Decay to the Following Levels in ^{20}Ne:				Deduced[a] Energies in	Previous Work		
g.s.	1.634 MeV	4.247 MeV	4.968 MeV	^{21}Na	En 67	Bu 68	Other
2 1.113 ± 0.4[b]				3.545 ± 2	3.544 ± 8	3.54 ± 20	
5 1.862 ± 2[b]	--[c]			4.294 ± 3	4.294 ± 9	4.28 ± 30	
6 2.036 ± 5[b]	--			4.468 ± 5	4.468 ± 9	4.41 ± 30	
9 2.598 ± 20	1 0.947 ± 20			5.022 ± 15	4.99 ± 50	4.99 ± 30	5.03[d]
X	3 1.320 ± 10			5.386 ± 10		5.34 ± 30	
11 3.326 ± 35	X[c]			5.758 ± 35	5.69	5.78 ± 30	
12 3.435 ± 25	X			5.867 ± 25	5.82		
13 3.547 ± 15	X[c]			5.979 ± 15			
14 3.662 ± 35	X[c]			6.094 ± 35	6.08		
15 3.78 ± 50	X[c]			6.21 ± 50	6.24	6.16 ± 30	
16 3.930 ± 35	8 2.265 ± 25			6.341 ± 20			
17 4.068 ± 20	X			6.500 ± 20	6.51	6.54 ± 30	6.52[f]
22 5.865 ± 15	18 4.246 ± 25	X	X	8.301 ± 15	(8.35)	8.31 ± 30	
23 5.986 ± 15	19 4.350 ± 20	X	X	8.417 ± 15			
24 6.387 ± 25	20 4.741 ± 15	7 2.145 ± 15	X [g]	8.816 ± 10			
25 6.538 ± 4[b]	21 4.904 ± 4[b]	X	4 1.573 ± 10 [g]	8.970 ± 4[h]	8.90 ± 40	8.97 ± 30[i]	
Unassigned proton peak: 10 2.718 ± 30[j]							

continued. . .

Table 4-6 (continued)

a) The energies are calculated using a proton separation energy of 2.432 ± 0.002 MeV (see Table 4-2).

b) These proton energies were used, in part, to determine the energy calibration (see discussion in Sec. IV A).

c) Unobserved, but energetically-allowed, proton decays within the experimental range are marked by X, while those outside this range (≤ 600 keV) are shown by --.

d) Ref. (Am 69)

e) These possible decays were obscured by peaks arising from the decay of other states.

f) Ref. (Be 67a)

g) Possible proton decays from these levels leading to higher excited states in ^{20}Ne are also within the present energy range, but no such decays were observed.

h) This number is based on the average of the delayed-proton results and resonance measurements discussed in Sec. IV A.

i) This number is corrected based on the remeasured mass of ^{10}C (Br 68).

j) The possible origin of this peak is discussed in the text.

studied (Bl 69a, En 67), most recently by Haas, et al. (Ha 72a) using ^{20}Ne (p, γ) and ^{20}Ne (d, n) reactions. In addition the energy levels in the mirror ^{21}Ne nucleus have also been recently investigated (Ro 72), and assignments of mirror levels up to 4.8 MeV have been made for these nuclei (Ha 72a, Ro 72).

States in ^{21}Na populated by allowed beta decay from ^{21}Mg will have J^{π} = 3/2+, 5/2+, or 7/2+, since the ground state spin and parity of ^{21}Mg is presumed to be 5/2+, in analogy with its mirror ^{21}F. Further verification comes from the determination that J^{π} for the lowest T = 3/2 state in each of the $T_z = \pm 1/2$ isobars is 5/2+ (^{21}Ne: Ref. Bu 68: ^{21}Na: Ref. Be 70). It therefore seems reasonably unlikely that additional levels capable of being fed by allowed beta decay could exist for excitation energies < 5 MeV. For this reason, no new levels below 5 MeV are postulated in Table 4-6. Peak 3 has been associated with decay of the 5.39-MeV state to the ^{20}Ne first-excited state, although it could have been assigned a level ~ 3.75 MeV. For reasons just noted, the former assignment appears to be the more correct.

Peak 10, on the other hand, has not been assigned to any level in ^{21}Na, although it certainly arises from the β^+ decay of ^{21}Mg. However, it is not certain whether this relatively weak peak is due to decay to the ground state, or the first-excited state in ^{20}Ne. Although it has not been associated with a parent state in ^{21}Na, the proton intensity is included in subsequent branching ratio determinations.

Three peaks arise from the decay of the T = 3/2 state (denoted by the vertical arrows in Figs. 4-2, 4-3, and 4-4); the proton decay to the second-excited state was not observed, although the resulting peak

would appear in the region of peak 8. This peak, however, consistently exhibits a width three times larger than is observed for the other (isospin-forbidden) decays of the analog state, and so was not associated with the T = 3/2 decay.

Table 4-6 also indicates the comparison of the ^{21}Na energy levels deduced from the present data with those found in the literature (Bu 68, En 67). As noted in Sec. IV A and Table 4-4, proton groups 2, 5, and 6 were used as part of the energy calibration; the corresponding excitation energies result directly from the data of Refs. (Va 64, Bl 69a, and Ha 72a). No comparison with these values is therefore shown under the heading "previous work." Only those energies that reasonably correspond to the excitation energies deduced from the present data are listed in the last three columns of Table 4-6. Although some T = 1/2 states above 5 MeV in ^{21}Na have been established, spin and parity assignments for these states are generally unavailable. As it is difficult to correlate the present results with previous measurements, the energies of excited states above 5 MeV are taken from the present study only and are used for all subsequent calculations.

b. Decay of the T = 3/2 state. The particle decays of the lowest T = 3/2 state in ^{21}Na are shown in Table 4-7. Of the potential decay modes not seen in the present work, penetrability calculations indicate that only proton decay to ^{20}Ne* (4.25 MeV) and α decay to ^{17}F (g.s.) might be expected. An upper limit for each of these two decays has been obtained, but neither is included in the branching ratio and log ft calculations shown below.

Table 4-7. Energies, Branching Ratios and Penetrabilities for Particle Decays of the Lowest T = 3/2 State in ^{21}Na

	Final[a] State (MeV)	J^π	Particle Decay Energy (c.m.)(MeV)	Observed Intensity I(%)	Relative Branching Ratio (%)	Penetrability[c] P	1/P
p + ^{20}Ne	0.000	0+	6.538	1.76 ± 0.12	20 ± 2	0.99	1.8
	1.634	2+	4.904	4.78 ± 0.23	56 ± 3	1.57	3.0
	4.247	4+	2.291	< 0.35		0.061	< 5.7
	4.968	2-	1.573	2.02 ± 0.19	24 ± 2	0.096	21.0
	5.622	3-	0.916	X		0.010	
	5.785	1-	0.753	X		0.004	
α + ^{17}F	0.000	5/2+	2.410	<1.60		0.070	< 23
	0.495	1/2+	1.915	X		0.002	

a) Excited states in ^{20}Ne are from (Aj 72) while for ^{17}F they are from (Aj 71).

b) These are stated in terms of the percent of the total proton decay of ^{21}Na. Possible groups marked X were unobserved, though within range of observation. These results agree qualitatively with the observations in (Mc 69) where resonances were found in the p_0, p_1, and p_3 channels.

c) This is calculated as discussed in Sec. II D, with r_0 = 1.3 fm.

An estimate of the small partial width contribution due to gamma decay of this state can be obtained from the present measurement of Γ_{p_0}/Γ (see Table 4-7) and the results from (Be 70), which gives $\Gamma_\gamma \sim 9$ eV. The total width is ~ 1200-1500 eV (Mc 69, Te 69), so $\Gamma_\gamma/\Gamma \sim 0.75\%$.

c. Branching ratios and ft values. As noted in Sec. II B, several calculations for the transition strength of the superallowed beta decay have been made. The recent shell model calculations of Lanford and Wildenthal (La 73) give $\langle \sigma \rangle^2_{S.A.} \sim 0.27$ for ^{21}Mg. The earlier Nilsson formalism estimates give $\langle \sigma \rangle^2_{S.A.} \sim 0.24$ (Ha 65), in agreement with the shell-model calculations. From the assumption of isospin purity for the T = 3/2 state in ^{21}Na (i.e., $a^2 = 1$ in Eq. 2-20), Eq. 2-14 then gives log ft = 3.26 which in turn yields a calculated branching ratio for this decay. It should be noted from Eq. 2-14 that the ft values are relatively insensitive to $\langle \sigma \rangle^2$. For an uncertainty of up to ± 50% in the estimate of the Gamow-Teller matrix element, the transition strength is affected by ~ 5%, and the subsequent log ft by ~ ±0.02.

The ^{21}Mg proton intensities, relative to the total proton decay from the T = 3/2 state, are thus a measure of the beta decay strength; the beta branching ratio for each unbound level, and hence the partial half-life, can be obtained from these relative proton intensities. These branching ratios are shown in column 4 of Table 4-8 for each unbound level in ^{21}Na. Lack of β-decay data to bound states in ^{21}Na precludes a worthwhile discussion of isospin mixing in its T = 3/2 analogue state.

For beta decay to the bound states, the intensity ratios for these three levels are taken from the mirror $^{21}F \rightarrow {}^{21}Ne\ \beta^-$ decay (Ha 70a).

Table 4-8. Branching Ratios and ft Values for the Positron Decay of ^{21}Mg.

Energy Level[a] In ^{21}Na (MeV)	J^{π}[b]	Proportion of Proton Decays[c] (%)	Branching Ratio[d] From ^{21}Mg (%)	ft[d,e] (10^3 sec)	Log ft (sec)	Theoretical Predictions[f] Log ft (sec)	E_x in ^{21}Na (MeV)	J^{π}
0.000	3/2+		15.8 ± 4.0[g]	182 ± 46	5.26 ± 0.10	5.55	0.000	3/2+
0.332	5/2+		40.7 ± 5.0[g]	62 ± 8	4.79 ± 0.05	4.70	0.314	5/2+
1.723	7/2+		10.9 ± 2.0[g]	126 ± 23	5.10 ± 0.07	4.80	1.800	7/2+
3.545	5/2+	1.38 ± 0.19	0.45 ± 0.07[h]	1200 ± 180	6.09 ± 0.06	8.34	3.592	5/2+
4.294	5/2+	16.48 ± 0.65	5.36 ± 0.31	65.9 ± 3.6	4.82 ± 0.02	5.21	4.445	5/2+
4.468	3/2+	32.09 ± 0.34	10.45 ± 0.46	30.4 ± 1.2	4.48 ± 0.02	4.44	4.353	3/2+
5.022	(5/2+, 3/2+)	7.76 ± 0.68	2.53 ± 0.25	88 ± 8	4.95 ± 0.04	4.67	5.600	3/2+
5.386		7.47 ± 0.55	2.43 ± 0.21	71 ± 6	4.85 ± 0.03	5.33	5.345	7/2+
5.758		1.06 ± 0.06	0.34 ± 0.03	384 ± 27	5.59 ± 0.03	4.99	6.147	7/2+
5.867		1.89 ± 0.10	0.62 ± 0.04	198 ± 13	5.30 ± 0.03	4.84	6.230	3/2+
5.979		1.44 ± 0.16	0.47 ± 0.06	239 ± 28	5.38 ± 0.05	4.82	6.602	7/2+
6.094		0.43 ± 0.03	0.14 ± 0.01	730 ± 60	5.86 ± 0.03	4.65	6.932	5/2+
6.21		0.42 ± 0.06	0.14 ± 0.02	690 ± 110	5.84 ± 0.06	5.68	7.322	7/2+
6.341		2.63 ± 0.19	0.86 ± 0.07	98 ± 8	4.99 ± 0.03	4.59	7.588	3/2+
6.500		3.29 ± 0.13	1.07 ± 0.06	69.1 ± 3.8	4.84 ± 0.02	4.73	7.689	5/2+
						4.24	8.264	5/2+
8.301		0.94 ± 0.07	0.31 ± 0.03	40.2 ± 3.3	4.60 ± 0.03	3.81	8.672	5/2+
8.417		0.55 ± 0.07	0.18 ± 0.02	59 ± 8	4.77 ± 0.05	4.67	8.685	5/2+
8.816		3.65 ± 0.36	1.19 ± 0.13	5.4 ± 0.6	3.73 ± 0.04	5.93	8.861	7/2+
8.970	5/2+, T=3/2	8.56 ± 0.33	2.79 ± 0.16	1.80	3.26	3.26	8.993	5/2+, T=3/2
E_p = 2.718[i]		0.93 ± 0.32	0.30 ± 0.11					

continued . . .

Table 4-8 (continued)

a) Energies of bound states (below 2.43 MeV) are taken from (Ha 72a) while the remaining three levels below 5 MeV are discussed in the text. The energies above 5 MeV are from the present work only.

b) Spins and parities are from (Ha 72a).

c) The sum of the proton decays equals 91.0% since there is a 9.0% proton "background" made up of decays apparently due to weakly populated, broad levels too weak to analyze.

d) The branching ratios and ft values are calculated assuming complete isospin purity of the T=3/2 state, and allowance has been made for the 0.75% gamma-decay branch from this level (see text).

e) The ft values are calculated using the Q_β listed in Table 4-2, and a half-life of 122.5± 2.8 msec.

f) These calculations are from (La 73). For the predicted T = 1/2 states between 6 to 9 MeV, no general attempt was made to correlate these individual levels with the experimental results.

g) These branching ratios were calculated from comparison to the mirror ^{21}F decay (Ha 70a).

h) This value has been corrected for the $\Gamma_\gamma/\Gamma \sim 2.5\%$ (Bl 69a).

i) This unassigned peak is discussed in the text. Only the decay energy is listed, since the level from which it originates is uncertain.

The resulting branching ratios are also given in Table 4-8. In addition to these three allowed β-decay transitions, Harris and Alburger (Ha 70a) also reported an upper limit for the negatron branch leading to the 2.790-MeV state in ^{21}Ne. Rolfs, et al., (Ro 72) have subsequently reported $J^{\pi} = 1/2$- for this state, consistent with its assigned mirror in ^{21}Na. Hence there is a level at 2.80 MeV in ^{21}Na potentially fed by first-forbidden unique beta decay. However, since only an upper limit for this decay has been established (i.e., a lower limit on the ft value), the present calculations for the branching ratios for ^{21}Mg β^+ decay ignore this possibility.

Calculations of the statistical rate function, f, were made for each positron decay shown in Table 4-8 following the method discussed in Sec. II A. The consequent ft values, and their logarithms are tabulated in columns 5 and 6. The shell model predictions for energy levels and β-decay transition rates in mass 21 are taken from (La 73), and are listed in the last three columns of Table 4-8. These calculations used a complete sd shell basis space for the five nucleons outside an ^{16}O c. e. Log ft values were obtained for the $T = 1/2$ levels with $J^{\pi} = 3/2+$, $5/2+$, and $7/2+$, as well as for the lowest $T = 3/2$ level (see additional discussion below).

The deduced energy levels in ^{21}Na, and the beta decay branching ratios and log ft values resulting from the data presented here are summarized in the ^{21}Mg decay scheme in Fig. 4-7. For those $T = 1/2$ states having more than one observed decay branch, the proton intensities and reduced-width ratics are listed in Table 4-9.

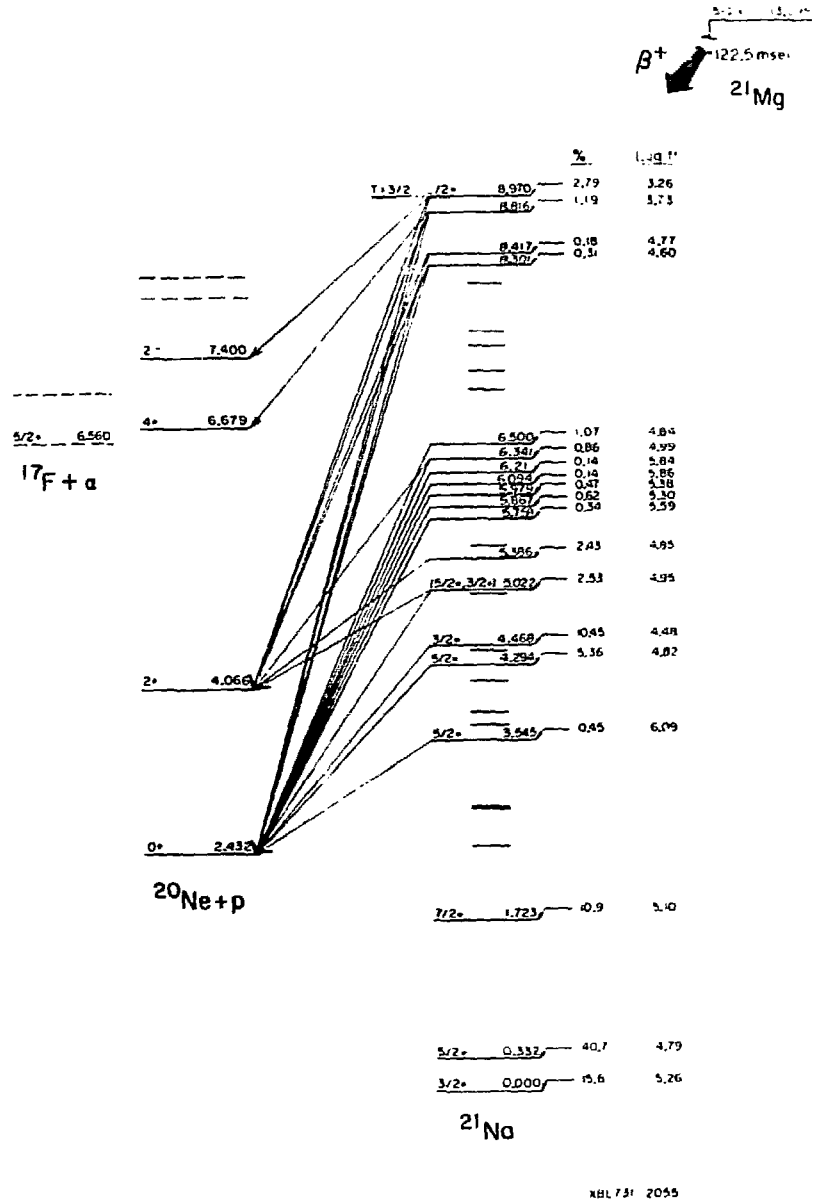

Fig. 4-7. Proposed decay scheme for ^{21}Mg. The excitation energies above 5 MeV in ^{21}Na are taken from this work (except the 8.970-MeV state). β^+-decay branching ratios and log *ft* values are also listed.

Table 4-9. Relative Branching Ratios and Reduced Widths for the Decay of $T = 1/2$ States in ^{21}Na

E_x in ^{21}Na (MeV)	Intensity[a] of Proton Decay			Intensity Ratios		Ratio of Reduced Widths[b]			
						1x/gs		2x/gs	
	To g.s.	To 1x	To 2x	1x/gs	2x/gs	3/2+,5/2+	7/2+	3/2+,5/2+	7/2+
5.022	2.44 ± 0.64	5.32 ± 0.17		2.2		4.3	--	--	
6.341	1.15 ± 0.16	1.47 ± 0.13		1.3		0.73	0.11	--	
8.301	0.15 ± 0.02	0.79 ± 0.06		5.3		3.2	0.48	--	
8.417	0.23 ± 0.02	0.32 ± 0.06		1.4		0.85	0.13	--	
8.816	0.18 ± 0.03	0.80 ± 0.16	2.66 ± 0.32		14.8	2.8	0.46	310	1.6

a) This is quoted as the percentage of the total proton decays from ^{21}Na.

b) The reduced widths are calculated by dividing the observed intensity by the penetrability for the decay (using the lowest possible ℓ) assuming the state has $J^\pi = 3/2+$, $5/2+$, or $7/2+$. The penetrabilities were evaluated using $r_0 = 1.3$ fm.

3. Discussion and conclusions

a. Comparison of experimental and theoretical results. The major experimental and theoretical results appearing in Table 4-8 have been illustrated in Fig. 4-8. Enough data exist to permit comparisons of theoretical and experimental β-decay transition rates to levels up through 5.6 MeV in excitation. Such a comparison shows excellent agreement except for the decay to the 3.5-MeV state, for which a strongly hindered transition is predicted. Although the present results indicate that this decay has a considerably greater strength than predicted, it is the weakest of all the (allowed) β-decay rates measured. Qualitatively the difference between experiment and theory for this case probably represents only a small change in the matrix element cancellations arising from details of the wavefunctions.

Based on known spins and parities for states at 4.294 and 4.468 MeV, the predicted levels at 4.35 ($J^{\pi} = 3/2+$) and 4.45 MeV ($J^{\pi} = 5/2+$) have been inverted in order that the known and predicted spins correspond. The level at 5.022 MeV has been tentatively assigned $J^{\pi} = (3/2, 5/2)+$, based on earlier measurements (Ha 72a). The shell model calculations show a state at 5.60 MeV with $J^{\pi} = 3/2+$, while the next available 5/2+ state is predicted to be at 6.9 MeV. Thus the two predicted levels at 5.35 and 5.60 MeV have been exchanged in Table 4-8 to align these possible 3/2+ states. (The alignment of these pairs of levels is shown in Fig. 4-8 by dashed lines.)

A more circumstantial case may be made for correlating the experimentally deduced level at 5.386 MeV with that calculated to be at 5.35 MeV. The measured and predicted beta-decay rates show moderate

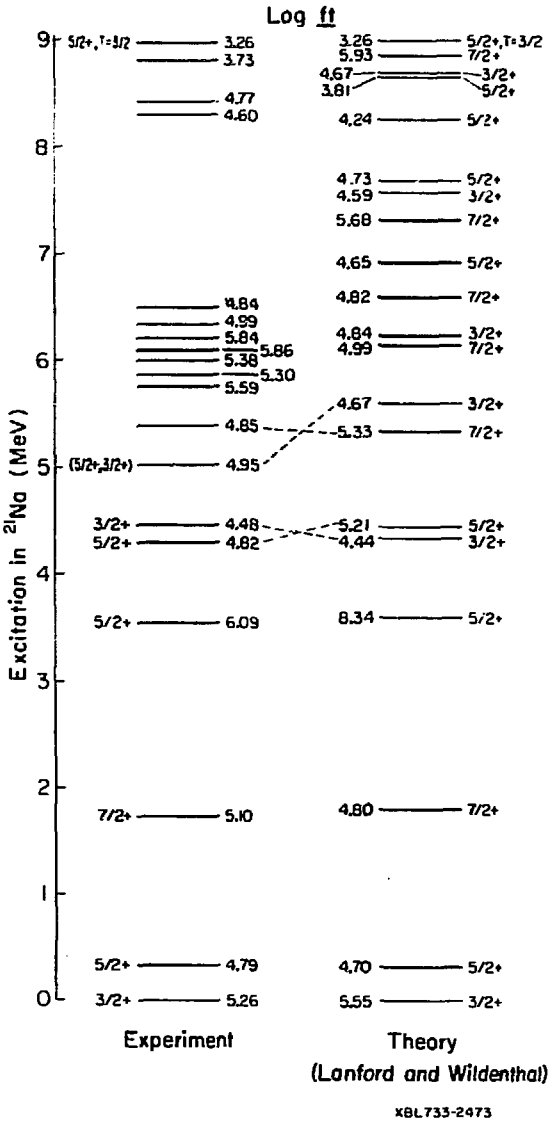

Fig. 4-8. Experimental and theoretical excitation energies and log ft values for states in ^{21}Na populated by allowed β^+ decay of ^{21}Mg.

agreement, and a state at 5.34 MeV has been identified by Butler, et al., (Bu 68) in ^{23}Na(p, t). If this state has $J^{\pi} = 7/2+$, the two neutron transfer could readily proceed via L = 2 pickup, while a ^{20}Ne (p, p) resonance experiment would require $\ell = 4$. This might explain why no level at this excitation has been reported from such resonance experiments.

Of the 16 $J^{\pi} = 3/2+, 5/2+, 7/2+$ T = 1/2 levels predicted above the proton separation energy, 15 levels with log ft values consistent with allowed Gamow-Teller decay have been experimentally located, plus one additional unassigned proton decay peak that almost certainly belongs to a separate, though unidentifiable level. The sum of the predicted strengths to the first eight states in ^{21}Na (up through 5.6 MeV) is 90% of the total calculated decay strength from ^{21}Mg, while these experimental results indicate 89% of the total β^+ decay populates these states. Individual comparisons of the predicted and experimental transition strengths for decay to these low-lying levels show a difference of less than 10% between log ft values (with the exception of the 3.5-MeV state noted previously). This reinforces the 5% (rms) and 12% (maximum) deviation in the logarithms found by Lanford and Wildenthal (La 73) in a more general study of theoretical vs experimental log ft values in the mass ranges A = 17 to 22 and 35 to 39.

The level at 8.816 MeV exhibits a relatively fast β-decay transition rate (Go 66). It should be emphasized that this strength is predicated on the assignment of peaks 7,20, and 24 to this level (cf. Table 4-6), which is a reasonable assumption based on observed decay energies and widths. If one assumes that mixing between this level and the

8.970-MeV, T = 3/2 state (assuming identical J^{π}) might simply account for this enhanced decay strength, the necessary T = 3/2 admixture can be estimated from Eq. (2-22). However, the resulting admixture of ~30% would imply both an unusually strong charge-dependent matrix element, and an isospin impurity of the T = 3/2 state considerably greater than that experimentally determined for T = 3/2 states in ^{17}F, ^{33}Cl (Ha 71) or ^{41}Ti (see later discussion in Sec. IV D). Further, if such substantial mixing were to occur between these levels, one might expect the particle decay modes of these states to be similar. Tables 4-7, 4-9, and Fig. 4-7 indicate that this is not the case. Lanford and Wildenthal (La 73) in fact predict a log $\underline{ft}$ = 3.81 for a 5/2+ state at 8.67 MeV (see Table 4-8 and Fig. 4-8), which compares remarkably well with the experimental value for the 8.816 MeV state (log $\underline{ft}$ = 3.73). It therefore seems quite plausible that these levels in fact correspond.

b. Mirror decay rates. From the assumption of isospin purity for the lowest T = 3/2 state in ^{21}Na, and the resulting β^+-decay transition rates to other levels in ^{21}Na, the expected half-life for the mirror β^- decay of ^{21}F can be estimated. As noted previously, the mirror levels in ^{21}Na and ^{21}Ne have been assigned up to 5 MeV (Ro 72). Hence partial half-lives for allowed β^- decay to the first six levels with J^{π} = (3/2, 5/2, or 7/2)+ in ^{21}Ne can be calculated from the present experimental values of $(\underline{ft})^+$ for positron decay to the analogs in ^{21}Na. Comparison of this predicted half-life thus obtained with the measured ^{21}F half-life of 4.35 ± 0.04 sec (Fo 65) gives $(\underline{ft})^+/(\underline{ft})^- = 1.10 \pm 0.08$.

C. Results for ^{25}Si

Although the more complete delayed-proton results for ^{25}Si reported by Reeder, et al., (Re 66) are a considerable improvement over the early experiments (Ba 63, Mc 65, Ha 65a), it is still of interest to obtain high resolution delayed-proton spectra spanning a large energy range. Since the determination of absolute beta-decay strengths depends on measurements of all the significant particle decay branches of the T = 3/2 state (for which the superallowed β-decay strength can be calculated), such high resolution experiments might serve to reduce the errors on the ft values, and in turn, yield a more accurate ratio of $(ft)^+/(ft)^-$.

1. Discussion of data

The ^{24}Mg(^{3}He, 2n)^{25}Si experiments were done primarily at 29.5-MeV and 40-MeV bombarding energies on a natural Mg target. Although a 40-MeV ^{3}He beam is energetic enough to produce ^{21}Mg via the ^{24}Mg (^{3}He, 2nα) reaction (see Table 4-1), no proton peaks associated with its decay were seen. A experiment performed with a 60-MeV ^{3}He beam did, in fact, produce peaks identifiable with ^{21}Mg, notably those prominent peaks at 1.773 and 1.939 MeV (peaks 5 and 6 in the ^{21}Mg spectra shown in the previous Section). These peaks, along with the ^{25}Si peaks at 1.849 and 2.218 MeV, served to cross-check the accuracy of these energies as calibration points (as listed in Table 4-4).

a. Proton spectra. The ^{25}Si delayed-proton spectrum displayed in Fig. 4-9 was obtained using a 10-μm ΔE 250-μm E detector telescope. These data were taken at a ^{3}He beam energy of 40 MeV. The peak

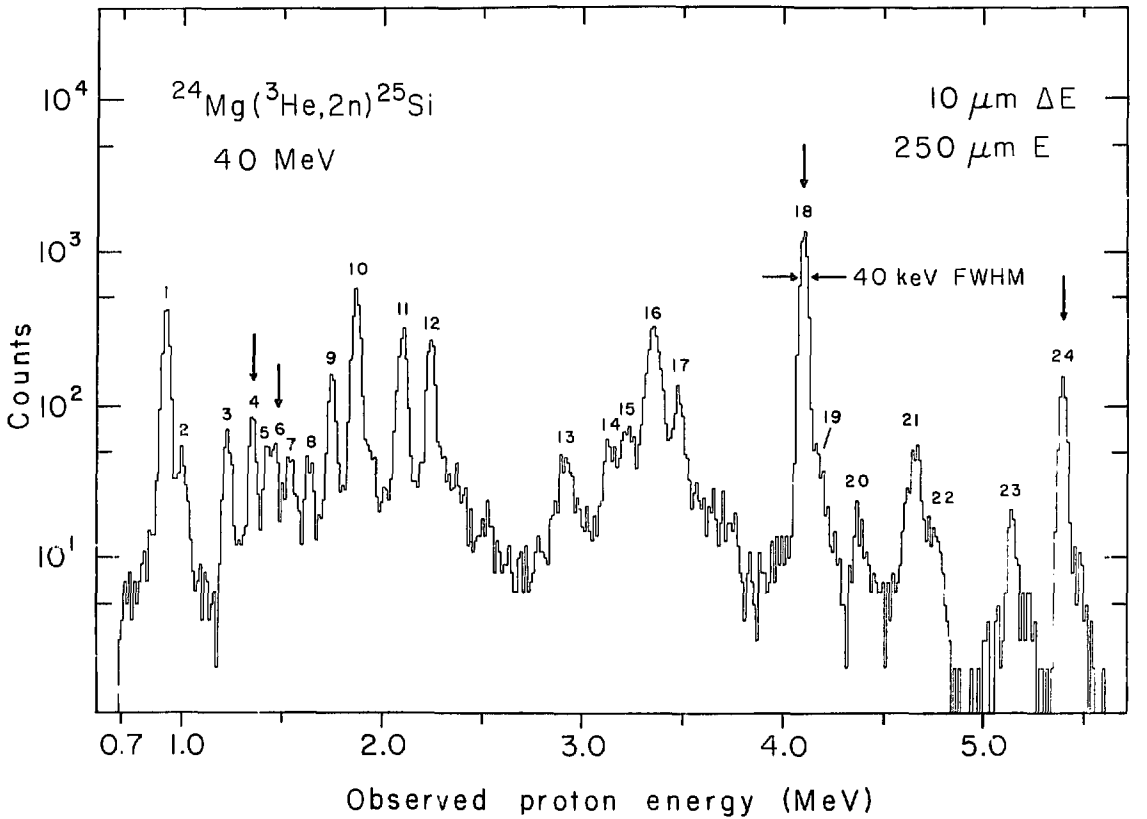

XBL 7311-6804

Fig. 4-9. Delayed protons from ^{25}Si. The numbers serve to identify peaks in Tables 4-10 and 4-11. The vertical arrows denote peaks arising from decay of the T = 3/2 state.

numbers are used to identify the peaks for use below in Tables 4-10 and 4-11. Additional data, not shown here, were acquired using both thinner (6-μm ΔE 50-μm E) and thicker (50-μm ΔE 500-μm E) detector telescopes. In the latter case, no additional higher energy proton groups (E_p > 5.5 MeV) were identified.

No known β^+-delayed protons could originate from any likely target contaminants. However, competing reactions from the ^{24}Mg + ^{3}He reaction can occur, in principle. The production of ^{21}Mg as one of these has already been discussed. The nuclide ^{24}Al, and its isomer $^{24}Al^m$ can both be produced from this reaction, though the 29.5-MeV bombarding energy is only a few MeV above their respective thresholds. Both have been identified as delayed alpha precursors (Ha 72), although either can positron decay to proton unbound levels in ^{24}Mg (To 71). However, all statistically significant peaks in the time-routed data were found to exhibit half-lives consistent with that of ^{25}Si, thereby eliminating ^{24}Al and $^{24}Al^m$ as sources of the intense proton peaks.

The energy calibration points used here are designated in Table 4-4. The resulting lab energy for each of the 24 proton peaks is listed in Table 4-10, including the relative intensity for each of these peaks. The energy resolution is ~40 keV FWHM, which is just sufficient to resolve peaks 40 keV apart, as in the case of peaks 5 and 6. In the spectrum shown in Fig. 4-9, there is a slight decrease in peak intensity for peaks with energies greater than ~4 MeV, due to a particle-identification-gate misadjustment. The intensities for these higher energy peaks are taken from data acquired with a 50-μm ΔE 500-μm E telescope. The errors on the relative intensities listed in Table 4-10

Table 4-10. Observed proton energies and intensities for the delayed-proton decay of ^{25}Si. The peak numbers correspond to the identification numbers shown in Fig. 4-9.

Peak Number	E_p (Lab) MeV ± keV	Relative[a] Intensity (%)
1	0.905 ± 2[b]	22.2 ± 1.4
2	0.992 ± 25	3.1 ± 0.6
3	1.213 ± 15	3.8 ± 0.6
4	1.335 ± 15	4.7 ± 0.6
5	1.405 ± 20	2.7 ± 0.4
6	1.445 ± 20	2.7 ± 0.4
7	1.522 ± 15	3.8 ± 0.6
8	1.616 ± 15	2.9 ± 0.4
9	1.728 ± 10	9.4 ± 0.8
10	1.849 ± 1[b]	33.3 ± 2.5
11	2.075 ± 10	20.3 ± 0.6
12	2.218 ± 1[b]	16.8 ± 1.0
13	2.895 ± 15	5.9 ± 0.5
14	3.108 ± 20	4.7 ± 0.6
15	3.198 ± 20	6.4 ± 0.6
16	3.333 ± 15	32.2 ± 1.6
17	3.461 ± 15	9.2 ± 0.6
18	4.091 ± 3[b]	100
19	4.172 ± 40	5.6 ± 0.8
20	4.372 ± 20	2.3 ± 0.4
21	4.651 ± 15	9.1 ± 1.0
22	4.768 ± 20	2.3 ± 0.6
23	5.151 ± 15	2.7 ± 0.6
24	5.404 ± 3[b]	21.7 ± 1.6

a) These are relative to the most intense group-peak 18.

b) Energy calibration point, see discussion in Sec. IV A.

include any uncertainties arising from this procedure, as well as any statistical effects.

b. Half-life measurements. All of the peaks have been identified with the decay of ^{25}Si (except at a 60-MeV bombarding energy, as noted above). Following the description in Sec. III C, the resulting half-life, averaged over five independent determinations, is 222.6 ± 5.9 msec. This agrees with the previous values obtained by McPherson, et al. (Mc 65)--225 ± 6 msec, and by Reeder, et al., (Re 66)--218 ± 4 msec. The resulting weighted average of these three values is 220.7 ± 2.9 msec and has been used for all subsequent calculations and results quoted here.

2. Analysis

a. Assignment of energy levels. The penetrability calculations displayed in Fig. 2-3 indicate that proton decay of excited states in ^{25}Al can proceed to several final states in ^{24}Mg with nearly equal probability, which can complicate identification of the origin of a peak. However, unlike ^{21}Na, many excited states above 5 MeV are known in ^{25}Al, making proton decay assignment somewhat easier. The accuracy of the energy calibration also aided in these assignments.

The ground state J^{π} for ^{25}Si is assumed to be 5/2+, analogous to that for the ^{25}Na ground state. The lowest T = 3/2 states in ^{25}Al and ^{25}Mg have also been assigned $J^{\pi} = 5/2+$, on the basis of their characteristic L transfers in two-nucleon transfer reactions (Ha 66). The measured γ-decay transitions from this analogue level in ^{25}Al substantiate the J^{π} assignment (Mo 68). Hence allowed β^{+} decay from the

analogue, ^{25}Si, will populate J^{π} = (3/2, 5/2, or 7/2)+ states in ^{25}Al.

The peak assignments are exhibited in Table 4-11, and the deduced energy levels in ^{25}Al are compared to previous determinations. States up to ~ 5 MeV have been the subject of intensive investigation; these are summarized in Refs. (Li 68, Ro 70, Br 73). It is unlikely that any new levels fed by allowed β decay exist in this energy region. Above 5 MeV, recent studies employing the ^{24}Mg(p, p) and (p, p' γ) reactions (Du 72), and the ^{24}Mg(^{3}He, d) and ^{28}Si(p, α) reactions (Br 73), have accurately located many new levels. No new levels have been postulated based on the present delayed proton results. In fact, the agreement between those excitation energies inferred from the present data, and the values obtained via reactions described above is excellent.

The two states populated by beta decay (as inferred from the decay protons), at E_x ~ 5.28 and 7.12 MeV, have previously been tentatively assigned J^{π} = 1/2+ in Ref. (Du 72). The lower of these is a broad state with Γ ~ 185 keV (Du 72) and could be a doublet, one component of which is fed by allowed beta-decay. The present proton data show a broad peak (peak 13 in Fig. 4-9) ~ 125 keV FWHM, which is consistent with the assignment to this level. The J^{π} = 1/2+ assignment to the higher 7 MeV state is less certain, and the present data indicate this assignment is incorrect (if these levels are, in fact, the same).

Although seven proton peaks occur with energies less than 1.6 MeV, only one of these arises from a transition to the ^{24}Mg ground state (peak 7). The others, as shown in Table 4-11, apparently are due to decays to excited states in ^{24}Mg from high-lying levels in ^{25}Al.

Table 4-11. Assignment of observed proton decays to states in ^{25}Al, and a comparison of the inferred excitation energies to previous results. Underlined numbers preceding each entry correspond to peak identification numbers shown in Fig. 4-9. (All entries given in MeV ± keV).

Center-of-Mass Proton Energies Corresponding to Decay to the Following Levels in ^{24}Mg:				Deduced[a] Levels in	Previous Excitation Energies			
g.s.	1.369 MeV	4.123 MeV	4.233 MeV	^{25}Al	En 67[b]	Br 73	E_x Other	Ref.
7 1.586 ± 15	--[c]			3.857 ± 15	3.86	3.856 ± 3	3.854 ± 0.6	Pi 72
							3.858 ± 4	Va 69[b]
							3.858	Li 68
10 1.927 ± 1[d]	--			4.197 ± 3[e]	4.20	e)	4.198	Li 68
12 2.311 ± 1[d]	1 0.943 ± 2[d]			4.582 ± 1[e]		e)	4.581	Li 68
X[c,f]	5 1.464 ± 20			5.104 ± 20	5.08	5.101 ± 10		
13 3.017 ± 15	X			5.288 ± 15	5.28		5.28 ± 10	Du 72
14 3.239 ± 20	X			5.510 ± 20		5.527 ± 7		
15 3.332 ± 20	X[g]			5.603 ± 20			5.58 ± 10	Du 72
X[g]	11 2.162 ± 10			5.802 ± 10	5.78	5.809 ± 7	5.79 ± 10	Du 72
21 4.846 ± 15	16 3.473 ± 15	X	--	7.115 ± 11	7.12	7.112 ± 10	7.12 ± 10	Du 72
22 4.968 ± 20	17 3.606 ± 15	X	X	7.243 ± 12	7.25 ± 30[h]	7.240 ± 7	7.24 ± 10	Du 72
X	X[f]	2 1.034 ± 25	X	7.428 ± 25		7.417 ± 7	7.42 ± 10	Du 72
23 5.367 ± 15	X[f]	3 1.264 ± 15	X	7.648 ± 11			7.647 ± 6	Te 69a[b]
24 5.631 ± 3[d]	18 4.263 ± 3[d]	6 1.506 ± 20	4 1.391 ± 15	7.902 ± 3[e]			e)	
X[i]	19 4.347 ± 40	X[g]	X	7.987 ± 40			7.972 ± 6	Te 69a[b]
							7.968 ± 5	Ma 68[b]
							7.975 ± 5	Bu 73a[a]
X[f]	20 4.556 ± 20	9 1.801 ± 10	8 1.684 ± 15	8.193 ± 8	8.20 ± 30[h]		8.194 ± 6	Te 69a[b]

continued . . .

Table 4-11 (continued)

a) These energies are calculated using a proton separation energy of 2.271 ± 0.001 MeV (see Table 4-2).

b) The original excitation energies given here have been corrected for the change in separation energy.

c) Energetically allowed proton decays that are below the experimental energy range (≤ 600 keV) are denoted by --, while those within the detectable energy range but unobserved in these experiments are denoted by X.

d) Part of the energy calibration, see Sec. IV A.

e) The excitation energies of these states, which are averages of previous results, are from Table 4-4.

f) Possible evidence for this decay branch exists in some spectra.

g) Potential decay peak obscured by more intense peaks in the energy region of interest.

h) From the delayed-proton results in (Re 66).

i) Weak evidence for this possible decay exists in some spectra (as a high-energy shoulder on peak 24).

Of these, only peak 2 has been assigned a level with no other observed decay branch. As mentioned above, it is unlikely that this peak is due to decay of a heretofore unobserved state below 5 MeV in ^{25}Al; thus it has been assigned to the 7.428-MeV state, previously identified in Refs. (Br 73, Du 72).

Peak 19 has been associated with the decay of an excited state at 7.987 MeV. Since this peak is seen as a low-intensity shoulder on peak 18 (possibly the ground-state decay of this state is a similar shoulder on peak 24), the energy is uncertain to 40 keV. However, it agrees well with the state at ~ 7.97 MeV, which has been identified as the T = 3/2 analogue to the first-excited states in ^{25}Si and ^{25}Na (Mo 68, Te 69a, Be 73a). Since β^+ decay to this level is <u>not</u> superallowed, the resulting proton intensity would be reduced considerably compared to the superallowed β^+ decay to the nearby ($\Delta E \sim 70$ keV) ^{25}Si ground-state analogue. The proton spectrum shown in Fig. 4-9 is consistent with this. States above 7.5 MeV are unbound to proton decay to the 5.228-MeV state in ^{24}Mg. Only decay from the 8.193-MeV state would yield protons above the 600-keV lower limit on the experimental energy range; no protons corresponding to this decay were observed.

With the exception of a state ~ 4.9 MeV tentatively assigned $J^\pi = 7/2+$ in Ref. (Li 68), all energetically observable decays from those known levels with $J^\pi = (3/2, 5/2, \text{ or } 7/2)+$ have been seen for states up to 5 MeV. No strong proton peak due to the decay of a ~ 4.9-MeV level is apparent in the present proton spectra.

b. <u>Decay of the (lowest) T = 3/2 state</u>. The four observed decay protons of the lowest T = 3/2 state are designated by vertical arrows in

Fig. 4-9 and are listed in Tables 4-11 and 4-12. Although the decays to the ground and first-excited states in ^{24}Mg were identified in the earlier work (Re 66), the lower intensity decays to the second and third-excited states were first observed in the present work. Table 4-12 gives the relative branching ratios for each of these decays, as well as the results of penetrability calculations for each decay. Although the proton decays are isospin forbidden, the competition from isospin allowed γ decay is nevertheless small--$\Gamma_\gamma/\Gamma \sim 2\%$. This ratio is calculated using $\Gamma_\gamma \sim 2$ eV (Mo 68) and Γ (total) ~ 100 eV (Te 69).

c. Comparison with previous delayed-proton results. The present results confirm many of the earlier measurements by Reeder et al. (Re 66), and differ in some assignments to proton unbound levels in the emitter, ^{25}Al. The higher resolution data discussed here resolve some of the broad proton peaks in the earlier data into two or more distinct peaks, and identify additional peaks in the decay spectrum.

The assignments listed in Table 4-11 indicate that no states between 5.9 and 7.0 MeV give rise to observable proton decay peaks. However, the previous Brookhaven work (Re 66) shows three levels in this range of excitation. The lowest of these, at 6.15 MeV, should emit protons with an energy of ~ 3.72 MeV. No evidence for a peak in this energy region appears in Fig. 4-9. The second level, at 6.70 MeV, is based on the observed peak ~ 2.9 MeV (lab) assigned as originating from decay to the first excited state in ^{24}Mg. However, this observed proton peak could be due to decay to the ^{24}Mg ground state of a state at 5.3 MeV in excitation. The present results prefer this assignment since the observed peak width is consistent with the known width of a

Table 4-12. Energetically Allowed Proton Decay of the Lowest T = 3/2 State in ^{25}Al.

Final State In ^{24}Mg (MeV)	J^{π} [a]	Center-of-Mass Decay Energy (MeV)	Observed Intensity [b] I(%)	Relative Branching Ratio (%)	Penetrability [c] P	I/P
0.000	0+	5.631	6.62 ± 0.49	16.8 ± 1.3	0.76	8.7
1.369	2+	4.262	30.51 ± 0.69	77.5 ± 2.2	1.30	23.5
4.123	4+	1.508	0.82 ± 0.12	2.1 ± 0.3	0.007	117
4.233	2+	1.398	1.43 ± 0.18	3.6 ± 0.5	0.11	13.0
5.228	3+	0.403	--		$\sim 4 \times 10^{-5}$	

a) Excitation energies and J^{π} for ^{24}Mg are taken from ref. (En 67).

b) These are fractional amounts of the total observed proton decay. The decay marked with -- is below the experimental energy range.

c) Calculated as discussed in Sec. II D, with r_0 = 1.3 fm.

level at 5.28 MeV (as noted in the discussion above). The level at 6.92 MeV was postulated on the basis of an observed peak ~ 3.2 MeV. The present results resolve this group into two peaks, both of which have been assigned to known states decaying to the ^{24}Mg ground state (see Table 4-11).

Finally, the peak at ~ 5.1 MeV was assigned to a state at 8.97 MeV, agreeing with the earlier proposal in (Ha 65a), and was thought to be the T = 3/2 analogue to the second-excited state in ^{25}Na. This state in ^{25}Na is now known to have $J^{\pi} = 1/2+$ (Be 69); beta decay to its mirror in ^{25}Al would not be an allowed transition and hence protons from this state would not be expected. The present assignment of this peak to a state at 7.65 MeV is shown in Table 4-11. It should be noted that this state appears to decay also to the second-excited state in ^{24}Mg.

d. Branching ratios and ft values. The estimate of $\langle \sigma \rangle^2_{S.A.} = 0.24$ from (Ha 65), used with Eq. 2-14, gives log ft = 3.26 for the super-allowed beta decay leading to the lowest T = 3/2 state. The assumption of isospin purity for this state is supported, in part, by the analysis of the proton capture resonance for the lowest T = 3/2 level. Based on the proton partial widths, the isospin impurity amplitude was estimated to be < 1% (Mo 68).

The beta-decay branching ratios derived from the ratio of proton decay intensities relative to the T = 3/2 state decay are shown in Table 4-13. The branching to levels below 3 MeV is calculated from the mirror ^{25}Na negatron decay (Al 71). The statistical rate function calculations were performed as described in Sec. II A, and the ft values and their corresponding logarithms are shown in the last two

Table 4-13. Branching Ratios and ft Values for the Positron Decay of ^{25}Si.

Energy Level[a] In ^{25}Al (MeV ± keV)	J^{π}[b]	Proportion of Proton Decays (%)	Branching Ratio[c] From ^{25}Si (%)	ft[c,d] (10^3 sec)	Log ft (s)
0.000	5/2+		20.7 ± 1.0[e]	213 ± 10	5.33 ± 0.02
0.945 ± 1	3/2+		22.1 ± 1.4[e]	133 ± 8	5.13 ± 0.03
1.613 ± 1	7/2+		16.9 ± 1.3[e]	128 ± 8	5.11 ± 0.03
1.790 ± 1	5/2+		1.7 ± 0.3[e]	1172 ±192	6.09 ± 0.07
2.673 ± 1	3/2+		< 0.4[e]	> 3300	> 6.5
2.721 ± 1	7/2+		6.7 ± 1.2[e]	187 ± 34	5.27 ± 0.08
3.859 ± 1	5/2+	1.16 ± 0.18	0.36± 0.06	1820 ±290	6.26 ± 0.07
4.197 ± 1	3/2+	10.16 ± 0.77	3.16± 0.26	169 ± 14	5.23 ± 0.04
4.582 ± 1	5/2+	11.90 ± 0.53	3.70± 0.20	112 ± 6	5.05 ± 0.02
5.102 ± 9	(5/2)+	0.82 ± 0.12	0.26± 0.04	1140 ±170	6.06 ± 0.07
5.282 ± 8		1.80 ± 0.12	0.57± 0.04[f]	448 ± 33	5.65 ± 0.03
5.525 ± 7		1.43 ± 0.18	0.45± 0.06	479 ± 63	5.68 ± 0.06
5.585 ± 9		1.95 ± 0.18	0.61± 0.06	336 ± 33	5.53 ± 0.04
5.803 ± 5		6.19 ± 0.37	1.93± 0.13	90 ± 6	4.95 ± 0.03
7.116 ± 6		12.60 ± 0.59	3.92± 0.22	13.7± 0.8	4.14 ± 0.02
7.241 ± 5		3.51 ± 0.25	1.09± 0.08	43.5± 3.3	4.64 ± 0.03
7.418 ± 6		0.95 ± 0.18	0.29± 0.06	134 ± 26	5.13 ± 0.09
7.647 ± 5		1.98 ± 0.24	0.62± 0.08	50 ± 6	4.70 ± 0.06
7.902 ± 3	5/2+, T=3/2	39.38 ± 0.92	12.51± 0.54	1.83	3.26

continued . . .

Table 4-13 (continued)

Energy Level [a] In ^{25}Al (MeV ± keV)	J^{π} [b]	Proportion of Proton Decays (%)	Branching Ratio [c] From ^{25}Si (%)	$\underline{ft}$ [c, d] (10^3 sec)	Log $\underline{ft}$ (sec)
7.972 ± 3	(3/2+, T=3/2)	1.71 ± 0.24	0.53 ± 0.08	39.5 ± 5.8	4.60 ± 0.06
8.194 ± 5		4.45 ± 0.31	1.39 ± 0.10	11.5 ± 0.9	4.06 ± 0.03

a) For states above 3 MeV, the values listed here are weighted averages of those energies with errors in Table 4-11. For levels below 3 MeV, the excitation energies are from (Pi 72).

b) The spins and parities for the T = 1/2 states are from refs. (Li 68, En 67), while J^{π} for the T = 3/2 states are taken from (Ha 66, Mo 68).

c) The branching ratios and $\underline{ft}$ values are calculated based on the assumption of isospin purity for the lowest T = 3/2 state, including the correction for the γ-decay branch, as noted in the text.

d) The $\underline{ft}$ values are calculated using the Q_{β} shown in Table 4-2 and $T_{1/2}$ = 220.7 ± 2.9 msec.

e) The branching ratios and $\underline{ft}$ values for states below 3 MeV are calculated from comparison to the mirror ^{25}Na decay (Al 71).

f) This branching ratio has been corrected for $\Gamma p_0/\Gamma$ = 0.979 (Du 72).

columns of Table 4-13. The decay scheme for ^{25}Si, shown in Fig. 4-10, also lists branching ratios and log ft values derived from the present work. The proton decays for the T = 1/2 states (as seen in Fig. 4-10) having more than one decay branch are listed in Table 4-14, along with reduced-width ratios for the different possible J^{π} assignments.

3. Discussion and conclusions

The branching ratios and ft values deduced from the present work differ in some respects from the earlier work (Re 66). The present results indicate that ~ 31% of the beta-decay strength goes to proton-unbound levels above 3 MeV, which then gives the partial half-life for beta decay to the six states below 3 MeV. This improved value for the the branching leads to a new evaluation of the ratio of $(ft)^{+}/(ft)^{-}$.

The mirrors in ^{25}Mg-^{25}Al have been assigned up to 5 MeV (Li 68) and the negatron decay rates in ^{25}Na have been measured for these six mirror levels (Al 71). The resulting ft values can then be used to calculate the expected partial half-life for positron decay to these mirror levels. Thus a comparison of the partial half-lives gives $(ft)^{+}/(ft)^{-} = 1.17 \pm 0.04$, consistent with the ratio determined by Alburger and Wilkinson (Al 71), but with somewhat reduced errors.

D. Results for ^{37}Ca, ^{41}Ti, and ^{40}Sc.

The previous studies of ^{37}Ca and ^{41}Ti (Ha 64, Re 64, Po 66) were complicated by background and insufficient particle resolution. In ^{37}Ca, the T = 3/2 state decay peak was not completely resolved from the proton decay of nearby T = 1/2 states. In addition, there could be significant β-decay branches resulting in low energy protons that were

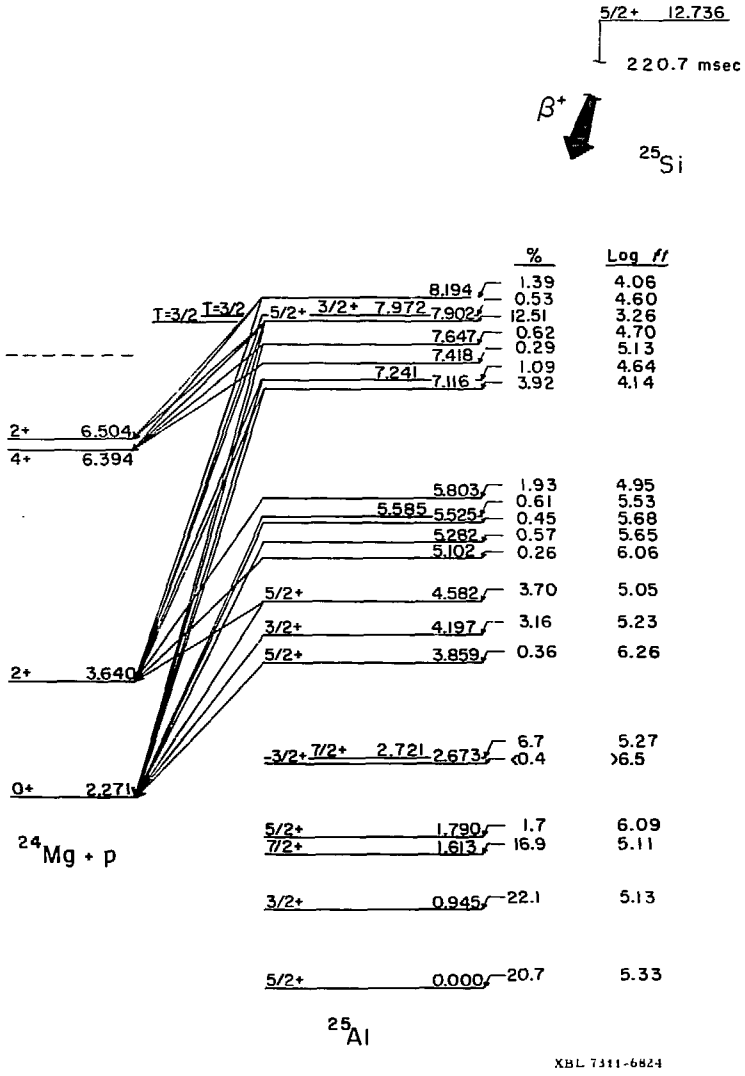

Fig. 4-10. Proposed decay scheme for ^{25}Si. The excitation energies for the unbound states are weighted averages of present and previous results. The branching ratios and ft values are from Table 4-13.

Table 4-14. Relative Branching Ratios and Reduced Widths for the Decay of T=1/2 States in ^{25}Al.

E_x in ^{25}Al (MeV)	Observed Ratio of Proton Intensities [a]		Ratio of Reduced Widths [b]			
			1x/g.s.		2x/g.s.	
	1x/g.s.	2x/g.s.	(3/2, 5/2)+	7/2+	(3/2, 5/2)+	7/2+
4.582	1.32		3.5			
7.115	3.54		1.9	0.26		
7.241	4.00		2.2	0.32		
7.647		1.41			480	0.56
	2x/1x	3x/1x	2x/1x		3x/1x	
8.194	4.09	1.26	360	7.6	8.6	33

a) The individual peak intensities are from Table 4-10.

b) The reduced widths are calculated by dividing the observed intensity by the penetrability for decay, assuming J^{π} = (3/2, 5/2, or 7/2)+, and r_0 = 1.3 fm.

unobserved in these experiments. Since the ground state J^{π} is 7/2- for ^{41}Sc and all excited states are unbound to protons (see Table 4-2), accurate intensity measurements of all significant proton decay peaks can result in direct determination of beta-decay branching ratios and absolute ft values. The degree of isospin purity of the lowest T = 3/2 state in ^{41}Sc can then be determined.

Higher accuracy data for the delayed proton decay of ^{40}Sc were also necessary, since proton peaks from this nuclide were present in all ^{40}Ca+^{3}He spectra discussed below. The bulk of the ^{37}Ca, ^{41}Ti and ^{40}Sc data were acquired simultaneously, and are therefore presented en masse in this section. The analysis and conclusions are described separately for each nuclide.

1. Discussion of data

The nuclides ^{37}Ca and ^{41}Ti were produced utilizing ^{3}He beams for bombardment of ^{36}Ar and ^{40}Ca targets. The ^{36}Ar + ^{3}He experiments were done at 40 MeV, while the ^{40}Ca + ^{3}He experiments were performed at 29.5, 36.5, and 60 MeV in order to establish relative peak intensities as a function of bombarding energy. In each case competing reactions can potentially complicate the proton spectra, as shown in Table 4-1. Half-life information and intensity as a function of bombarding energy are important aids in identification of the origin of individual peaks. Data were also acquired from the ^{40}Ca(p, n)^{40}Sc reaction at 20-MeV bombarding energy, in order to ascertain the contribution of delayed-protons from ^{40}Sc in the proton spectra obtained from ^{3}He bombardment of ^{40}Ca.

In the $^{40}Ca + {}^{3}He$ experiments, natural isotopic composition Ca targets of 1.0 to 1.5 mg/cm^2 thickness were used. For the $^{36}Ar(^{3}He, 2n)$ reaction, the gas target and gas handling system described in Sec. III B were used.

a. Peak identification, energies, and intensities. The known, weak, beta-delayed proton emitter ^{40}Sc (Ve 69) was present in all the ^{41}Ti spectra (see Table 4-1). Figure 4-11 shows low-energy proton spectra following ^{3}He and proton bombardment of ^{40}Ca; parts a) and b) were obtained at ^{3}He bombarding energies of 29.5 and 60 MeV respectively. The 6-μm ΔE 50-μm E telescope cutoff was ~ 2.2 MeV. The ^{40}Sc spectrum produced at a proton bombarding energy of 20 MeV is shown in Fig. 4-11 c) and was taken with a thicker E counter in order to investigate proton decay groups with higher energies. Those peaks arising from more than one source but not separated into clearly identifiable components (due to proton energy differences being less than or nearly equal to the ~ 40 keV energy resolution) are numbered as one peak.

A more complete spectrum from the 60-MeV ^{3}He bombardment of a ^{40}Ca target is shown in Fig. 4-12. The peak labeled (1) shows the location of peak 1 which has been partially reduced in intensity due to an electronic threshold effect. Finally, a delayed-proton spectrum from ^{37}Ca produced via ^{36}Ar (^{3}He, 2n) is shown in Fig. 4-13 for the energy region between 2 and 4 MeV. Beyond 4.2 MeV the spectrum is featureless, and no specific peaks could be identified. The fits to peaks 22, 23, and 24, shown in the inset of Fig. 4-13, were generated using the Gaussian peak fitting program described earlier in Sec. III E.

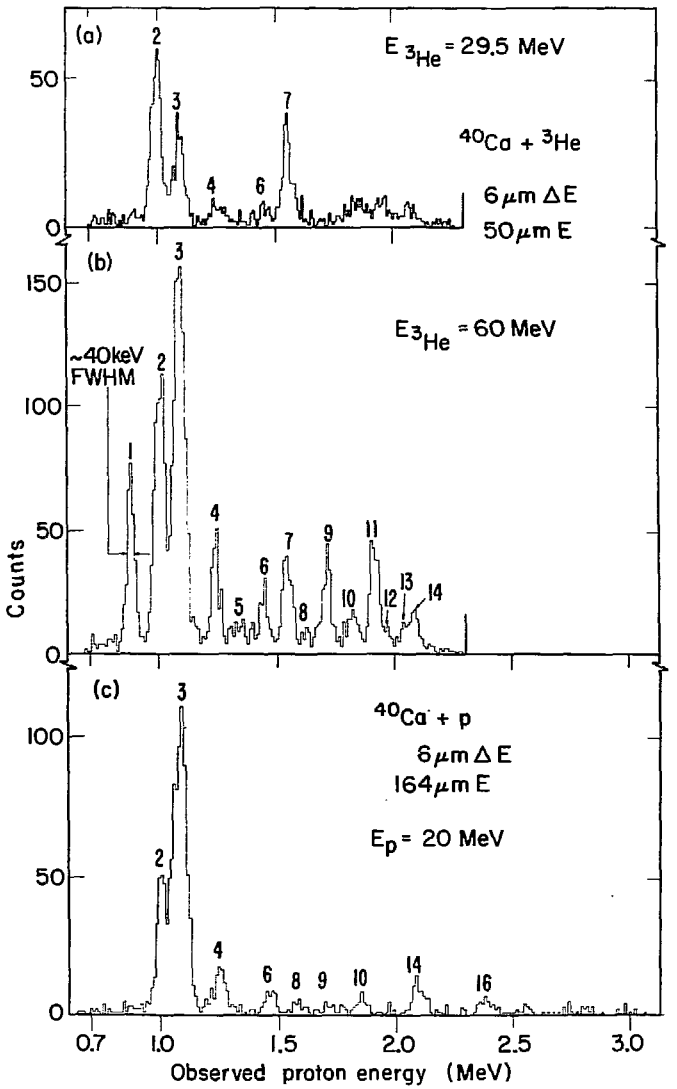

Fig. 4-11. Identified protons following ^3He or proton bombardment of ^{40}Ca. The peak identification numbers are discussed in the text.

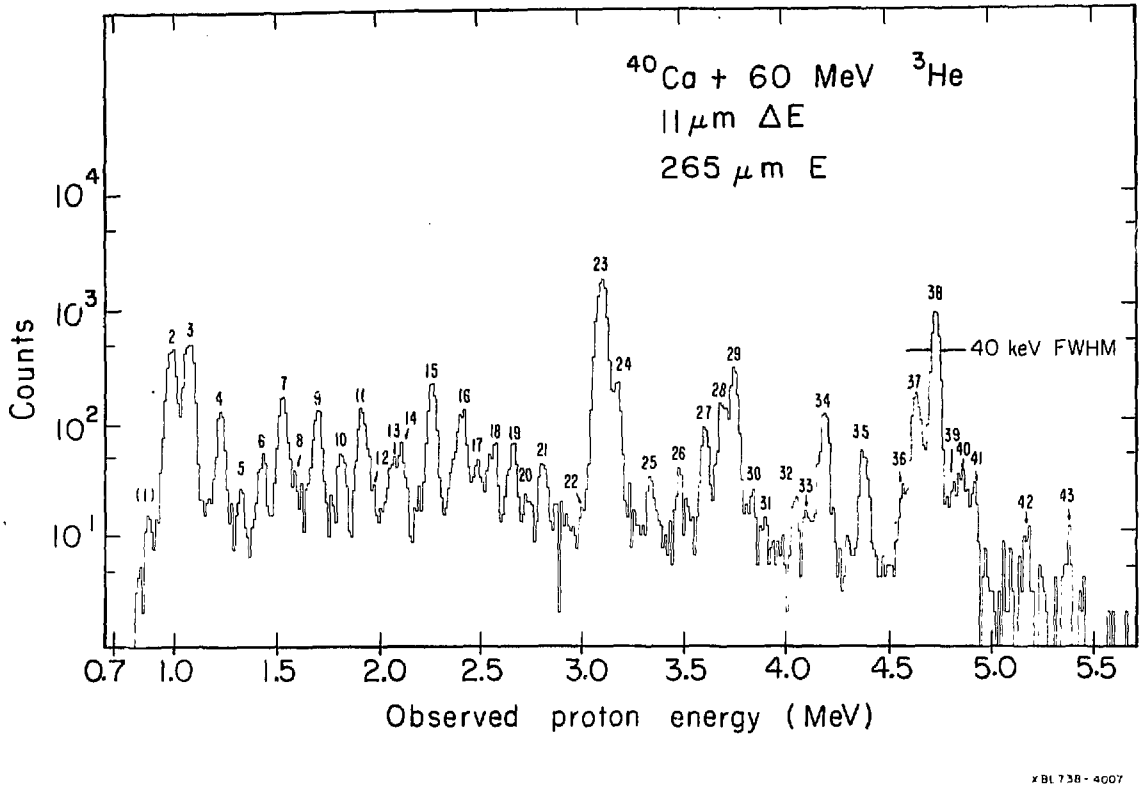

XBL 738-4007

Fig. 4-12. Delayed protons following ^{40}Ca + ^{3}He bombardment at $E_{^{3}He}$ = 60 MeV. The numbering system is identical to that in Fig. 4-11 and is described in the text. The intensity of peak (1) is reduced due to an electronic cut-off effect.

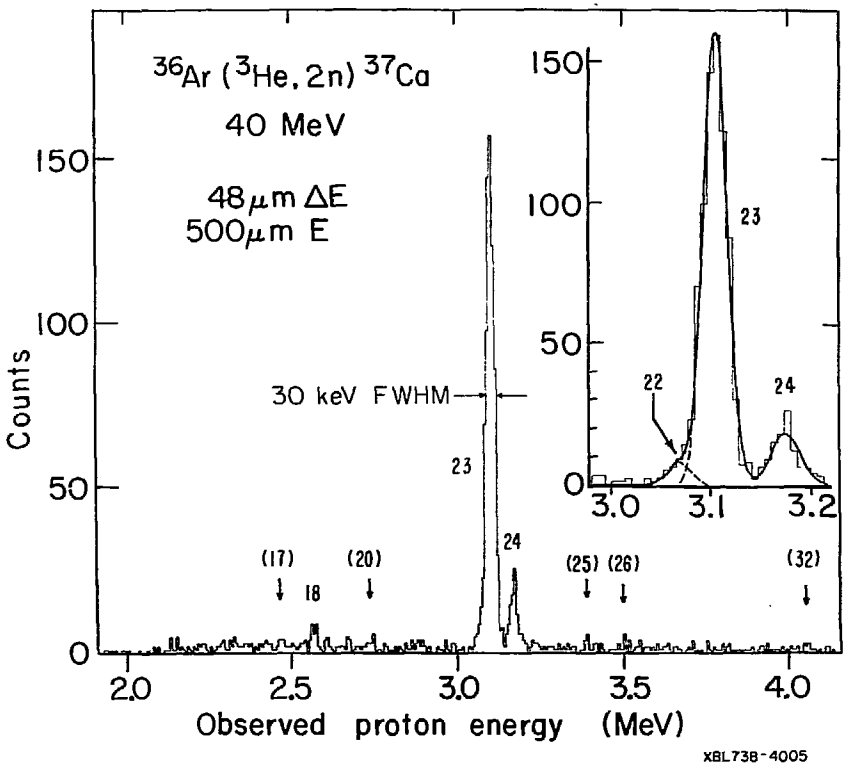

Fig. 4-13. Delayed protons from ^{37}Ca. The peak numbering corresponds to that in Figs. 4-11 and 4-12 (see text). Numbers in parentheses show locations of proton peaks whose energies were determined from other data. The inset shows in more detail the three main proton groups with energies greater than 3 MeV. The smooth curve and the dashed lines are Gaussian fits to these peaks.

Three types of data were used in identifying the origin of individual proton peaks: half-lives, energies and intensities from single-component spectra, and relative excitation functions. As noted in Sec. III C, half-life information was available for each statistically significant peak from the sequentially-routed 8×512-channel data; the relatively short ^{41}Ti half-life aids in distinguishing most of the peaks originating from this precursor.

(i) ^{40}Ca + p. The p + ^{40}Ca reaction at 20 MeV produces only ^{40}Sc. These data were used to identify major ^{40}Sc peaks with higher resolution than available in the previous measurements (Ve 69). The resulting energies and intensities could then be applied to the interpretation of the ^{40}Ca + ^{3}He results.

(ii) ^{36}Ar + ^{3}He. As can be seen from Table 4-1, the ^{3}He + ^{36}Ar reaction at 40 MeV has several competing exit channels capable of producing delayed protons. The nuclide ^{36}K can, in principle, β^+ decay to proton unbound levels in ^{36}Ar. However, from beta-decay systematics such decays should be extremely weak; ^{36}K has been discounted as a source of delayed protons produced in reactions on this target.

Three other possibilities exist. Two of these--^{32}Cl and ^{29}S--can be eliminated as possible sources for peaks 18, 22, 23, or 24 in in Fig. 4-13 since the energies of the main decay groups are known (Ha 72) and do not correspond to these peaks. (In ^{32}Cl, only electron capture could lead to protons with energies greater than 2.8 MeV.) The third possibility, ^{33}Ar, does have a main decay peak essentially of equal energy with peak 24 (Ha 71). However a) other known proton

groups from ^{33}Ar do not appear in the spectrum, and b) ^{32}S targets (as Cu_2S) were bombarded with 29.5-MeV ^{3}He beams and no proton activity that could be associated with ^{33}Ar was observed. This latter is consistent with other evidence (Ma 70a) that inert gas nuclides have extremely low collection efficiencies in He-jet systems without cooled collector foils. These results eliminate ^{33}Ar as a source of background in this spectrum.

(iii) $^{40}Ca + ^{3}He$. Data from $^{40}Ca + ^{3}He$ were acquired at three bombarding energies and with several different ΔE-E detector telescopes. These data establish relative excitation functions for most of the peaks shown in Fig. 4-12; this spectrum contains contributions from ^{40}Sc, ^{37}Ca, and ^{41}Ti. However, ^{36}K can be eliminated as a source of protons as in the previous discussion; in fact, no prominent peak exhibiting a lifetime as long as that of ^{36}K was observed (see Table 4-1). The preceding discussion on ^{33}Ar eliminates it from consideration as a background source. Likewise the relative excitation functions coupled with the known ^{32}Cl proton energies serve to eliminate it as a possible proton source.

Finally, in addition to products from competing reaction channels, target contaminants comprise another potential source of delayed protons. The two most likely contaminants are oxygen (from CaO) and Mg, which was present at ~0.2% by weight of the natural Ca target material. These lead to ^{17}Ne and ^{25}Si, via the $^{16}O(^{3}He, 2n)$ and $^{24}Mg(^{3}He, 2n)$ reactions respectively. No identifiable ^{17}Ne peaks or components were found; as discussed in the case of ^{33}Ar, inert gases do not adhere to the (uncooled) collector. On the other hand proton

peaks from ^{25}Si were found; their intensities are consistent with the approximate level of Mg contamination in the Ca targets.

The results of these analyses are shown in Table 4-15, where laboratory proton energies and relative intensities for one or more components are indicated for each of the 43 numbered peaks. Where more than one laboratory energy is indicated for an individual peak, the energy was determined independently for each constituent from one-component data. The energy calibrants used for the various reactions and the relevant proton energy ranges are tabulated in Table 4-4. In addition, part of the ^{41}Ti data acquired with the 6-μm ΔE 50-μm E telescope required the use of secondary calibration points at 1.085 MeV (^{40}Sc) and 1.542 MeV (^{41}Ti), their energies having first been determined (in part) from the primary calibrants in Table 4-4. The relative intensities for each nuclide were computed separately, correcting where necessary for "contaminant" contributions. It should be noted that peaks 43 and 33 have been assigned to ^{25}Si and arise from the decay of the lowest T = 3/2 state to the ^{24}Mg ground- and first-excited states respectively (see Sec. IV C).

The present ^{36}Ar(^{3}He, 2n) data reliably give relative intensities down to ~ 4% while ^{37}Ca peaks in the ^{40}Ca + ^{3}He data are similarly identifiable to ~ 2.5% for $E_p < 3$ MeV, and to ~ 1% for $E_p > 3$ MeV. The results for ^{41}Ti cover all significant proton decays in the energy range from 0.6 to 8.5 MeV, and with relative intensities down to ~ 3% for $E_p < 3$ MeV and down to 1.5% for $E_p > 3$ MeV.

b. Half-lives. The previously established half-lives of ^{40}Sc and ^{37}Ca are shown in Table 4-1. The present measurements of the ^{40}Sc

Table 4-15. Observed proton energies and relative intensities for the delayed-proton precursors ^{41}Ti, ^{40}Sc, and ^{37}Ca. The peak numbers correspond to peak identification numbers shown in Figs. 4-11, 4-12, and 4-13.

Peak Number	E_p (Lab)[a] MeV ± keV	Relative Intensities[b] ^{41}Ti	^{40}Sc	^{37}Ca
1	0.870 ± 15			13.8 ± 1.5
2	1.000 ± 15[c]	38.6 ± 2.4[d]	27.3 ± 3.0[e]	
3	1.085 ± 10		100.	
4	1.248 ± 15[c]	3.9 ± 0.9[d]	14.5 ± 1.8[e]	
5	1.339 ± 25		4.4 ± 1.0[f]	
6	1.454 ± 15		8.9 ± 1.5	
7	1.546 ± 15	21.6 ± 0.7		
8	1.612 ± 25		4.7 ± 0.6	
9	1.709 ± 10[c]		2.6 ± 0.7[e]	8.7 ± 0.8[d]
10	1.846 ± 20		9.4 ± 1.0	
11	1.925 ± 10			9.7 ± 0.6
12	1.983 ± 25	3.1 ± 0.6		
13	2.063 ± 30	4.1 ± 0.5		
14	2.113 ± 25		9.0 ± 1.0	
15	2.271 ± 10	26.1 ± 0.9		
16	2.409 ± 20	14.7 ± 0.3[d]		
	2.443 ± 25[e]		5.4 ± 0.9[e]	
17	2.498 ± 20			2.5 ± 0.3
18	2.580 ± 20[g]			4.5 ± 0.4[g]
19	2.662 ± 20	8.1 ± 0.8		
20	2.745 ± 20			2.5 ± 1.0
21	2.814 ± 15	4.9 ± [illegible]		
22	3.063 ± 15[h]			4.0 ± 1.2[h]
23	3.103 ± [illegible][i]			100.
	3.077 ± 15[j]	60.3 ± 3.8[i]		
24	3.173 ± 10[g]			12.8 ± 1.0[g]
	3.148 ± 20[j]	4.0 ± 1.1[i]		

continued . . .

Table 4-15 (continued)

Peak Number	E_p (Lab)[a] MeV ± keV	Relative Intensities[b] ^{41}Ti	^{40}Sc	^{37}Ca
25	3.339 ± 30	2.3 ± 0.4[k]		1.7 ± 0.4[h]
26	3.487 ± 20	2.8 ± 0.4[k]		1.1 ± 0.4[h]
27	3.605 ± 15	9.7 ± 0.4		
28	3.690 ± 15	15.5 ± 0.8		
29	3.749 ± 10	31.0 ± 2.0		
30	3.836 ± 25	2.4 ± 0.2		
31	3.904 ± 25	1.5 ± 0.2		
32	4.046 ± 20			1.4 ± 0.2
33	4.094 ± 25		—^{25}Si—	
34	4.187 ± 15	15.4 ± 0.5		
35	4.379 ± 15	7.2 ± 0.4		
36	4.564 ± 20	2.2 ± 0.3		
37	4.638 ± 10	22.1 ± 0.7		
38	4.734 ± 4[i]	100.		
39	4.832 ± 25	3.0 ± 0.3		
40	4.876 ± 20	3.4 ± 0.4		
41	4.925 ± 20	2.9 ± 0.3		
42	5.177 ± 30	1.5 ± 0.3		
43	5.387 ± 30		—^{25}Si—	

a) Unless otherwise noted, the observed energies are average values from the $^{40}Ca + {}^{3}He$ data.

b) These values are computed separately for each nuclide with 100 assigned the strongest branch. Unless otherwise indicated, they are from the $^{40}Ca + {}^{3}He$ data.

c) Average of values determined from $^{40}Ca + {}^{3}He$ and $^{40}Ca + p$ data.

d) Computed after removal of the ^{40}Sc component.

e) From $^{40}Ca + p$ data only.

continued . . .

Table 4-15 (continued)

f) This peak is tentatively assigned to ^{40}Sc on the basis of the relative excitation data.

g) Average of values from $^{40}Ca + ^{3}He$ and $^{36}Ar + ^{3}He$ data.

h) From $^{36}Ar + ^{3}He$ data.

i) Energy calibration point, see Sec. IV A.

j) From $^{40}Ca + ^{3}He$ at 29.5 MeV only.

k) Computed after removal of ^{37}Ca component.

and ^{37}Ca half-lives are consistent with these previous measurements, however neither, when weighted with the accepted values, makes a statistically significant change. These earlier values have therefore been adopted and have been used for all subsequent calculations presented here. The present results for the ^{41}Ti half-life are not, however, consistent with the former value. The present number of 80 ± 2 msec results from separate measurements from selected peaks at several bombarding energies. These peaks are all associated with ^{41}Ti decay only; at 29.5 MeV peaks 7, 23, and 38 were used, while at the higher bombarding energies of 36.5 and 60 MeV, peaks 7, 15, 29, and 38 were used.

The earlier Brookhaven data on ^{41}Ti (Po 66, Re 64) were taken at ~ 32 MeV bombarding energy, at which, according to Table 4-1, some contributions from the decay of ^{37}Ca could appear in the spectrum. Although the present data acquired at 29.5-MeV bombarding energy are above the ^{37}Ca threshold, no evidence for this nuclide exists in the proton spectrum (and none was expected, since a $\leq$ 2-MeV α particle has an extremely small probability of emission from the compound nucleus). On the other hand, peak 23 in the $E_{^3He}$ = 36.5-MeV results is ~ 33% due to ^{37}Ca; so at 32 MeV a ^{37}Ca contamination of 10-15% is possible. Since this group amounts to ~ 30% of the proton peak intensities previously used to evaluate the half-life, this level of impurity could be enough to lengthen the apparent half-life to ~ 88 msec. One should also note that the present data have a peak-to-valley ratio approximately three times better than that of the earlier results; this should serve also to reduce the small background contributions from ^{40}Sc (Ve 69)

at the higher proton energies. The present result for the ^{41}Ti half-life has been used for all subsequent calculations in this work.

2. Analysis

The spin-parity assignments for the precursors ^{41}Ti and ^{37}Ca follow from their $T_z = +3/2$ mirrors and from the J^π of the lowest $T = 3/2$ states in the $T_z = \pm 1/2$ nuclei. For mass 41, J^π for ^{41}K(g.s.) is 3/2+ (En 67), while the lowest $T = 3/2$ state in ^{41}Ca has been identified as 3/2+ by Belote, et al. (Be 67) and Lynen, et al. (Ly 67). Trainor et al. (Tr 73) have assigned $J^\pi = 3/2+$ for the lowest $T = 3/2$ level in ^{41}Sc. In the case of mass 37, the ground state J^π for ^{37}Cl is known to be 3/2+ (En 67), while Butler et al. (Bu 68) have assigned $J^\pi = 3/2+$ to the lowest $T = 3/2$ states in ^{37}K and ^{37}Ar.

Unlike some of the other $T_z = -1/2$ nuclei in the $A = 4n+1$ series where high resolution delayed-proton studies have resulted in some new spectroscopic assignments (^{17}F, ^{33}Cl (Ha 71) and ^{21}Na (Sec. IV B)), the energy levels in ^{41}Sc and ^{37}K have been extensively studied to approximately 7 MeV in excitation in each case, with spins and parities assigned for many levels. Hence, in the present case only one new level (in ^{41}Sc) has been identified, while in ^{40}Ca, several new levels are postulated as a result of the present ^{40}Sc data.

a. ^{40}Sc. The nuclide ^{40}Sc($J^\pi = 4^-$) is a very weak delayed proton emitter, with less than 1% of the total ^{40}Sc β^+ decay proceeding to particle-unbound levels in ^{40}Ca (Ve 69). The relative intensities for the major proton peaks arising from the decay of these levels are shown in Table 4-15; relative intensities of less than ~ 2.5% would not have been

reliably measured for proton energies less than 3 MeV, nor relative intensities of less than ~ 1.5% for protons greater than 3 MeV. Peak 5 has been tentatively assigned to ^{40}Sc decay. The relative excitation data from ^{40}Ca + ^{3}He are consistent with this assignment, even though it appears only very weakly in the ^{40}Ca + p data in Fig. 4-11.

The ^{40}Sc peak energies, corrected to the center-of-mass, are shown in Table 4-16 with a comparison to the previous measurements of Verrall and Bell (Ve 69). Their data extend to higher proton energies than the present results, and they identify peaks whose relative intensities extend as low as ~ 0.1%. The higher resolution results presented here show only one major change; the strongest proton peak, previously ~ 1.05 MeV and thought to be composed of decays from two or more closely grouped levels, has been resolved into two components (peaks labeled 2 and 3). It is possible that peak 3 still contains more than one component.

Also shown in Table 4-16 are the excitation energies in ^{40}Ca deduced on the assumption that the protons arise solely from decay to the ^{39}K ground state. These energies can be compared to known states in ^{40}Ca measured in ^{39}K(p, γ) experiments (En 67, De 70). These results do not correspond entirely with the previous measurements, possibly because allowed beta decay from ^{40}Sc proceeds to states with $J^{\pi} = 3^{-}$, 4^{-}, or 5^{-}, while proton capture reactions require $\ell = 3$ protons to populate $J^{\pi} = 4^{-}$ or 5^{-} levels in ^{40}Ca. No $\ell = 3$ proton results for ^{39}K(p, γ) have been reported.

Finally log ft values have been calculated for these decays assuming log ft = 5.0 for beta decay to the 9.45-MeV level--seen in the

Table 4-16 Energy Levels, Branching Ratios, and Log ft Values for ^{40}Sc Delayed-Proton Decay. (Energies in MeV ± keV).

Peak Number	Proton Energy (c.m.) (Ve 69)	Proton Energy (c.m.) Present	Deduced[a] E_x in ^{40}Ca	Known Levels in ^{40}Ca	J^π	Note	Present Results: Log ft[b]
2	1.08 ± 30	1.032 ± 15	9.362 ± 15	9.364 ± 1		c)	5.61
3		1.112 ± 10	9.442 ± 10	9.454 ± 1	$(2,3)^-$	c, d)	5.00
4	1.27 ± 30	1.279 ± 15	9.609 ± 15	9.603 ± 1	3^-	c, d)	5.76
5		1.373 ± 25	9.703 ± 25	9.669 ± 1	$(0,1,2,3)^-$	c, d)	6.22
6	1.48 ± 30	1.491 ± 15	9.821 ± 15	9.812 ± 1 9.830 ± 1		c)	5.85
8	1.58 ± 40	1.653 ± 25	9.983 ± 25				6.04
9	1.72 ± 30	1.752 ± 10	10.082 ± 10				6.23
10	1.88 ± 30	1.893 ± 20	10.223 ± 20	10.236 ± 2		c)	5.59
14	2.15 ± 30	2.166 ± 25	10.496 ± 25	10.531 ± 2		c)	5.43
16	2.44 ± 30	2.505 ± 25	10.835 ± 25				5.40

a) These are computed using the measured proton energies and $E_{sep.}$ = 8.330 ± 0.001 MeV (Table 4-2).

b) The ft values are computed using the known excitation energies for the first three levels listed, and the deduced values for excited states > 9.65 MeV. The Q_β value is from (Table 4-2), and the branching ratios are calculated assuming log ft = 5.0 (Go 66) for the strongest transition (peak 3).

c) These are from ref. (En 67), corrected for the newer value of the separation energy.

d) These are from ref. (De 70), weighted with those from (En 67).

present data as the largest intensity proton group. This assumption is based on the average allowed transition in the A =20 to 69 mass region, as shown in (Go 66). The sum of the β^+-decay branches leading to the ten proton groups observed in this work is ~ 0.2%, following the above assumption. Even in the case of a faster transition for this decay e.g., log ft ~ 4.5, the total observed branching ratio leading to proton unstable states in ^{40}Ca is ≤ 1%.

b. ^{37}Ca. There are two major differences in the otherwise general agreement with the previous results for ^{37}Ca (Po 66): proton decay has been seen from the lowest unbound level capable of being fed by allowed beta decay (peak 1 in Fig. 4-11 b) and the decay peak at ~ 3.1 MeV arising in part from the T = 3/2 state has been resolved into three components. Energy levels in ^{37}K fed by allowed β^+ decay are shown in Table 4-17, along with a comparison to known levels (Go 67, Th 70). Although other levels with J^π = (1/2, 3/2, or 5/2)+ are known in this energy region, possible proton peaks arising from their decay were too weak to have been reliably identified in the present spectra. These assignments also assume that the primary decay mode is to the ^{36}Ar ground state. This assumption essentially agrees with the previous results, although two levels, one at 5.05 MeV (the T = 3/2 state) and at 5.32 MeV are known to have $\Gamma_p/\Gamma < 1$ (Go 67, Th 70). In the case of the T = 3/2 state, $\Gamma_\gamma/\Gamma \sim 1.4\times10^{-3}$, and $\Gamma_{p_1}/\Gamma \sim 1.1\times10^{-2}$; qualitative evidence can be seen in some spectra for this very weak proton decay to the first excited state in ^{36}Ar (as a low energy shoulder on peak 4, Figs. 4-11 b and 4-12), but it is not of sufficient intensity to be reliable identified. For decay of the 5.32-MeV state to the first-excited state in ^{36}Ar, the

Table 4-17 Energies of Unbound Levels in ^{37}K Fed by Allowed Beta Decay from ^{37}Ca, and a Comparison with Previous Results. (Energies are in MeV ± keV).

Peak Number	Deduced E_x [a] in ^{37}K	Previous Work: Ref. Go 67		Previous Work: Ref. Th 70		Γ_{p0}/Γ [b]
1	2.751 ± 15	2.750 ± 1	5/2+			
9	3.614 ± 10	3.623 ± 15	(1/2, 3/2, 5/2)+			
11	3.836 ± 10	3.844 ± 10	(1/2, 3/2, 5/2)+			
17	4.425 ± 20	4.417 ± 5 4.435 ± 5	(1/2, 3/2, 5/2)+ or (1/2, 3/2, 5/2)+			
18	4.509 ± 20	4.523 ± 20	1/2+	4.496 ± 10	1/2+	
20	4.679 ± 20	4.659 ± 10	(1/2, 3/2, 5/2)+	4.671 ± 15	(1/2, 3/2, 5/2)+	
22	5.006 ± 15	5.018 ± 3	(3/2, 5/2)+	5.018 ± 10		
23	5.047 ± 3 [c]	5.048 ± 3	(3/2, 5/2)+, T=3/2	5.048 ± 15		0.988 ± 0.007
24	5.119 ± 10	5.116 ± 5	1/2+	5.116 ± 10		
25	5.289 ± 30	5.318 ± 6	3/2	5.321 ± 10	3/2+	0.75 ± 0.08
26	5.442 ± 20	5.449 ± 6		5.452 ± 10	1/2+	
32	6.016 ± 20	6.012 ± 20	(1/2, 3/2, 5/2)+	6.017 ± 10	(3/2, 5/2)+	

a) All peaks were presumed to arise from decay to the ^{36}Ar g.s. The excitation energies were computed using a proton separation energy of 1.857 ± 0.001 MeV (see Table 4-2).

b) This ratio is based on partial widths given in refs. Go 67, and Th 70.

c) This number is already averaged (see Table 4-3) and as noted in Sec. IV A was used, in part, as an energy calibrant (see Table 4-4).

proton energy is ~ 1.5 MeV, while the relative intensity is ~ 0.6 (from $\Gamma_{p_1}/\Gamma \sim 0.25$). This is too weak to have been observed here. The last column in Table 4-17 gives Γ_{p_0}/Γ for these two states.

Several calculations for $\langle\sigma\rangle^2$ have been made for the superallowed beta decay to the T = 3/2 analogue level (Ha 65, Ba 64, La 72, En 66). All give consistent values for $\langle\sigma\rangle^2$ which, when used in Eq. (2-14), result in log ft = 3.27 to 3.30 for the superallowed decay to the T = 3/2 analogue state (assuming $a^2 = 1$ in Eq. (2-20)).

If one assumes a log ft value of 3.30 for this nearly model-independent prediction for the superallowed beta-decay transition strength, the relative proton intensities can then be used to determine absolute ft values for positron decay to unbound levels in ^{37}K. These results and the absolute positron decay branching ratios that follow are shown in Table 4-18. The branching ratios and ft values for beta decay to the 5.05- and 5.32-MeV states have been corrected for the Γ_p/Γ ratio shown in Table 4-17.

Table 4-18 also shows the branching ratio and ft value for decay to the ^{37}K ground state, for which the log ft has been obtained from the mirror ^{37}Ar electron capture decay. By combining this branching ratio with the present results, the branching to the 1.368-MeV, $J^\pi = 1/2+$ state can be estimated. The decay scheme for beta-delayed protons from ^{37}Ca is shown in Fig. 4-14; the branching ratios and ft values to proton unbound levels are from the present work.

c. ^{41}Ti. The ground state of ^{41}Sc has $J^\pi = 7/2-$; hence beta decay to this state from ^{41}Ti ($J^\pi = 3/2+$) is first-forbidden unique and will be strongly hindered. (The analogous mirror ^{41}Ca → ^{41}K electron

Table 4-18. Branching Ratios, and $\underline{ft}$ Values for ^{37}Ca Positron Decay.

Energy In ^{37}K [a] (MeV ± keV)	J^{π} [b]	Proportion of Proton Decays (%)	Branching From ^{37}Ca [c] (%)	$\underline{ft}$ [c,d] (10^3 sec)	Log $\underline{ft}$ (sec)
0.000	3/2+ [e]		15.62 ± 0.52 [f]	125 ± 3 [f]	5.10 ± 0.01
1.368 [e]	1/2+ [e]		8.4 ± 2.5 [g]	121 ± 36	5.08 ± 0.13
2.750 ± 1	5/2+	8.48 ± 0.94	6.37 ± 0.73	74.0 ± 8.3	4.87 ± 0.05
3.617 ± 8		5.35 ± 0.50	4.02 ± 0.39	67.7 ± 6.5	4.83 ± 0.04
3.840 ± 7		5.96 ± 0.40	4.48 ± 0.32	52.1 ± 3.6	4.72 ± 0.03
4.417 ± 5 [h]		1.54 ± 0.19	1.15 ± 0.14	133 ± 16	5.12 ± 0.05
4.503 ± 8	1/2+	2.77 ± 0.25	2.08 ± 0.20	69.3 ± 6.5	4.84 ± 0.04
4.665 ± 8		1.54 ± 0.62	1.15 ± 0.46	110 ± 44	5.04 ± 0.18
5.018 ± 3	(3/2, 5/2)+	2.46 ± 0.74	1.85 ± 0.56	52 ± 16	4.71 ± 0.14
5.047 ± 3	3/2+, T=3/2	61.46 ± 2.27	46.74	2.0	3.30
5.117 ± 4	1/2+	7.87 ± 0.64	5.91 ± 0.50	14.9 ± 1.2	4.17 ± 0.04
5.318 ± 5	3/2+	1.04 ± 0.25	1.05 ± 0.27 [i]	71 ± 18	4.85 ± 0.12
5.449 ± 5	1/2+	0.68 ± 0.25	0.51 ± 0.19	130 ± 47	5.11 ± 0.17
6.016 ± 8	(3/2, 5/2)+	0.86 ± 0.12	0.65 ± 0.09	59.5 ± 8.7	4.77 ± 0.06

a) This is a weighted average of present and previous results shown in Table 4-17.

b) Spins and parities are from those shown in Table 4-17 and the present results.

c) The branching ratios and $\underline{ft}$ values are calculated based on the assumption of isospin purity for the lowest T=3/2 state, correcting for Γ_{p_0}/Γ.

continued . . .

Table 4-18 (continued)

d) The ft values are calculated using the Q_{β} shown in Table 4-2 and a half-life of 175 ± 3 msec.

e) Ref. (Go 67).

f) This is taken from the mirror decay, using $Q_{E.C.}$ and $T_{1/2}$ from (En 67) and $f_{E.C.}$ from (Go 71a).

g) The branching ratio is calculated from the sum of all measured branching ratios and that inferred for the ground state branch.

h) The lower of the two energies listed in Table 4-17 has been tentatively used, since no evidence for the upper level was observed in ref. (Th 70).

i) Corrected for Γ_{p_0}/Γ given in Table 4-17.

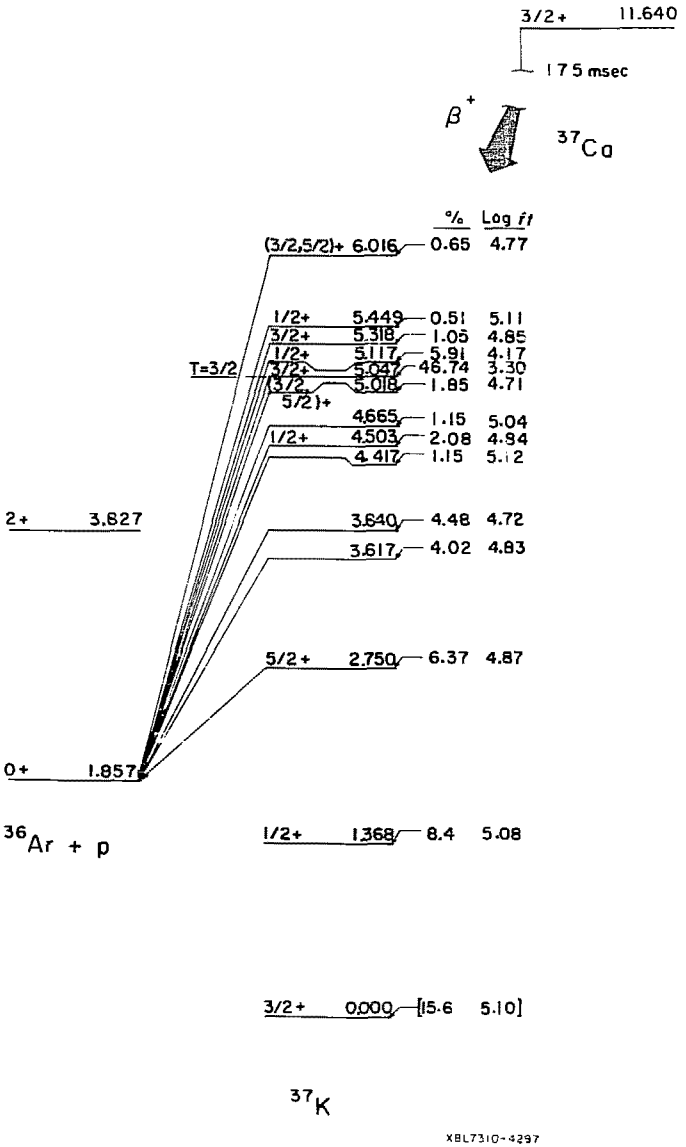

Fig. 4-14. Proposed decay scheme for ^{37}Ca. The excitation energies are weighted averages of present and previous results. The branching ratios and log ft values for decay to the excited states are from the present work, while the ground-state log ft is taken from the mirror decay.

capture decay has log ft = 10.5.) The first level to which allowed β^+ decay can proceed is at $E_x \sim 2.0$ MeV, well above the proton separation energy. It is therefore possible to directly determine the absolute beta-decay branching ratios from the relative intensities of the proton decays of these unbound levels, providing all significant proton intensities are measured. The observed proton groups range in energy from ~ 1.0 MeV to 5.3 MeV, though a further search for other proton groups with energies up to 8.5 MeV was made.

Excited states in ^{41}Sc have been extensively studied, using both resonance (Yo 68, En 67, Ma 70) and particle-transfer reactions (Yo 70, Yo 70a, Bo 65, Ge 69). Excitation energies from the present delayed-proton results are shown in Table 4-19, along with those from previous determinations; these results show remarkably good agreement with known levels in ^{41}Sc. As noted in Sec. IV A, the decay of the T = 3/2 state (peak 38) results in a new determination of the excitation energy of this level (combined with the recent resonance data from (Tr 73) or (Tr 73a)).

Marinov et al., (Ma 70) have reported ^{40}Ca(p, p) and (p, p') results for states between 5.8 and 7.0 MeV in excitation; for states below 6.1 MeV, no strong inelastic decay modes were seen. Some levels above this energy do exhibit significant partial widths for decays to excited states in ^{40}Ca. Three of the proton peaks discussed here have been assigned to transitions to excited states on the basis of results in Ref. (Ma 70). The state at ~ 6.09 MeV has a decay branch to the 3^-, 3.737-MeV state in ^{40}Ca, as well as a ground-state decay branch. The assignment of peaks 4 and 40 agree with this (see Table 4-19). The

Table 4-19. Energies of Unbound Levels in ^{41}Sc Fed by Allowed Beta Decay from ^{41}Ti, and a Comparison with Previous Results (Energies are in MeV ± keV).

Peak number	Final[a] state in ^{40}Ca	Deduced[b] energies in ^{41}Sc	Previous Work					
			Ref. Yo 68[c]		Ref. En 67[c]		Ref. Ma 70[c]	Other
2	g.s.	2.111 ± 15						2.096 ± 7 (3/2+,5/2+)[d]
								2.100 ± 20 3/2+[e]
								2.077 ± 20 3/2+,5/2+[f]
7	g.s.	2.671 ± 15	2.667 ± 3	(5/2+,9/2+)				
15	g.s.	3.414 ± 10			3.415 ± 2	1/2+		
16	g.s.	3.556 ± 20						
19	g.s.	3.815 ± 20	3.782 ± 3	5/2+	3.783 ± 2	5/2+		3.776 ± 10 5/2+[d]
21	g.s.	3.971 ± 15			3.970 ± 2	1/2+		
23	g.s.	4.241 ± 15	4.246 ± 4	5/2+	4.248 ± 2	5/2+		
24	g.s.	4.313 ± 20	4.329 ± 4					
25	g.s.	4.509 ± 30			4.505 ± 2	(3/2,5/2)+		
26	g.s.	4.661 ± 20			4.643 ± 3	1/2-[g]		
27	g.s.	4.782 ± 15			4.778 ± 2	(3/2,5/2)+		
28	g.s.	4.869 ± 15	4.872 ± 6	5/2+	4.868 ± 2	(3/2,5/2)+		
29	g.s.	4.929 ± 10			4.948 ± 4	(3/2,5/2)+		
30	g.s.	5.019 ± 25			5.023 ± 2	1/2+		
31	g.s.	5.088 ± 25			5.082 ± 2	(3/2.5/2)+		
34	g.s.	5.378 ± 15	5.380 ± 9		5.375 ± 2			
35	g.s.	5.575 ± 15	5.575 ± 10	5/2+	5.575 ± 2	(3/2,5/2)+		
36	g.s.	5.763 ± 20	5.780 ± 8					

continued. . .

Table 4-19. continued

37	g.s.	5.041 ± 10			5.038 ± 2	(3/2,5/2)+	5.837 ± 10		5.838 (3/2+) [h]
38	g.s.	5.939 ± 4 [i]							5.941 3/2+, T=3/2 [h]
39	g.s.	6.040 ± 25	6.017	1/2+ [j]			6.014 ± 10	1/2+	
40	g.s.	6.085 ± 20	6.087 ± 11				6.086 ± 10		
4	3.737 MeV	6.102 ± 15 [k]							
41	g.s.	6.135 ± 20	6.130	3/2+ [j]			6.132 ± 10		
42	g.s.	6.393 ± 30					6.413 ± 10	(5/2+)	
12	3.353 MeV	6.472 ± 25 [k]					6.477 ± 10		
13	3.737 MeV	6.938 ± 30 [k]					6.948 ± 10		

a) The excitation energies in ^{40}Ca are from (Ma 71).

b) The energies are calculated using a proton separation energy of 1.086 ± 0.001 MeV, (see Table 4-2).

c) The excitation energies given in this reference have been corrected for the change in proton separation energy (note b) above.

d) Ga 69.

e) Yo 70.

f) Yo 70a.

g) The assigned parity of this state precludes it being fed by allowed beta decay. Nevertheless, the deduced energy appears to be in agreement. The width of this level is 36 keV (En 67); it is possible that this is a doublet, part of which is fed by allowed β^+ decay.

h) Tr 73a.

i) This energy is already averaged, and part of the energy calibration, see Table 4-4.

j) This energy is from N. A. Brown, Rice University Ph.D. Thesis, 1963 (unpublished), quoted in ref. (Yo 68). It is not included in the average computed for E_x, however the J^π assignment is tentatively used.

k) This assignment is based, in part, on agreement with ref. (Ma 70) with respect to excitation energy and observed decay mode.

states at 6.47 and 6.94 MeV have been observed to decay primarily to the first and second-excited states in ^{40}Ca respectively; the present assignments follow this result. The ground-state branches for both of these states are so weak that they are not reliably observed in the present spectra--consistent with the results in Ref. (Ma 70).

Penetrability calculations for proton decay from states in ^{41}Sc are shown in Fig. 2-2, following the discussion in Sec. II D. It is apparent from this figure that for states below 6 MeV in excitation the ratio of penetrabilities for decay to the excited states vs that for decay to the ground state is extremely small.

A relatively strong peak (number 16) is observed at $E_p \sim 2.4$ MeV. Although it has a small ^{40}Sc component, the deduced half-life (after removal of the ^{40}Sc) is consistent with that of ^{41}Ti. It corresponds to a level at $E_x \sim 3.56$ MeV decaying to the ^{40}Ca ground state; however no such level has been previously observed in ^{41}Sc. A comparison with the mirror ^{41}Ca nucleus, shown in Fig. 4-15, indicates that the known $J^\pi = (1/2, 3/2, 5/2)+$ levels agree up to 4.3 MeV, except no mirror for the (3/2, 5/2)+, 3.54-MeV state in ^{41}Ca has been identified. The bracketed level at 3.556 MeV in ^{41}Sc shown in this figure follows from the present assignment for the 2.4 MeV proton peak. Supporting evidence for assignment of this new level comes from the inelastic scattering results of (Ma 70). These results show no states between 5.8 and 7.0 MeV in excitation that would correspond to the assignment of this 2.4-MeV proton peak to a state decaying to either of the first two excited states in ^{40}Ca. The lower positive parity states in mass-41 arise from particle-hole configurations; hence

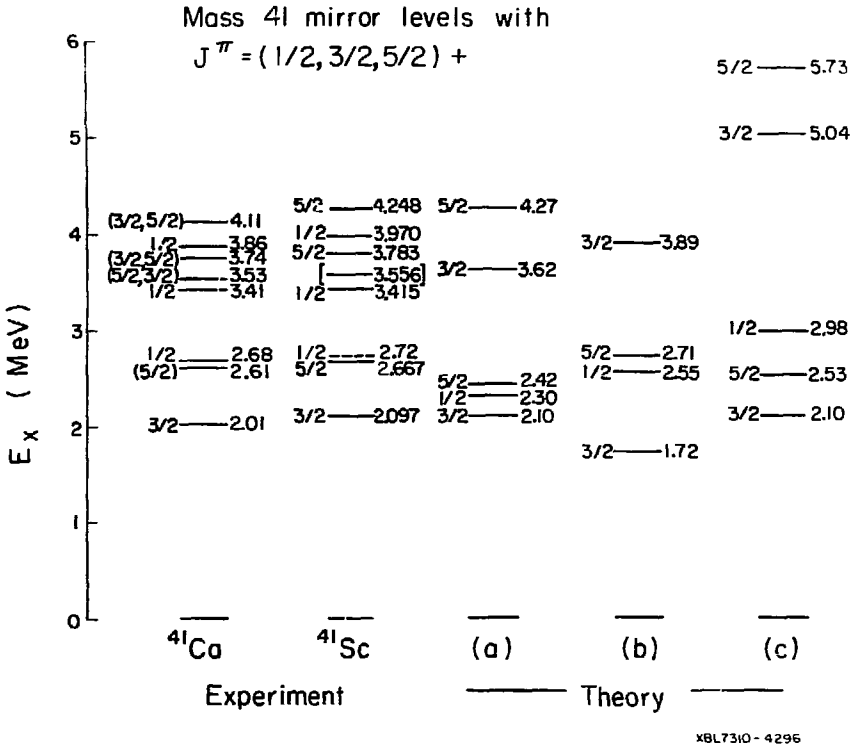

Fig. 4-15. Comparison of mirror levels in mass 41 below 4.3 MeV with J^{π} = (1/2, 3/2, or 5/2)+. The ^{41}Ca levels are taken from Refs. (Sm 68, Se 73a) while ^{41}Sc excitation energies are from Table 4-20. The level at 2.72 MeV (shown by dashed lines) is not observed in the delayed proton spectra, while the bracketed level at 3.56 MeV is from the present results. The theoretical predictions are from a) Ch 71, b) Di 68, and c) Ar 67.

they are only weakly excited in reactions from a ^{40}Ca target, and such a level at 3.5 MeV might not have been identifiable. Furthermore, the nearby 3.46-MeV state with $J^{\pi}=1/2-$, produced in particle-transfer reactions (Ge 69, Yo 70), has a width of ~ 60 keV (En 67) which could obscure a weaker transition to a state near 3.56 MeV.

Penetrability calculations are also of interest in determining the branching ratio for decay to the T = 3/2 state in ^{41}Sc, and the question of isospin purity discussed later. From these experimental results, only upper limits can be established for possible decay branches of the T = 3/2 state to the first three excited states. The proton energies for each of these possible decay modes unfortunately closely match energies of peaks arising from ^{40}Sc decay. Limits for such decay branches are shown in Table 4-20, along with penetrabilities calculated for each decay mode. The earlier results reported in (Go 73) showed a decay branch to the 0+, first-excited state with a relative intensity of 4 ± 2%. This peak (6) now appears to arise solely from the decay of ^{40}Sc (see Table 4-15).

It is apparent from the penetrabilities listed in Table 4-20 that decay of the T = 3/2 state to any of the energetically allowed excited states in ^{40}Ca is quite unlikely and that the upper limits extracted from the present data are probably too large. These possible decays therefore have not been included in the calculation of the branching ratio and ft value for beta decay to this state, nor in the calculation of the isospin impurity for this level.

The mass-excess of this narrow analogue level (Γ ~ 65 eV, Tr 73a) can be used, along with the known mass-excesses of the ^{41}K

. able 4-20. Possible Proton Decays of the Lowest $T = 3/2$ State in ^{41}Sc.

^{40}Ca Final State[a]				
E_x (MeV)	J^π	E_{lab}[b] MeV ± keV	Observed Intensity[c] I(%)	Penetrability[d] P
0.000	0+	4.734	24.3	0.39
3.353	0+	1.463	<0.7	0.0005
3.737	3-	1.089	<1.2	0.0003
3.904	2+	0.926	<0.4	0.0002
4.492	5-	0.352	e)	$\sim 1 \times 10^{-12}$

a) Excited states in ^{40}Ca are from Ref. (Ma 71).

b) Calculated assuming a separation energy of 1.086 MeV (Table 4-2).

c) These are in terms of percent of the total proton decay of ^{41}Sc.

d) These calculations are described in Sec. II D, with $r_0 = 1.3$ fm.

e) This proton energy is below the experimental range of observation.

ground state (Wa 71), and of the lowest T = 3/2 state in ^{41}Ca (Be 67, Ly 67), to predict the mass-excess of ^{41}Ti. Using the isobaric multiplet mass equation (IMME)(Ce 68) a value of -15.78 ± 0.03 MeV is obtained, in agreement with the prediction of -15.72 MeV from Kelson and Garvey (Ke 66). The calculations of reaction thresholds and beta-decay energies for ^{41}Ti shown in Tables 4-1 and 4-2 use the IMME result.

From the relative proton intensities, and energy-level assignments discussed above, branching ratios and absolute transition strengths for positron decay of ^{41}Ti have been calculated and are shown in Table 4-21. The ground-state decay branch is taken from the mirror ^{41}Ca → ^{41}K electron capture. Its very small magnitude for ^{41}Ti ($\sim 4 \times 10^{-5}$%) has no effect on the absolute beta-decay intensities to unbound levels.

Figure 4-15 shows a state in ^{41}Sc at 2.72 MeV with $J^{\pi} = 1/2+$ (En 67, Ge 69). Protons from the decay of this state were not observed in the present experiments, although their predicted position is near peak 8, which is predominately from ^{40}Sc decay. Since this level is the only known state with $J^{\pi} = (1/2, 3/2, \text{or } 5/2)+$ below 5.3 MeV whose corresponding proton decay was not observed, an upper limit on the relative intensity of this possible ^{41}Sc decay peak has been calculated to be $\leq 1.5\%$. This limit corresponds to a beta-branching ratio of $\leq 0.4\%$, and log $\underline{ft} \geq 6.04$. The uncertainty in the observed beta-decay branching ratios generated by this upper limit is incorporated in the errors for each decay shown in Table 4-21. This level, in fact, is the only previously known state in ^{41}Sc with a firmly established J^{π} not seen in the present delayed-proton data.

Table 4-21. Branching Ratios and ft Values for ^{41}Ti Positron Decay.

Energy In ^{41}Sc [a] (MeV ± keV)	J^{π} [b]	Proportion of Proton Decays (Beta Decay Branching Ratio [c]) (%)	ft [d] (10^3 sec)	Log ft (sec)
0.000	7/2-	~4 x 10^{-5} [e]	~3 x 10^{7} [e]	10.5
2.097 ± 6	3/2+	9.36 ± 0.60	61.5 ± 4.4	4.79 ± 0.03
2.667 ± 3	5/2+	5.24 ± 0.19	82.5 ± 3.9	4.92 ± 0.02
3.415 ± 2	1/2+	6.33 ± 0.24	45.6 ± 2.2	4.66 ± 0.02
3.536 ±20		3.57 ± 0.09	74.6 ± 3.1	4.87 ± 0.02
3.783 ± 2	5/2+	1.96 ± 0.20	119 ± 12	5.07 ± 0.05
3.970 ± 2	1/2+	1.19 ± 0.12	176 ± 19	5.24 ± 0.05
4.248 ± 2	5/2+	14.63 ± 0.95	12.0 ± 0.9	4.08 ± 0.03
4.329 ± 4		0.97 ± 0.27	173 ± 48	5.24 ± 0.12
4.505 ± 2	(3/2, 5/2)+	0.56 ± 0.10	268 ± 48	5.43 ± 0.08
4.643 ± 3		0.68 ± 0.10	201 ± 30	5.30 ± 0.06
4.778 ± 2	(3/2, 5/2)+	2.35 ± 0.10	53.2 ± 2.9	4.73 ± 0.02
4.868 ± 2	5/2+	3.76 ± 0.20	31.3 ± 2.0	4.50 ± 0.03
4.945 ± 7	(3/2, 5/2)+	7.52 ± 0.50	14.9 ± 1.1	4.17 ± 0.03
5.023 ± 2	1/2+	0.58 ± 0.05	182 ± 17	5.26 ± 0.04
5.082 ± 2	(3/2, 5/2)+	0.36 ± 0.05	280 ± 39	5.45 ± 0.06
5.375 ± 2		3.74 ± 0.14	22.1 ± 1.1	4.34 ± 0.02
5.575 ± 2	5/2+	1.75 ± 0.10	40.8 ± 2.7	4.61 ± 0.03
5.778 ± 7		0.53 ± 0.07	115 ± 16	5.06 ± 0.06

continued . . .

Table 4-21 (continued)

Energy In ^{41}Sc [a] (MeV ± keV)	J^{π} [b]	Proportion of Proton Decays (Beta Decay Branching Ratio [c]) (%)	$\underline{ft}$ [d] (10^3 sec)	Log $\underline{ft}$ (sec)
5.838 ± 2	(3/2, 5/2)+	5.36 ± 0.19	10.9 ± 0.5	4.04 ± 0.02
5.939 ± 4	3/2+, T=3/2	24.25 ± 0.50	2.22± 0.09	3.35 ± 0.02
6.018 ± 9	1/2+	0.73 ± 0.07	69.5 ± 7.5	4.84 ± 0.05
6.089 ± 6		1.77 ± 0.24	27.0 ± 3.8	4.43 ± 0.06
6.133 ± 9	(3/2)+	0.70 ± 0.07	65.6 ± 7.3	4.82 ± 0.05
6.411 ± 9	(5/2)+	0.36 ± 0.07	100 ± 20	5.00 ± 0.09
6.476 ± 9		0.75 ± 0.15	46.0 ± 9.1	4.66 ± 0.09
6.947 ± 9		0.99 ± 0.12	22.7 ± 2.9	4.36 ± 0.06

a) This is a weighted average of excitation energies listed in Table 4-19.

b) This is based on those listed in Table 4-19 and the present results assuming allowed beta decay. The ground state J^{π} is from (En 67).

c) With the exception of decay to the ground state, the absolute beta-decay branching ratios follow directly from the observed proton intensities.

d) The $\underline{ft}$ values are calculated using Q_{β} from Table 4-2 and $T_{1/2} = 80 \pm 2$ msec.

e) This branching ratio is calculated from comparison with the mirror decay (En 67).

For comparison, Fig. 4-15 also shows results of shell-model predictions for mass 41. Two of these earlier calculations, part b) Ref. (Di 68) and part c) Ref. (Ar 67), used a restricted basis space--allowing for $1f_{7/2}$ particles and $1d_{3/2}$ holes--which accounts, in part, for their lack of agreement with the experimental data. A more complete calculation (Ch 71), shown in part a), uses single particle states in $1f_{7/2}$, $2p_{3/2}$, and $2p_{1/2}$ orbits, and $1d_{3/2}$ and $2s_{1/2}$ hole states. The low energy levels compare well with those identified experimentally, while the levels above 3 MeV are not reproduced as adequately.

The excitation energies listed in Table 4-21 are a weighted average of present and previous results shown in Table 4-19. No allowance has been made in the beta-decay branching ratios for γ-decay, since the radiative widths for levels in ^{41}Sc are quite small (Yo 68). For those levels with $J^{\pi} = (1/2, 3/2, 5/2)+$ and for which Γ_{γ} and Γ are known, Γ_{γ}/Γ is $\leq 0.5\%$ (Yo 68, En 67).

The proposed decay scheme for ^{41}Ti delayed-proton emission is shown in Fig. 4-16. Beta-decay branching ratios and log ft values determined from this work are given for each decay.

3. Discussion and conclusions

a. ^{37}Ca β^+ decay and effects on the solar neutrino cross-section.

Several predictions have been made for beta-decay transition strengths to states in ^{37}K, primarily to estimate the solar neutrino capture cross-section for the ^{37}Cl(ν, e^-)^{37}Ar reaction (Ba 64, En 66, La 72). These estimates for log ft values and the corresponding excitation energies appear in Table 4-22 along with results from the present experiments.

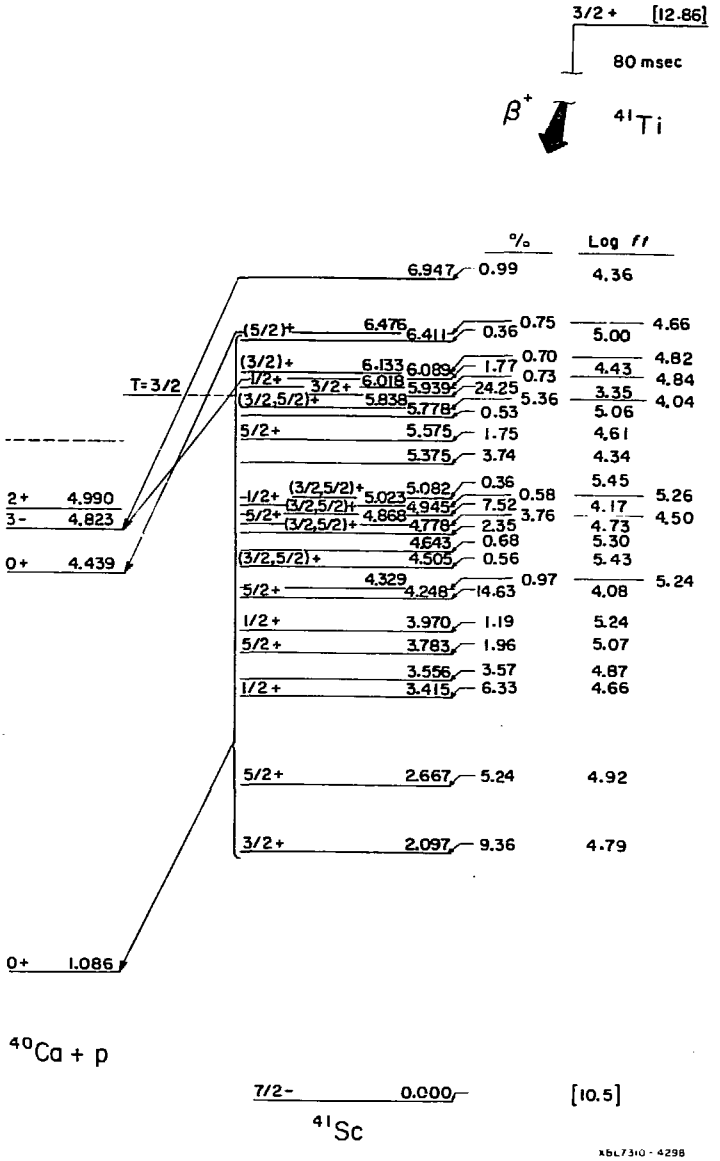

Fig. 4-16. Proposed decay scheme for ^{41}Ti. All excitation energies are weighted averages from Table 4-21. The branching ratios and ft values for all unbound levels are from the present work. The log ft for decay to the ground state is from the mirror.

Table 4-22. Comparison of Calculated Excitation Energies and log ft Values with Experimental Results for ^{37}Ca.

Experimental Results				Theoretical Predictions					
Present[a]		Previous (Po 66)		Ba 64		En 66		La 72	
E_x (MeV)	log ft (sec)	E_x (MeV)	log ft (sec)	E_x (MeV)	log ft (sec)	E_x (MeV)	log ft (sec)	E_x (MeV)	log ft (sec)
0.000	5.10	0.00	[5.06][b]	0.00	[5.06][b]	0.00	4.45	0.00	5.14
1.368	5.08[c]	1.36	[4.9][c]	1.46	4.48	1.36	4.71	1.47	5.44
2.750	4.87	2.75	[4.9][c]	1.57	4.34	2.74	3.81	2.65	4.36
		3.08	(>5.4)						
3.617	4.83	3.62	4.8					3.62	4.68
3.840	4.72	3.84	4.8						
		(4.12)	5.0						
4.417	5.12	4.40	4.7						
4.503	4.84								
4.665	5.04	4.66	4.5					4.71	4.12
		4.83	(> 4.8)						
5.018	4.71	5.02	3.2[d]						
5.047	3.30	5.05		5.12	3.28	5.07	3.27	5.05	3.30
5.118	4.17								

continued . . .

Table 4-22 (continued)

Experimental Results				Theoretical Predictions					
Present[a]		Previous (Po 66)		Ba 64		En 66		La 72	
E_x (MeV)	log ft (sec)	E_x (MeV)	log ft (sec)	E_x (MeV)	log ft (sec)	E_x (MeV)	log ft (sec)	E_x (MeV)	log ft (sec)
5.317	4.85								
5.449	5.11							5.53	3.77
								5.79	4.47
								5.91	4.34
6.016	4.77	6.03	4.5					6.03	4.77
		(6.32)	4.7						
		6.54	4.6						
		6.96	4.5						

a) Taken from Table 4-18.

b) This log ft is from the previous experimental value for the mirror ^{37}Ar electron capture decay as computed in (Ba 64).

c) Estimated by assigning the remaining beta-decay strength to known, but unobserved level(s) with J^{π} = (1/2, 3/2, or 5/2)+.

d) The earlier work did not resolve the T = 3/2 state decay protons from those decays from nearby levels, hence a slightly lower ft was adopted by these authors.

The earlier delayed-proton data (Po 66) are also shown for comparison. Both Bahcall (Ba 64) and Engelbertink (En 66) calculated ft's for decay to the first three levels with J^{π} = (1/2, 3/2, and 5/2)+ and for the transition to the lowest T = 3/2 state, using a limited basis space, while Lanford and Wildenthal (La 72) employed a full sd shell basis space. These more complete calculations still fail to predict several of the states between 3 and 5 MeV fed by allowed beta decay. As noted in (La 72), this lack of agreement probably arises from the restrictions still present in their basis space for the calculations, since some of the states are undoubtedly due to particle excitations into the lf-2p shell.

Since ~ 62% of the total beta-decay strength populates the ground state plus T = 3/2 state (5.05 MeV), it is unlikely that new information on the beta branching will cause a dramatic change in the predicted solar neutrino capture cross-section. The effect of the present experimental results on this cross-section has been estimated using the method detailed by Bahcall (Ba 64). The largest change occurs in the estimated cross-section contribution for capture to the T = 3/2 state. In his later paper, Bahcall (Ba 66) apparently used log ft = 3.2 for this decay, which allowed for unresolved contributions from nearby T = 1/2 states to the total decay strength (Po 66). As noted earlier, the present results have resolved these components and the capture cross-section contributions can be computed separately for each level. Using the ft values shown in Table 4-18, the change in the predicted solar neutrino capture cross-section (Ba 66) is

$$\sigma_{\nu}(\text{present}) \sim 0.97\ \sigma_{\nu}(\text{Bahcall}) \sim 1.31 \times 10^{-42}\ \text{cm}^2.$$

Clearly, the present result has no significant effect on the estimates for the capture cross-section.

It is also of some interest to estimate the magnitude of possible mixing between the 5.047-MeV, 3/2+, T = 3/2 state and the nearby state at 5.018 MeV if it has $J^{\pi} = 3/2+$. If one assumes that the entire decay strength to this state is due to mixing with the analogue state, then using Eqs. (2-14 and 2-20), a^2 can be estimated from the ft value for this decay to be ~ 4% (assuming $\langle \sigma \rangle^2 = 0$). The corresponding charge dependent matrix element, estimated from Eq. 2-22, is −6 keV, within the range for such matrix element magnitude as discussed in (Bl 66 and Be 72).

The mixing gives an estimate for the probable lower limit on the isospin purity of the T = 3/2 state of ~96%. Such an impurity level in this state would have a negligible effect on the estimate for the predicted neutrino capture cross-section in the mirror.

b. ^{41}Ti beta decay and the isospin purity of ^{41}Sc (T = 3/2).

(i). The antianalogue state and the Gamow-Teller matrix element.

The T = 3/2 analogue levels in mass 41 can be described as:

$$[(f_{7/2})^2 \; J = 0,\; T = 1 \;\otimes\; (d_{3/2}^{-1})]\; J = 3/2,\; T = 3/2\,. \qquad (4\text{-}1)$$

The antianalogue configuration has the same components, but recoupled to T = 1/2 viz.,

$$[(f_{7/2})^2 \; J = 0,\; T = 1 \;\otimes\; (d_{3/2}^{-1})]\; J = 3/2,\; T = 1/2\,. \qquad (4\text{-}2)$$

Particle-hole states in mass 41, mainly in the $T_z = +1/2$ isobar ^{41}Ca, have been studied and identified through direct-reactions, including ^{39}K(^{3}He, p) (Be 67), ^{42}Ca(^{3}He, α) (Ly 67), and ^{42}Ca(p, d) (Sm 68, Ma 72). They have also been observed in ^{40}Ca(d, p) (Be 65, Se 73a) through 2p-2h components in the ^{40}Ca ground state. All these reactions show that the main $d_{3/2}$ hole strength is in the lowest 3/2+ state in ^{41}Ca at 2.017 MeV, with possibly some fractionation to levels at 3.7 and 4.8 MeV. However it is not clear from the data whether these latter two levels have $J^\pi = 3/2+$ or 5/2+, or the exact strength of the antianalogue component, if any. Neither of these two levels was seen in ^{41}K(^{3}He, t) (Sc 70), while the analogue and 2.02 MeV levels were strongly populated. Experimental estimates of the amount of antianalogue strength in the 2.02-MeV mirror level in ^{41}Ca range from 80% (Ly 67) to 100% (Ma 72).

In the $T_z = -1/2$ mirror ^{41}Sc, the lowest $J^\pi = 3/2+$ state at 2.1 MeV was seen in ^{40}Ca(^{3}He, d) (Bo 65), again through 2p-2h components in ^{40}Ca (g.s.). The ^{40}Ca(d, n) reaction (Ge 69) to this state exhibits the same strong $\ell = 2$ stripping pattern as does the analogous (d, p) reaction to its mirror in ^{41}Ca. These arguments, along with the direct reaction evidence in ^{41}Ca, serve to locate the main antianalogue strength at ~ 2.0 MeV in ^{41}Sc.

Finally, several shell model predictions for 2p-1h states in mass-41 have been made (Sa 67, Di 68, Ar 67, Ch 71); they all generally agree that the main component of the antianalogue configuration (Eq. 4-2) is concentrated in the lowest $J^\pi = 3/2+$ state (the last three calculations are shown as part of Fig. 4-15). The other primary configuration predicted to contribute to 3/2+ states in similar to that in Eq. (4-2), but

with the two $f_{7/2}$ nucleons coupled to J = 1, T = 0. This recoupled configuration is predicted to have components in the three calculated $J^{\pi} = 3/2+$ states below 7 MeV (Sa 67, Be 67) with the smallest contribution to the lowest $J^{\pi} = 3/2+$ state.

On the basis of the experimental and theoretical evidence just discussed, the antianalogue state configuration is assumed to be concentrated solely in the 2.1-MeV level in ^{41}Sc. The Gamow-Teller matrix element $\langle \sigma \rangle_{A.A.}$, for beta decay to the antianalogue state can then be calculated ($\langle 1 \rangle^2_{A.A.} = 0$ assuming no substantial mixing with the T = 3/2 state) to be 0.253 ± 0.013. This value is related to the matrix element for the superallowed decay, $\langle \sigma \rangle_{S.A.}$, as shown in Eq. 2-24, and $\langle \sigma \rangle^2_{S.A.} = 0.032 \pm 0.002$.

(ii). Isospin purity of the lowest T = 3/2 state in ^{41}Sc. Using this value for $\langle \sigma \rangle^2_{S.A.}$, the amount of isospin purity (a^2) for the T = 3/2 state can be calculated. From the experimental determination of $\underline{ft}_{S.A.}$, and Eqs. (2-14) and (2-20).

$$a^2 = (90.9 \pm 4.1)\%; \langle \sigma \rangle^2_{S.A.} = 0.032.$$

In the extreme case of $\langle \sigma \rangle^2_{S.A.} = 0$ (where deviations from the calculated value can only be due to isospin impurities)

$$a^2 = (92.6 \pm 3.8)\%.$$

In view of this ~ 8 to 10% impurity for the T = 3/3/2 state, it would be of interest to ascertain those states which predominate in the mixing with the analogue state. Recently, contributions to the partial widths for the isospin-forbidden proton decay of T = 3/2 states

have been calculated (Au 71). These results indicate that a major term in these amplitudes comes from mixing between the configuration state (i.e., the antianalogue state) and the analogue level; the estimated mixing is of the order of 1% for ^{41}Sc. However, this prediction uses a value of the charge-dependent matrix element (Eq. 2-22) that is approximately a factor of 5 to 10 larger than those values measured in the s-d shell or in the $f_{7/2}$ shell (Bl 66, Be 72).

It is of course possible that mixing with other states occurs, which might aid in explaining the isospin impurity found in the present results. One such candidate is the state at 5.838 MeV, which is ~100 keV away from the T = 3/2 state, and is populated by significant beta-decay strength. The possible mixing due to this level can be estimated from Eqs. (2-14) and (2-20), and the assumption that the decay strength arises solely via mixing with the T = 3/2 state. This gives an admixture of ~ 19%, and the resulting charge-dependent matrix element from Eq. (2-22) is ~ 43 keV. The latter is well within the tabulated values for this matrix element (Bl 66, Be 72). Although this overestimates the measured amount of isospin mixing with the T = 3/2 state, the assumption that the entire beta-decay strength observed for the 5.838-MeV state arises from this mixing is most likely an oversimplification. The Gamow-Teller matrix element undoubtedly contributes as well, which would serve to decrease the size of the mixing.

The observed isospin purity of the T = 3/2 state in ^{41}Sc of $\geq$ 91% is consistent with previous determinations of isospin purity for other T = 3/2 states--notably those in ^{17}F and ^{33}Cl (Ha 71). It appears

that in the present case mixing with nearby states, and possibly with the antianalogue state, are plausible sources of the observed impurity, and that the former is the more significant source for such mixing.

E. Results for ^{23}Al

Although the masses and decay properties of $T_z = -3/2$ nuclei in the $A = 4n+1$ series have been the subject of considerable study, almost no information has been available for their counterparts in the $A = 4n+3$, $T_z = -3/2$ series. Mass measurements (Ce 69) using the (p, ^{6}He) reaction have established the particle stability of ^{23}Al (the lightest, nucleon-stable member of the 4n+3 series). As such, it should exhibit beta-delayed proton decay, although much weaker than the comparable members of the 4n+1 series. The results discussed here have been reported in (Go 72).

1. Discussion of data

Proton beam energies used for the ^{24}Mg(p, 2n) reaction (on 99.96% -enriched targets) ranged from 30 to 40 MeV; as shown in Table 4-1, even the lowest of these energies can produce ^{20}Na, ^{24}Al or ^{24}Al^m in competing reactions.

a. Pulsed-beam experiment. The description of the pulsed-beam, shielded-detector apparatus (wheel) has been given in Sec. III D. The protons following decay of ^{23}Al were detected in the 8-μm ΔE 50-μm E telescope mounted as shown in Fig. 3-9. In order to observe low energy protons as well as alpha particles, singles spectra were recorded from the 8-μm ΔE detector, and from an additional 14-μm detector mounted in an adjacent position. This system was used for the

excitation function measurements, at beam energies of 30.3, 31.8, 33, 35, and 40 MeV. Half-life data were also taken, as described in Sec. III C.

b. He-jet experiments. Although this method had a lower overall efficiency (see discussion in Appendix A), it afforded both a higher particle resolution, and a lower background. In addition, as described in Sec. III C, it provided a means of doing an anticoincidence experiment to aid in reducing the background at low energies due to ^{16}O recoil nuclei from the beta-delayed alpha decay of ^{20}Na. (Thus ^{16}O nuclei in coincidence with the alpha particles detected in this large area detector were rejected from the ΔE-counter spectrum.)

The helium-jet experiments were done at a 40-MeV bombarding energy, and used a 6-μm ΔE and 50-μm E detector telescope. Half-life data were also acquired using the methods previously described.

c. Proton spectra and half-life data. An identified proton spectrum following decay of ^{23}Al is shown in Fig. 4-17. This spectrum was acquired using the helium-jet technique; spectra obtained using the wheel system were similar, though with peak widths of ~ 70-80 keV FWHM due to proton energy loss in the thick target. In both cases the protons at energies $\gtrsim$ 1.0 MeV exhibited a half-life consistent with that for the main peak, but were always too weak to reliably analyze.

The original data taken using the wheel technique were calibrated using very low-intensity H_2^+ beams of 0.63 and 1.15 MeV/nucleon elastically scattered from a Au target directly into the 4-μm ΔE 50-μm E detector telescope (the wheel having been stopped so as to expose the detectors to the target). The proton spectrum acquired with the helium-

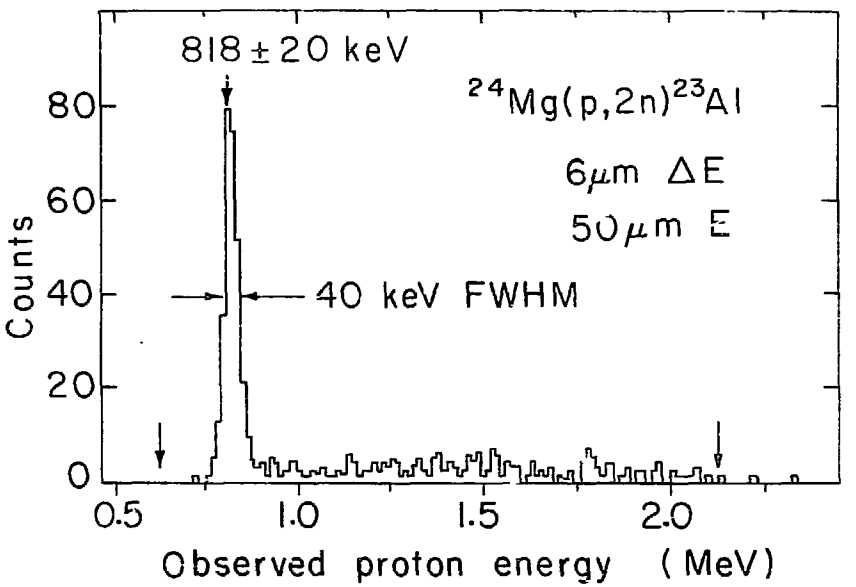

XBL 7110-4530A

Fig. 4-17. Identified protons following beta decay of ^{23}Al. This spectrum was acquired using the helium-jet system. Vertical arrows designate the energy range over which protons could be observed.

jet could not be similarly calibrated. However, with the higher resolution ^{40}Sc results reported in Sec. IV D this nuclide, produced in the ^{40}Ca(p, n) reaction, could be used for calibration of the ^{23}Al proton data from the helium-jet experiments. The resulting ^{23}Al proton energy is 818 ± 20 keV, as shown in Fig. 4-17. (This more accurate value agrees with that noted in (Go 72), which reported results based on the H_2^+ calibration only.)

This main proton peak was observed to have similar half-lives in each of the two experimental methods. The resulting average half-life is 470 ± 30 msec. This value eliminates any possibility of either ^{24}Al or ^{24}Al^m as a source for these protons. However, it is disconcertingly similar to that for ^{20}Na (see Table 4-1), which can in principle decay by electron capture to proton unbound levels in ^{20}Ne (as discussed in Sec. IV B above), resulting in protons $\lesssim$ 1.0 MeV.

The yield of ^{23}Al protons, along with ^{20}Na alpha decay data taken simultaneously, was obtained as a function of bombarding energy as described above. The resulting excitation function is shown in part a) of Fig. 4-18. No proton yield was observed at the 30.3-MeV bombarding energy, consistent with the calculated ^{24}Mg (p, 2n) ^{23}Al threshold of 30.78 ± 0.08 MeV (Table 4-1). The maximum production cross-section for this 818-keV proton peak is $\approx$ 220 nb.

The observed ratio of protons to 4.42-MeV α particles (To 73a, also Fig. 4-6 above) is shown in part b) of Fig. 4-18 as a function of bombarding energy. The 4.42-MeV alpha yield was determined from the dE/dx loss in either of the two independent ΔE detectors shown. This proton-to-alpha yield ratio can be seen to drop by a factor of ~10

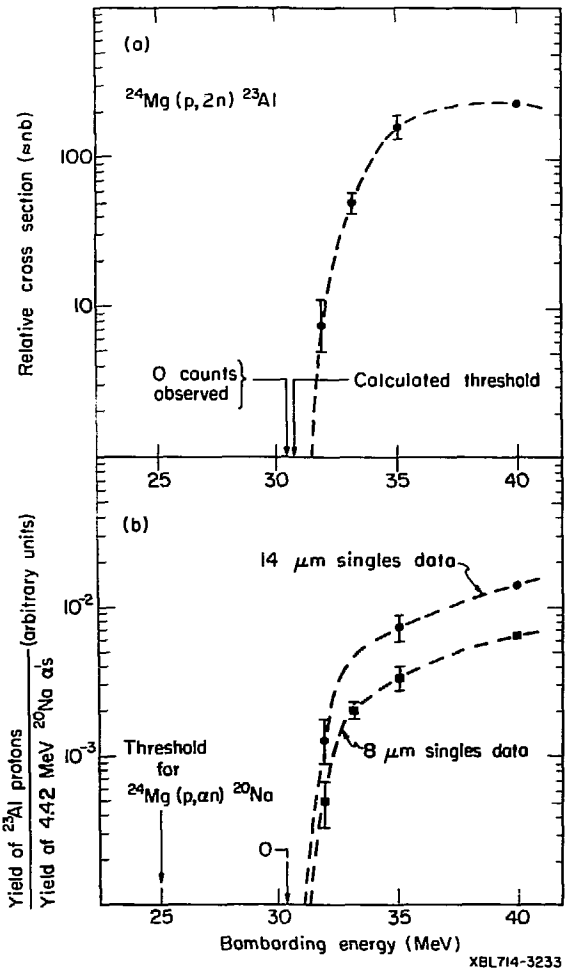

Fig. 4-18. a) An excitation function for ^{23}Al protons acquired with the wheel apparatus. Where error bars are not shown, they are smaller than the data points. b) The yield ratio of ^{23}Al protons to 4.42-MeV α particles from ^{20}Na as a function of bombarding energy. The ordinate gives the approximate absolute ratio for protons to alphas observed in the 8-μm ΔE detector.

as the beam energy is lowered 8 MeV, indicating that ^{20}Na is not the source of these protons.

It is of interest to note that at 40 MeV bombarding energy, the ratio of the sum of all observed ^{20}Na alpha groups to the 818 keV-proton intensity is ~10^3. The ordinate in Fig. 4-18b is approximately the absolute cross-section ratio for ^{23}Al protons (818 keV group) to ^{20}Na alphas (4.42 MeV group) as detected in the 8-μm counter. Hence this yield ratio as a function of bombarding energy is important in eliminating the possibility of a very weak ^{20}Na K-capture branch as a potential source for the observed proton peak. There are no other sources of such decay protons--either as target contaminants, or as competing reactions--with the exception of ^{23}Al.

2. Analysis and conclusions.

The proposed decay scheme for ^{23}Al is shown in Fig. 4-19. The excitation energies and J^π assignments for levels up to 3 MeV in ^{23}Mg are from (Ha 70), (En 71), and (Ne 72). The location and J^π assignment for the lowest T = 3/2 state was determined in ^{25}Mg(p, t) experiments reported by Hardy et al., (Ha 69). Similarly, (p, ^{3}He) data established the spin and parity of the T = 3/2 analogue level in ^{23}Na (Ha 69). The ground-state spin-parity for ^{23}Al is assumed to be 5/2+, based on these results for the T = 3/2 analogue levels, and the J^π = 5/2+ ground state in the ^{23}Ne mirror. Assuming the proton decay peak arises from decay to the ^{22}Na ground state, the observed peak energy corresponds to a previously unreported state at 8.434 MeV, which is restricted to J^π = (3/2, 5/2, or 7/2)+ if populated by allowed β^+ decay.

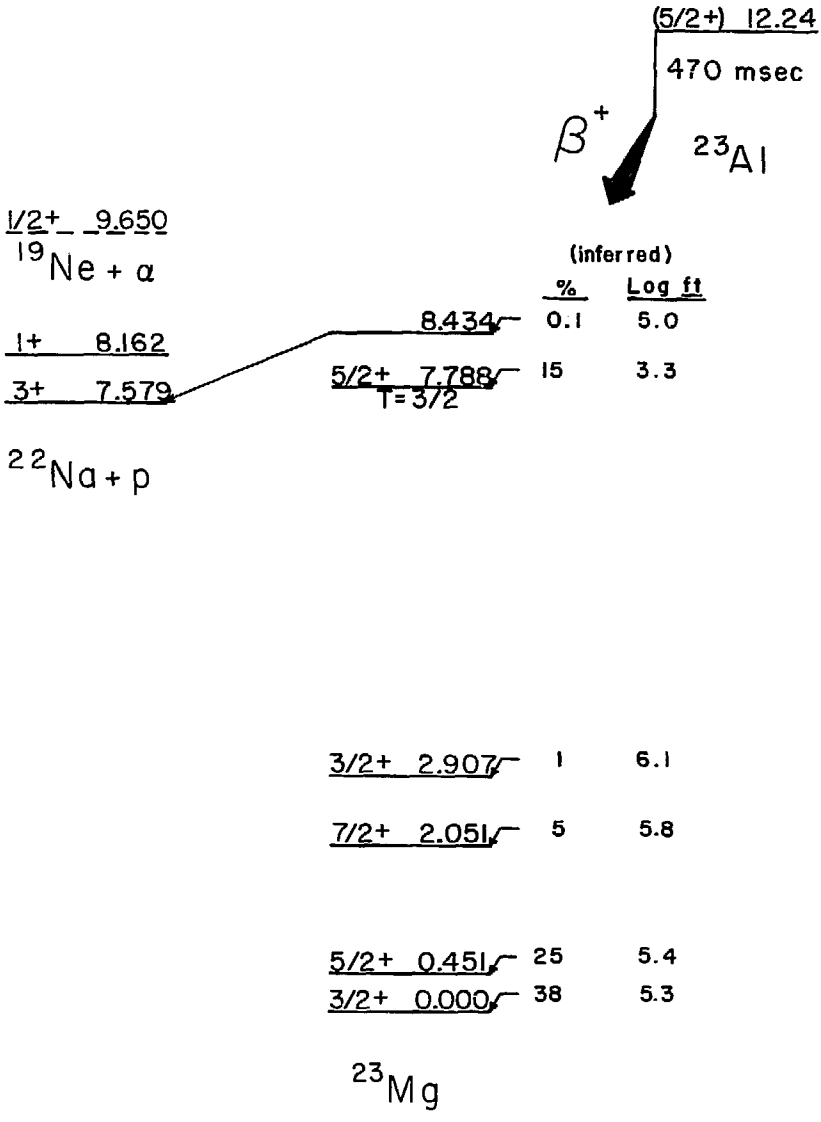

XBL 7310-1336

Fig. 4-19. Proposed decay scheme for ^{23}Al. The excitation energies for states in ^{23}Mg are discussed in the text. The inferred beta-decay branching ratios and log *ft* values are discussed there also.

The inferred branching ratios and log ft values for positron decay to the bound levels are taken from the measured branching ratios for the mirror ^{23}Ne β^- decay (Ch 72). Using these values and the ^{23}Ne half-life as reported in (En 67), the ft values for ^{23}Ne were calculated following the description in Sec. IIA. The mirror levels in ^{23}Mg have been identified (Ne 72) and the corresponding log ft values and positron-decay branching ratios are shown in Fig. 4-19 (no allowance for $(ft)^+/(ft)^-$ has been made).

The log ft value for the superallowed β^+ decay to the T = 3/2 state can be estimated to be ~ 3.3 from Eq. (2-14), similar to its counterparts in the A = 4n+1 series. The inferred branching ratio follows directly from this assumption. Likewise, the approximate beta-decay branching leading to the 8.43-MeV state follows from the assumption that the log ft ~ 5.0 for this allowed decay (Go 66).

As the decay scheme in Fig. 4-19 shows, the T = 3/2 state is unbound to proton decay by ~ 200 keV. Penetrability calculations indicate that the partial width for this possible decay is approximately the same order of magnitude as that for a typical 7.8-MeV M1 γ ray in this mass region (Sk 66). The experimental search for this low energy proton, the details of which are described earlier and in Sec. IIIC, produced no positive result. These data, in conjunction with the beta-decay branching ratios shown in Fig. 4-19, permit a crude estimate of $\Gamma_\gamma/\Gamma_p \geq 50$ for the isospin-forbidden proton decay of the T = 3/2 state.

As a note of minor historical interest, ^{23}Al was thought to have been identified as one of the products from proton bombardments of a natural Mg target (Ty 54). These bombardments in the circulating

beam of a 200 MeV synchrocyclotron were done at proton energies of 23, 50, and 80 MeV. Gross beta activity was detected in a scintillator. A 0.13-sec activity produced at 23 MeV was thought to be from either ^{23}Al or ^{22}Mg. As can be noted from the present excitation function data, this bombarding energy is below the ^{23}Al threshold. The 0.13-sec activity is probably due to ^{24}Al^{m}, as ^{22}Mg has a half-life of ~ 4 sec (En 67). However, at a 50-MeV proton bombarding energy, activity with a ~ 0.4 sec half-life was reported, but no identification was made. In retrospect, both ^{23}Al and ^{20}Na (having nearly identical half-lives) could contribute to this ~ 0.4-sec β^+ activity. Using the present ^{23}Al results as shown in Fig. 4-19 and the maximum proton production cross-section noted earlier, the total ^{24}Mg(p, 2n)^{23}Al cross-section at 40 MeV is ~ 220 μb. The ^{24}Mg (p, αn)^{20}Na cross-section can be estimated from the observed alpha to proton ratio of ~ 6.5×10^{-3} (from Fig. 4-18b), and the positron branching to the 10.26 MeV state in ^{20}Ne of ~ 2.9% (To 73a); hence the cross-section for this reaction at 40 MeV is ~ 1200 μb. The 0.4-sec activity originally observed at 50 MeV is therefore probably due mostly to ^{20}Na β^+ decay, with an ~ 15% contribution from the positron decay of ^{23}Al.

V. SUMMARY AND CONCLUSIONS

Results of high-resolution particle-decay experiments have been presented for several of the light-mass delayed-proton precursors. These observed particle energies have led to assignment of the decays to existing or, in some cases, new energy levels. For those assigned to previously known excited states, the agreement between the results of the present observations and the published values is excellent.

As detailed in the text, the proton intensities have been used to derive transition strengths for the preceding beta decay. For ^{41}Sc, the absolute $\underline{ft}$ values yield information on the degree of isospin admixing in the lowest T = 3/2 state. This value of ~ 8% is of the same order as those determined in previous measurements for ^{17}F and ^{33}Cl (Ha 71).

The ratios of mirror transition rates determined for masses 21 and 25 are consistent with those for other odd mass mirrors, $\underline{e.g.}$, masses 9 (Wi 71), 13 (Wi 71a), 17 (Ha 71), and 29 (Es 71a). The results for these six mirror pairs have been plotted as a function of $W_0^+ + W_0^-$ in Fig. 5-1. As can be seen, there is no evidence for a systematic change in $(\underline{ft})^+/(\underline{ft})^-$ as a function of decay energy. As discussed in a recent analysis by Wilkinson, $\underline{et\ al.}$, (Wi 72), the possible origin of these asymmetries in the odd-A systems as due to lack of perfect analogue symmetry in the final states should be studied. In the cases of ^{21}Mg, and ^{25}Si, a measure of the proton to gamma yield would provide information on the beta branching to bound levels; such results combined with the ground-state transition strength from the mirror

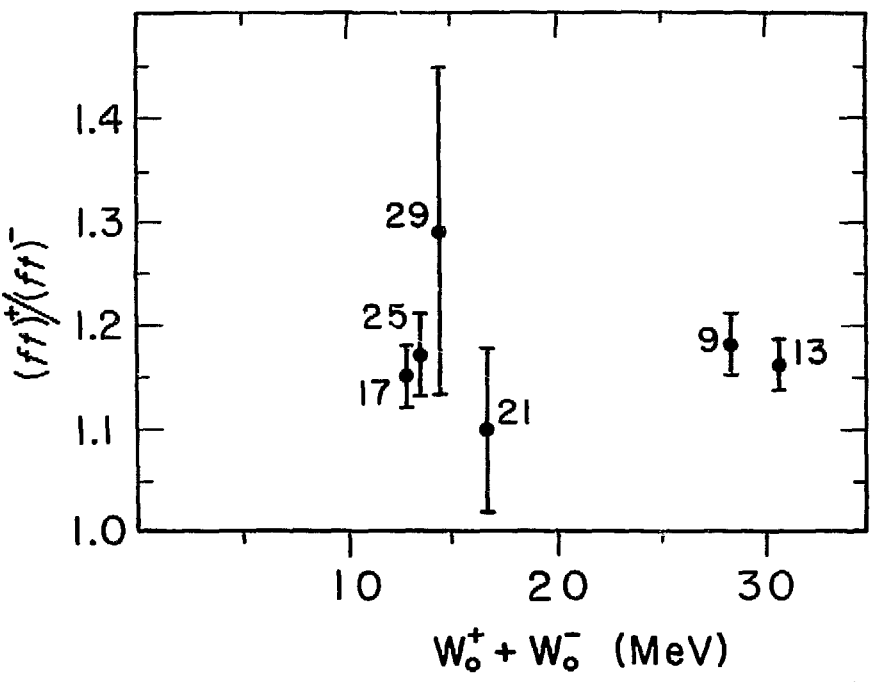

Fig. 5-1. The ratio of mirror beta decay rates as a function of the sum of the decay energies. The points are labelled with the mass of the mirror pair.

(as was done for ^{33}Ar (Ha 71)) would aid in checking the assumption of isospin purity in the T = 3/2 state (which is the basis for obtaining beta-decay branching ratios for these nuclei in the present work). In any event, if the T = 3/2 state in either mass 21 or 25 contained ~10% admixture (as has been observed in some of the members of this A = 4n+1 series), the resulting effect on $(\underline{ft})^+/(\underline{ft})^-$ would be a reduction of ~0.05, which is not large enough to fully account for the observed discrepancies in mirror decay rates.

The results presented here for ^{23}Al employ a technique which could be applicable for the characterization of decay properties of other nuclei that might be particle stable in this series. Although ^{23}Al is the lightest, nucleon stable member, ^{27}P, ^{31}Cl and ^{35}K are all predicted to exist (Ke 66). Like ^{23}Al, the other potential beta-delayed $T_z = -3/2$, A = 4n+3 proton emitters would have very small decay branches to particle-unbound levels in the daughter nuclei, since their proton separation energy is quite high--greater than 5.9 MeV (Wa 71). Experiments searching for these nuclei and higher-mass members of the series would be valuable since they are expected to lie near the edge of stability, and could lead to the observation of new examples of proton radioactivity.

ACKNOWLEDGMENTS

The excellence of the experimental facilities at the Berkeley 88-inch cyclotron is equalled by the outstanding staff at Building 88. I am indebted to them for their invaluable contributions toward the completion of this work, and I gratefully acknowledge their support.

I am particularly appreciative of the support, guidance and criticisms of my advisor, Professor Joseph Cerny. His enthusiasm for this work has been inspiring. I am also grateful to Dr. Bernard Harvey, Dr. David Hendrie, and Dr. Homer Conzett for their support and suggestions, and to Dr. John Hardy, who contributed substantially to my ability and interest in experimental research.

A considerable portion of this work was done with the collaboration of Dr. Richard Gough; his advice, assistance, and experimental expertise are a significant part of the successful completion of this work. I also wish to thank Dr. Hans Harney, and Dr. Nick Jelley for their help, and Dr. Creve Maples for the use of several of his computer programs.

To all those present and former graduate students who inhabited Building 88 about the same time as I, I am grateful for their assistance on experiments, their friendship, and for all those relevant, irreverent and otherwise good times: Joel Moss, Hank Brunnader, George Goth, John Esterl, Mike Zisman, Gordon Wozniak, John Macdonald, Ken Wilcox, Bob Weisenmiller, Dave Vieira, Leonard Ho, and especially

Joe Sherman, my well-informed office mate.

I want to especially thank my wife, Joan, for her love and support during my 6 years as a graduate student. She has been able to alter her priorities to accomodate the insistent demands of experimental research and thesis writing, and in the end maintain her enthusiasm for the future.

This work was supported by the U. S. Atomic Energy Commission.

APPENDIX A

Helium Jettery

This section describes empirical observations regarding some of the experimental parameters involved with the transport of recoil nuclei with a helium-jet system. Details of its construction and use have been given in Sec. III B. Although this method of transport of radioactive species has been in use for some time (see Ma 69 and references therein), only recently have there been attempts to explore the chemistry involved in the transport process.

Table A-1 lists the various reactions considered, along with a brief description of the experimental conditions. The quantity in the last column is the product of reaction cross-section and transport efficiency. This is calculated from (following the description in Es 71a):

$$\sigma\epsilon = \left(\frac{C}{BR \cdot \Omega}\right) \cdot \left(\frac{M}{N_o F_a F_i T_e}\right) \cdot \left(\frac{Z_p e}{Q}\right) \cdot \left(\frac{\lambda t_b (1 - e^{-\lambda T_c})}{\left(1 - e^{-\lambda t_b}\right) \cdot \left(e^{-\lambda t_d} - e^{-\lambda (t_d + t_c)}\right)}\right). \quad \text{(A-1)}$$

The first factor is the number of counts, C, in the peak or peaks of interest, the beta decay branching ratio(s), BR, and Ω, the fraction of a unit sphere subtended by the detector telescope. The second factor is the inverse of the number of target nuclei available for the reaction of interest, where M is the target molecular weight, F_a and F_i are the fractional atomic and isotopic abundances, respectively, N_o is Avogadro's number, and T_e is the effective target thickness. For experiments where the recoils of interest escape from the target (as in the He-jet experiments),

Table A-1. Observed yield from various reactions producing beta-delayed-particle precursors.

Entry number	Reaction	Beam Energy[a] (MeV)	Brief description of experimental parameters[b]	$\sigma\epsilon$[c] (nanobarns)
1	$^{40}Ca(^{3}He, 2n)^{41}Ti$	29.5		300
2		36.5		340
3		60		320
4	$^{40}Ca(^{3}He, 2np)^{40}Sc$	29.5		6500
5		36.5		10600
6		60		20000
7	$^{40}Ca(^{3}He, 2na)^{37}Ca$	36.5		40
8		60		190
9	$^{40}Ca(^{3}He, 2n)^{41}Ti$	29.5	pure[d] He	65
10		60	84-cm-long capillary[e]	100
11	$^{24}Mg(^{3}He, 2n)^{25}Si$	29.5		5200
12		29.5	pure[d] He	3100
13		40		1800
14		40	~5% air + 1,2-ethanediol bubbler[f]	7300
15		60		1800
16	$^{36}Ar(^{3}He, 2n)^{37}Ca$	40		150
17	$^{28}Si(^{3}He, 2n)^{29}S$	29.5		20[g]
18	$^{20}Ne(^{3}He, 2n)^{21}Mg$	29.5	Ne + He mixture	1100
19	$^{32}S(^{3}He, 2n)^{33}Ar$	29.5		<50[h]
20	$^{40}Ca(p, n)^{40}Sc$	20	~4% N_2 + 1,2-ethanediol bubbler[f]	37000
21	$^{24}Mg(p, 2n)^{23}Al$	40		20000
22	$^{24}Mg(p, \alpha n)^{20}Na$	40		91000[i]
23	$^{40}Ca(^{12}C, 3n)^{49}Fe$	(78)72	~10% air + 1,2-ethanediol bubbler[f]	60[j]
24	$^{20}Ne(^{12}C, 3n)^{29}S$	(78) 71.5	~10% air + H_2O bubbler[f]	50[g]
25	$^{40}Ca(^{16}O, 2np)^{53}Co^{m}$	(106) 79.2	7.6-μm Ni degrader foil	30

a) For heavy-ion beams, the initial beam energy is in ( ); the beam energy at the target surface is also given.

b) For those blank entries, no chemical additives were used.

c) With the exception of $^{53}Co^{m}$, these entries are for the total cross-section for production of the nuclide.

d) The helium was passed through a liquid-nitrogen trap.

e) This tube is twice as long as used for the other experiments.

f) The helium impurity-gas mixture was bubbled through the liquid at the entrance to the target box.

g) Beta-decay branching ratios estimated from Ve 68.

h) Beta-decay branching ratios from Ha 71.

i) Beta-decay branching ratios from To 73a.

j) Beta-decay branching ratio from Ce 70.

T_e is usually taken to be the recoil range in the target as computed from range-energy tables (No 70), while for those experiments where the recoils stop in the target, $T_e = \frac{t}{\cos \theta_t} - R$, where t is the target thickness, θ_t the target angle, and R the recoil range in the target.

The third factor is the inverse of the total number of beam particles, where Z_p is the projectile charge, e the electronic charge, and Q the total integrated charge collected. Finally, the last factor accounts for equilibrium of activity on the collector foils (or in the target), and T_c is the time for one complete revolution of the helium-jet collector wheel (= 6 × cycle time), or the cycle time for the pulsed-beam experiments; the remaining exponential terms account for decay during bombardment (t_b = bombardment time), and decay during the counting or delay times (t_c = counting time, t_d = delay time).

The product $\sigma \epsilon$ is in units of nanobarns for M in g/mole, T_e in mg/cm^2, and Q and e in μCoulomb. For those pulsed-beam experiments where the target was observed directly, $\epsilon \equiv 1$. The uncertainties associated with this product (and in deriving ϵ) are large, since many factors influence the results. One of the more significant, especially in the case of heavy ion beams, is the determination of the total beam current. There is multiple scattering in both the helium gas and in the exit foil which could affect the amount of beam refocused into the Faraday cup.

Relative cross-section information for various competing reactions is listed in Table A=1 also. As can be seen, both the (^{3}He, 2np) and (^{3}He, 2nα) reactions become more important at higher bombarding energies. Also shown are the $\sigma \epsilon$ products for (^{3}He, 2n) reactions on

several light-mass $T_z = 0$ targets; there appears to be considerable variation, influenced by both transport efficiencies and reaction cross-sections. The effects of various chemical additives are shown by comparing entries 1 and 9 (^{41}Ti), 11 and 12 (^{25}Si) and 13 and 14 (^{25}Si). In addition, studies done using the ^{24}Mg (p, αn) ^{20}Na reaction have shown effects due to beam intensity below 1 μA. The counts per unit of integrated charge drop linearly as the beam intensity is decreased down to ~100 μA. Above 1 μA, on the other hand, there appears to be no noticeable increase in this ratio. The effects of several chemical additives were also tested at these various beam intensities; no reproducible effects were observed.

In contrast to the ^{20}Na results, definite improvements in the transport efficiencies can be seen for ^{25}Si and ^{41}Ti; for the ^{20}Ne (^{12}C, 3n) reaction, the transport efficiency increased by a factor of 10 with the addition of air and an H_2O bubbler (see entry 24).

Table A-2 lists helium-jet efficiencies for some of the nuclides studied, based on measured cross-sections at similar beam energies. The pulsed-beam (wheel) data were obtained as part of this work. The ^{32}S(^{3}He, 2n) cross section has apparently not been measured. If it is similar to those for (^{3}He, 2n) reactions on other $T_z = 0$ targets, the ^{33}Ar transport efficiency can be estimated.

As noted above, due to uncertainties in the beam intensities, the efficiencies listed in Table A-2 are probably accurate within a factor of 3. It should also be noted that the efficiency includes 'sticking' probability as well as transport efficiency. The results described here apparently confirm the general view that chemical 'impurities' play a role

Table A-2. Cross-sections and Helium-jet Efficiencies.

Reaction	Beam Energy (MeV)	σ (nb)	Reference	ϵ (%)
$^{40}Ca(^{3}He, 2n)^{41}Ti$	40	50×10^{3}	wheel data	0.7
$^{24}Mg(p, 2n)^{23}Al$	40	220×10^{3}	wheel data	9.
$^{40}Ca(p, n)^{40}Sc$	20	3.8×10^{6}	wheel data	1.
$^{24}Mg(p, \alpha n)^{20}Na$	40	1.2×10^{6}	wheel data	8.
$^{40}Ca(^{12}C, 3n)^{49}Fe$	65	500	Ce 70	12.
$^{40}Ca(^{16}O, 2np)^{53}Co^{m}$	80	1.6×10^{3}	Ce 73	2.
$^{24}Mg(^{3}He, 2n)^{25}Si$	38	150×10^{3}	Es 71a	5.
$^{20}Ne(^{3}He, 2n)^{21}Mg$	31	230×10^{3}	Es 71a	0.5
$^{32}S(^{3}He, 2n)^{33}Ar$	30	$\sim50\times10^{3}$	estimate	<0.1

in this process (Ma 74) and that there appears to be some chemical specificity involved, either with regard to the type of 'impurity' used, or the chemical nature of the recoil product, or both (Ko 71, Ko 72). Clearly additional studies on increasing the transport efficiency, especially for low cross-section reactions, would be desirable.

FOOTNOTES

[1] Havar is an alloy consisting primarily of Co(42.5%), Ni(13.0%), Cr (20.0%), and Fe (17.9%), with a density of 8.3 gm/cm^3. Hamilton Watch Co., Metals Division, Lancaster, Penn.

[2] Chromium Corporation of America, 8701 Union Avenue, Cleveland, Ohio 44105

[3] Tube Sales, 1730 Geary Blvd., San Francisco, Ca 94115.

[4] Ledex, Inc., 123 Webster St., Dayton, Ohio 45401.

[5] Servometer Corporation, 82 Industrial East, Clifton, N. J. 07012.

[6] Transducer Technology, Inc., Route 83, Ellington, Conn. 06029.

[7] Ortec, Inc., 100 Midland Road, Oak Ridge, Tenn. 37830.

[8] Materials Electronics Products Corp., 990 Spruce St., Trenton, N. J. 08638.

REFERENCES

Ad 73 E. G. Adelberger, A. B. McDonald, C. L. Cocke, C. N. Davids, A. P. Shukla, H. B. Mak, and D. Ashery, Phys. Rev. C7, 889 (1973).

Aj 71 F. Ajzenberg-Selove, Nucl. Phys. A166, 1 (1971).

Aj 72 F. Ajzenberg-Selove, Nucl. Phys. A190, 1 (1972).

Al 72 D. E. Alburger and D. H. Wilkinson, Phys. Rev. C3, 1957 (1971).

Al 73 D. E. Alburger and D. H. Wilkinson, Phys. Rev. C8, 657 (1973).

Am 69 M. Amiel, M. Lambert, and H. Beaumevieille, Lettere Nuovo Cimento 1, 689 (1969).

Ar 67 A. Armigliato, L. M. El-Nadi, and F. Pellegrini, Nuovo Cimento 49B, 142 (1967).

Ar 71 A. Arima and S. Yoshida, Nucl. Phys. A161, 492 (1971).

Au 71 N. Auerbach and A. Lev, Phys. Lett. 34B, 13 (1971).

Ba 63 R. Barton, R. McPherson, R. E. Bell, W. R. Frisken, W. T. Link, and R. B. Moore, Can. J. Phys. 41, 2007 (1963).

Ba 64 J. N. Bahcall, Phys. Rev. 135, B137 (1964).

Ba 66 J. N. Bahcall, Phys. Rev. Lett. 17, 398 (1966).

Ba 66a J. N. Bahcall, Nucl. Phys. 75, 10 (1966).

Ba 72 T. T. Bardin, J. A. Becker, and T. R. Fisher, Phys. Rev. C5, 1351 (1972).

Be 65 T. A. Belote, A. Sperduto, and W. W. Buechner, Phys. Rev. 139, B80 (1965).

Be 67 T. A. Belote, F. T. Dao, W. E. Dorenbusch, J. Kuperus, J. Rapaport, and S. M. Smith, Nucl. Phys. A102, 462 (1967).

Be 67a P. Bém, J. Habanec, O. Karban, and J. Nemec, Nucl. Phys. A96, 529 (1967).

Be 69 J. A. Becker, R. E. McDonald, L. F. Chase, Jr., and D. Kohler, Phys. Rev. 188, 1783 (1969).

Be 70 R. C. Bearse, J. C. Legg, G. C. Morrison, and R. E. Segel, Phys. Rev. C1, 608 (1970).

Be 72 G. F. Bertsch and A. Mekjian, Ann. Rev. Nucl. Sci. 22, 25 (1972).

Be 72a W. Benenson, J. Driesbach, I. D. Proctor, G. F. Trentelman, and B. M. Preedom, Phys. Rev. C5, 1426 (1972).

Be 73 W. Benenson, E. Kashy, and I. D. Proctor, Phys. Rev. C8, 210 (1973).

Be 73a W. Benenson, E. Kashy, and I. D. Proctor, Phys. Rev. C 7, 1143 (1973).

Bl 66 S. D. Bloom, in Isobaric Spin in Nuclear Physics, ed. by J. D. Fox and D. Robson (Academic, New York, 1966) p. 123.

Bl 69 R. J. Blin-Stoyle, in Isospin in Nuclear Physics, ed. by D. H. Wilkinson (North Holland, Amsterdam, 1969) p. 115.

Bl 69a R. Bloch, T. Knellwolf, and R. E. Pixley, Nucl. Phys. A123, 129 (1969).

Bl 70 R. J. Blin-Stoyle and J. M. Freeman, Nucl. Phys. A150, 369 (1970).

Bo 65 R. Bock, H. H. Duhm, and R. Stock, Phys. Lett. 18, 61 (1965).

Br 68 H. Brunnader, J. C. Hardy, and J. Cerny, Phys. Rev. 174, 1247 (1968).

Br 73 C. P. Browne, J. D. Goss, and A. A. Rollefson, Phys. Rev C 8, 1805 (1973).

Bu 68 G. W. Butler, J. Cerny, S. W. Cosper, and R. L. McGrath, Phys. Rev. 166, 1096 (1968).

Ce 68 J. Cerny, Ann. Rev. Nucl. Sci. 18, 27 (1968).

Ce 69 J. Cerny, R. A. Mendelson, Jr., G. J. Wozniak, J. E. Esterl, and J. C. Hardy, Phys. Rev. Lett. 22, 612 (1969).

Ce 70 J. Cerny, C. U. Cardinal, H. C. Evans, K. P. Jackson, and N. A. Jelley, Phys. Rev. Lett. 24, 1128 (1970).

Ce 72 J. Cerny, R. A. Gough, R. G. Sextro, and J. E. Esterl, Nucl. Phys. A188, 666 (1972).

Ce 73 J. Cerny, unpublished results.

Ch 71 C. T. Chen-Tsai, S. T. Hsieh, and T. Y. Lee, Phys. Rev. C4, 2096 (1971).

Ch 72 J. E. Christiansson, J. Dubois, and L. Jarneborn, Physica Scripta 5, 159 (1972).

Cu 63 J. B. Cumming, in Applications of Computers to Nuclear and Radio-chemistry, ed. by G. D. O'Kelley, (Office of Technical Services, Washington, D.C., 1963) NAS-NS 3107, p. 25.

De 70 R. J. deMeijer, A. A. Sieders, H. A. A. Landman, and G. deRoos, Nucl. Phys. A155, 109 (1970).

Di 68 A. E. L. Dieperink and P. J. Brussaard, Nucl. Phys. A106, 177 (1968).

Du 72 J. R. Duray, H. J. Hausman, N. L. Gearhart, J. W. D. Sinclair, and W. S. Steiner, Phys. Rev. C6, 792 (1972).

En 66 G. A. P. Engelbertink and P. J. Brussaard, Nucl. Phys. 76, 442 (1966).

En 67 P. M. Endt and C. van der Leun, Nucl. Phys. A105, 1 (1967).

En 71 R. Engmann, R. Brandolini, and I. Mauritzson, Nucl. Phys. A171, 418 (1971).

Es 71 J. E. Esterl, R. G. Sextro, J. C. Hardy, G. J. Ehrhardt, and J. Cerny, Nucl. Instr. Methods 97, 229 (1971).

Es 71a J. E. Esterl, UCRL-20480, (Ph.D. Thesis) 1971, (unpublished).

Ev 71 F. Everling, G. L. Morgan, D. W. Miller, L. W. Seagondollar, and P. W. Tillman, Jr., Can. J. Phys. 49, 402 (1971).

Fo 65 J. L. C. Ford, Jr., J. K. Bair, C. M. Jones, and H. B. Willard, Nucl. Phys. 63, 588 (1965).

Ge 69 D. A. Gedcke, S. T. Lam, S. M. Tang, G. M. Stinson, J. T. Sample, T. B. Grandy, W. J. McDonald, W. K. Dawson, and G. C. Neilson, Nucl. Phys. A134, 141 (1969).

Go 64 F. S. Goulding, D. A. Landis, J. Cerny, and R. H. Pehl, Nucl. Instr. Methods 31, 1 (1964).

Go 65 F. S. Goulding, UCRL-16231, 1965 (unpublished).

Go 66 N. B. Gove, in Nuclear Spin-Parity Assignments, ed. by N. B. Gove and R. L. Robinson (Academic, New York, 1966) p. 83.

Go 67 D. R. Goosman and R. W. Kavanagh, Phys. Rev. 161, 1156 (1967).

Go 71 D. R. Goosman, K. W. Jones, E. K. Warburton, and D. E. Alburger, Phys. Rev. C4, 1800 (1971).

Go 71a N. B. Gove and M. J. Martin, Nucl. Data Tables 10, 205 (1971).

Go 72 R. A. Gough, R. G. Sextro, and J. Cerny, Phys. Rev. Lett. 28, 510 (1972).

Go 73 R. A. Gough, R. G. Sextro, J. Cerny, Phys. Lett. 43B, 33 (1973).

Gr 68 L. R. Greenwood, T. R. Canada, and C. M. Class, Bull. Am. Phys. Soc. 13, 1382 (1968).

Ha 64 J. C. Hardy and R. I. Verrall, Phys. Rev. Lett., 13, 764 (1964).

Ha 65 J. C. Hardy and B. Margolis, Phys. Lett. 15, 276 (1965).

Ha 65a J. C. Hardy and R. E. Bell, Can. J. Phys. 43, 1671 (1965).

Ha 66 J. C. Hardy and D. J. Skyrme, in Isobaric Spin in Nuclear Physics, ed. by J. D. Fox and D. Robson (Academic, New York, 1966) p. 701.

Ha 69 J. C. Hardy, H. Brunnader, J. Cerny, and J. Jänecke, Phys. Rev. 183, 854 (1969).

Ha 70 L. C. Haun, N. R. Roberson, and D. R. Tilley, Nucl. Phys. A140, 333 (1970).

Ha 70a W. R. Harris and D. E. Alburger, Phys. Rev. C1, 180 (1970).

Ha 71 J. C. Hardy, J. E. Esterl, R. G. Sextro, and J. Cerny, Phys. Rev. C3, 700 (1971).

Ha 72 J. C. Hardy, Nucl. Data Tables 11, 327 (1972).

Ha 72a F. X. Haas, C. H. Johnson, and J. K. Bair, Nucl. Phys. A193, 65 (1972).

Ha 73 J. C. Hardy, private communication.

Ha 74 J. C. Hardy, in Nuclear Spectroscopy and Reactions, ed. by J. Cerny (Academic, New York, to be published).

Hi 69 R. E. Hintz, F. B. Selph, W. S. Flood, B. G. Harvey, F. G. Resmini, and E. A. McClatchie, Nucl. Instr. Methods 72, 61 (1969).

Ja 70 W. Jaus and G. Rasche, Nucl. Phys. A143, 202 (1970).

Ja 72 W. Jaus, Phys. Lett. 40B, 616 (1972).

Ke 66 I. Kelson and G. T. Garvey, Phys. Lett. 23, 689 (1966).

Ko 65 E. J. Konopinski and M. E. Rose, in Alpha-, Beta-, and Gamma-Ray Spectroscopy, ed. by K. Siegbahn (North Holland, Amsterdam, 1965) p. 1327.

Ko 71 K. L. Kosanke, H. P. Hilbert, and W. C. McHarris, Michigan State University Annual Report 1971-1972 (unpublished), p. 97.

Ko 72 K. L. Kosanke, M. Slaughter, and W. C. McHarris, Michigan State University Annual Report 1972-1973 (unpublished), p. 90.

La 72 W. A. Lanford and B. H. Wildenthal, Phys. Rev. Lett. 29, 606 (1972).

La 73 W. A. Lanford and B. H. Wildenthal, Phys. Rev. C 7, 668 (1973); additional ^{21}Mg log ft values privately communicated.

Li 68 A. E. Litherland, in Third Symposium on the Structure of Low-Medium Mass Nuclei, ed. by J. P. Davidson (Univ. of Kansas Press, Lawrence, 1968) p. 92.

Ly 67 U. Lynen, R. Bock, R. Santo, and R. Stock, Phys. Lett. 25B, 9 (1967).

Ma 68 J. B. Marion and F. C. Young, Nuclear Reaction Analysis: Graphs and Tables (North Holland, Amsterdam, 1968) pp. 84-86.

Ma 69 R. D. Macfarlane, R. A. Gough, N. S. Oakey, and D. F. Torgerson, Nucl. Instr. Methods 73, 285 (1969).

Ma 70 A. Marinov, Ch. Drory, E. Navon, J. Burde, and G. Engler, Nucl. Phys. A145, 534 (1970).

Ma 70a R. D. Macfarlane, N. S. Oakey, and R. A. Gough, in The Uses of Cyclotrons in Chemistry, Metallurgy and Biology, ed. by C. B. Amphlett (Butterworths, London, 1970) p. 232; and private communication.

Ma 71 J. R. MacDonald, D. H. Wilkinson, and D. E. Alburger, Phys. Rev. C 3, 219 (1971).

Ma 71a C. C. Maples, LBL-253 (Ph.D. Thesis), 1971 (unpublished).

Ma 72 P. Martin, M. Buenerd, Y. Dupont, and M. Chabre, Nucl. Phys. A185, 465 (1972).

Ma 74 R. D. Macfarlane and W. C. McHarris, in Nuclear Spectroscopy and Reactions, ed. by J. Cerny (Academic, New York, to be published).

Mc 65 R. McPherson and J. C. Hardy, Can. J. Phys. 43, 1 (1965).

Mc 68 I. E. McCarthy, Introduction to Nuclear Theory (Wiley, New York, 1968).

Mc 69 A. B. McDonald, J. R. Patterson, and H. Winkler, Nucl. Phys. A137, 545 (1969).

Mc 70 R. L. McGrath, J. Cerny, J. C. Hardy, G. Goth, and A. Arima, Phys. Rev. C 1, 184 (1970).

Mo 68 G. C. Morrison, D. H. Youngblood, R. C. Bearse, and R. E. Segel, Phys. Rev. 174, 1366 (1968).

Ne 72 R. O. Nelson and N. R. Roberson, Phys. Rev. C 6, 2153 (1972).

No 70 L. C. Northcliffe and R. F. Schilling, Nucl. Data Tables A7, 233 (1970).

Pi 72 M. Piiparinen, Z. Physik 252, 206 (1972).

Po 66 A. M. Poskanzer, R. McPherson, R. A. Esterlund, and P. L. Reeder, Phys. Rev. 152, 995 (1966).

Re 64 P. L. Reeder, A. M. Poskanzer, and R. A. Esterlund, Phys. Rev. Lett. 13, 767 (1964).

Re 66 P. L. Reeder, A. M. Poskanzer, R. A. Esterlund, and R. McPherson, Phys. Rev. 147, 781 (1966).

Ro 70 H. Röpke, H. J. Brundiers, and G. Hammel, Nucl. Phys. A153, 211 (1970).

Ro 72 C. Rolfs, H. P. Trautvetter, E. Kuhlmann, and R. Riess, Nucl. Phys. A189, 641 (1972).

Sa 67 G. Sartoris and L. Zamick, Phys. Rev. Lett. 18, 292 (1967).

Sc 70 J. J. Schwartz and B. A. Watson, Phys. Lett. 31B, 198 (1970).

Se 73 R. G. Sextro, R. A. Gough, and J. Cerny, Phys. Rev. C 8, 258 (1973).

Se 73a K. K. Seth, A. Saha, and L. Greenwood, Phys. Rev. Lett. 31, 552 (1973).

Sk 66 S. J. Skorka, J. Hertel, and T. W. Retz-Schmidt, Nucl. Data Tables A2, 347 (1966).

Sm 68 S. M. Smith, A. M. Bernstein, and M. E. Rickey, Nucl. Phys. A113, 303 (1968).

St 69 J. E. Steigerwalt, J. W. Sunier, and J. R. Richardson, Nucl. Phys. A137, 585 (1969).

Te 69 G. M. Temmer, in Isospin in Nuclear Physics, ed. by D. H. Wilkinson (North Holland, Amsterdam, 1969), p. 693.

Te 69a B. Teitelman and G. M. Temmer, Phys. Rev. 177, 1656 (1969).

Th 70 T. T. Thwaites, Nucl. Phys. A150, 531 (1970).

To 71 D. F. Torgerson, N. S. Oakey, and R. D. Macfarlane, Nucl. Phys. A178, 69 (1971).

To 73 I. S. Towner and J. C. Hardy, Nucl. Phys. A205, 33 (1973).

To 73a D. F. Torgerson, K. Wien, Y. Fares, N. S. Oakey, R. D. Macfarlane, and W. A. Lanford, Phys. Rev. C8, 161 (1973).

Tr 73 T. A. Trainor, T. B. Clegg, and W. J. Thompson, Bull. Am. Phys. Soc. 18, 602 (1973).

Tr 73a T. A. Trainor, University of North Carolina, (Ph.D. Thesis) 1973 (unpublished).

Ty 54 H. Tyrén and P. A. Tove, Phys. Rev. 96, 773 (1954).

Va 64 C. van der Leun and W. L. Mouton, Physica 30, 333 (1964).

Va 69 R. J. van Reenen, Z. B. DuToit, and W. L. Mouton, Z. Physik 227, 326 (1969).

Ve 68 R. I. Verrall, McGill University, (Ph.D. Thesis) 1968 (unpublished).

Ve 69 R. I. Verrall and R. E. Bell, Nucl. Phys. A127, 635 (1969).

Wa 71 A. H. Wapstra and N. B. Gove, Nucl. Data Tables 9, 265 (1971).

Wi 70 D. H. Wilkinson and B. E. F. Macefield, Nucl. Phys. A158, 110 (1970).

Wi 70a D. H. Wilkinson, Phys. Lett. 31B, 447 (1970).

Wi 70b D. H. Wilkinson, Nucl. Phys. A158, 476 (1970).

Wi 71 D. H. Wilkinson, Phys. Rev. Lett. 27, 1018 (1971).

Wi 71a D. H. Wilkinson, D. E. Alburger, D. R. Goosman, K. W. Jones, E. K. Warburton, G. T. Garvey, and R. L. Williams, Nucl. Phys. A166, 661 (1971).

Wi 72 D. H. Wilkinson, D. R. Goosman, D. E. Alburger, and R. E. Marrs, Phys. Rev. C 6, 1664 (1972).

Wi 73 D. H. Wilkinson, Nucl. Phys. A209, 470 (1973).

Yo 66 D. H. Youngblood, G. C. Morrison, and R. E. Segel, Phys. Lett. 22, 625 (1966).

Yo 68 D. H. Youngblood, B. H. Wildenthal, and C. M. Class, Phys. Rev. 169, 859 (1968).

Yo 70 D. H. Youngblood, R. L. Kozub, R. A. Kenefick, and J. C. Hiebert, Phys. Rev. C 2, 477(1970).

Yo 70a D. H. Youngblood, R. L. Kozub, J. C. Hiebert, and R. A. Kenefick, Nucl. Phys. A143, 512 (1970).